



**University of  
Zurich<sup>UZH</sup>**

# Building a Setup for Electroluminescence with the Scanning Tunneling Microscope and Tip Functionalization with Plasmonic Gold Nanoparticles

Master Thesis in Physics

**Cinja Müller - [cinjacherylynn.mueller@uzh.ch](mailto:cinjacherylynn.mueller@uzh.ch)**

Supervised by

Prof. Dr. F. D. Natterer and his group  
including Dr. Aleš Čahlík, Dr. Carolina Marques, Berk Zengin, Danyang  
Liu, and Dr. Johannes Schwenk

May 22, 2023

## Abstract

---

Scanning tunneling microscopy induced luminescence (STML) is a technique that combines the high-resolution imaging capabilities of STM with the ability to detect and map the optical emission of a sample at the nanoscale. In this master thesis, we present the development of a setup for STML, where we attached gold nanoparticles (AuNPs) onto the apex or Pt/Ir tips. We dropcast commercially available colloidal AuNPs onto Highly Oriented Pyrolytic Graphite (HOPG) from which the AuNPs may be transferred to the STM tip. We describe our setup and characterize the electroluminescence using a fiber-coupled single photon detector. We also discuss the theoretical background of STML. Through our experimental work, we successfully picked up AuNPs from HOPG and measured luminescence coming from the STM junction. This work demonstrates the potential of using AuNPs on STM tips for STML.

## Zusammenfassung

---

Mit der Technik der lumineszenten Rastertunnelmikroskopie (STML) werden die hochauflösenden Abbildungsmöglichkeiten des Rastertunnelmikroskops (STM) mit der Fähigkeit kombiniert, die optische Emission einer Probe im Nanobereich zu detektieren und als Photon map darzustellen, kombiniert. In dieser Masterarbeit präsentieren wir die Entwicklung eines Setups für STML, bei dem Goldnanopartikel (AuNPs) an der Spitze von Pt/Ir-Spitzen angebracht wurden. Wir haben kommerziell erhältliche kolloidale AuNPs auf hoch orientiertes pyrolytisches Graphit (HOPG) mit der Drop-Cast-Methode appliziert. Danach haben wir die AuNPs vom HOPG mit der STM-Spitze aufgehoben. Wir beschreiben unser Setup und charakterisieren die Elektrolumineszenz mit einem fasergekoppelten Einzelphotonenzähler. Zusätzlich erörtern wir den theoretischen Hintergrund von STML. Schlussendlich konnten wir mit unserem experimentellen Aufbau erfolgreich AuNPs von HOPG aufheben und die Lumineszenz der STM-Verbindung nachweisen. Diese Arbeit zeigt das Potenzial der Verwendung von AuNPs auf STM-Spitzen für STML.

## Acknowledgements

---

I would like to express my sincere gratitude to everyone who supported me throughout the journey of writing this thesis. Thanks to all the good people I met and who believed in me #love.

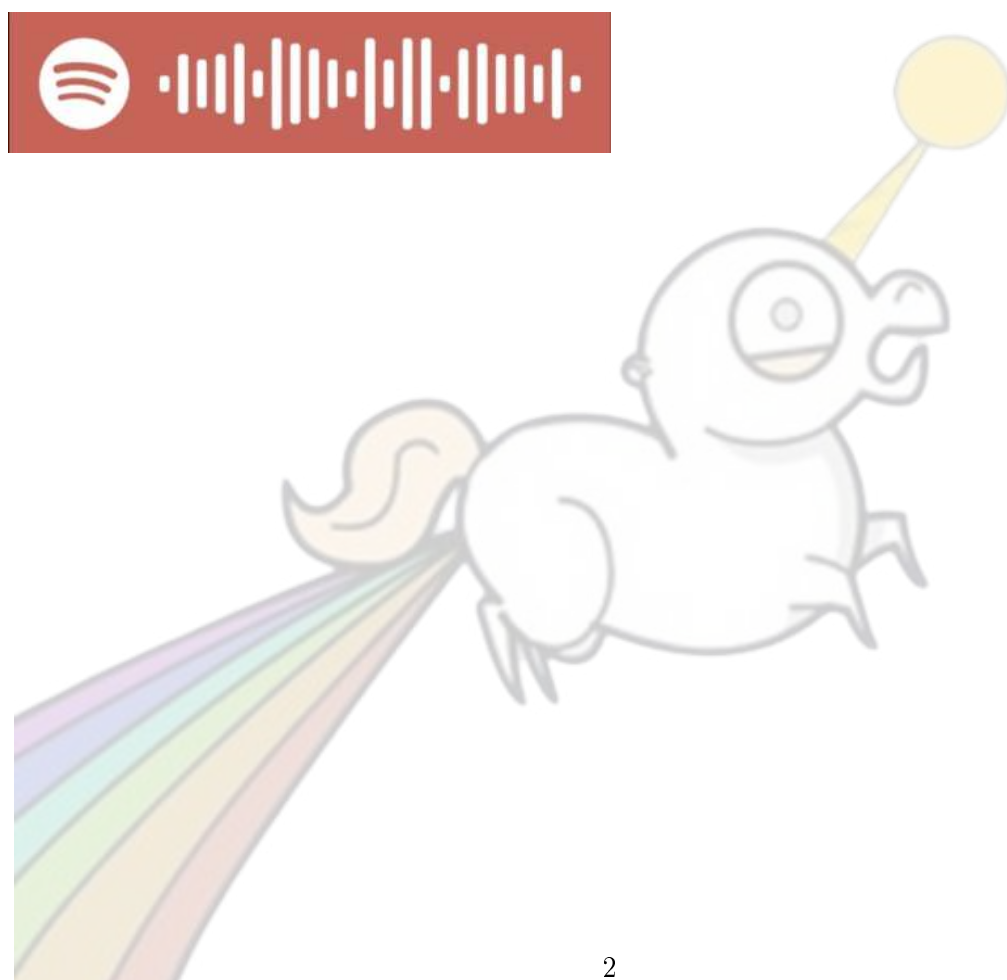
First and foremost, I want to thank my boyfriend for his unwavering love, encouragement, and support. And also for lending me the pipette for the dropcast method.

I am also grateful to my professor, Prof. Dr. Fabian Natterer, and his research group, including Dr. Aleš Cahlík, Dr. Carolina Marques, Berk Zengin, Danyang Liu, and Dr. Johannes Schwenk. Their guidance and expertise were invaluable in helping me understand the intricacies of my research topic. I am especially thankful for the countless discussions, support, and sessions we had, which helped me finally master the technique of picking up and understanding those gold particles.

I would like to thank Simon Jöhr for offering his support, patience and expertise of the AFM.

I would like to thank Dr. Matthias Hengsberger for the lent USB2000+ Fiber Optic Spectrometer. I would like to thank Dr. Andres Käch for the gifted TEM grids.

I would also like to extend my appreciation to technician Damian Bucher for his invaluable assistance and to Dr. Mirco Ackermann for his support, shared expertise with optical setups, the lent bandpass filters and the lent stingray F-145 camera. Also his offer to use his computer skills to export the data from Windows NT saved me hours of transferring data via floppy disks. Finally, I would like to thank again the whole group, my friends and my family who supported me during this time. Their love and encouragement were crucial in keeping me motivated.



# Contents

<b>I</b>	<b>Introduction and motivation</b>	<b>8</b>
<b>II</b>	<b>Theory</b>	<b>12</b>
<b>1</b>	<b>Scanning Tunneling Microscopy (STM)</b>	<b>12</b>
1.1	Bardeen Model . . . . .	12
<b>2</b>	<b>Luminescence</b>	<b>13</b>
2.1	Planck relation . . . . .	15
2.1.1	Conventional inversed photon emission . . . . .	15
<b>3</b>	<b>Historical Background of STML</b>	<b>16</b>
<b>4</b>	<b>Collective Excitations and Plasma resonance</b>	<b>16</b>
<b>5</b>	<b>Plasmons and Models</b>	<b>17</b>
5.1	Surface Plasmon Polariton (SPP) . . . . .	18
5.1.1	Theoretical Description of SPP . . . . .	19
5.2	Surface Plasmon (SP) . . . . .	20
5.3	Localized Surface Polariton (LSP) . . . . .	20
5.4	Models describing LSP in STM . . . . .	21
5.4.1	Inelastic tunneling (IET) and hot electron thermalization (HET) . . . . .	21
5.4.2	Model of Persson and Baratoff . . . . .	22
5.4.3	Model of Rendell . . . . .	23
5.4.4	Model of Johansson . . . . .	24
5.4.5	Conclusion from the models . . . . .	24
<b>6</b>	<b>Experimental manifestations of localized surface plasmons (LSP)</b>	<b>24</b>
6.1	Influence of LSPs on the tunneling current of STM . . . . .	24
6.2	Light emission . . . . .	25
6.2.1	Historical plot and explanations . . . . .	26
6.2.1.1	Explanations of observation 1 . . . . .	26
6.2.1.2	Explanations of observation 2 . . . . .	27
6.2.1.3	Explanations of observation 3 . . . . .	28
6.2.1.4	High-bias intensity suppression . . . . .	28
6.2.1.5	Change in peak positions . . . . .	28
<b>7</b>	<b>Experimental considerations</b>	<b>29</b>
7.1	Dielectric constant or permittivity . . . . .	29
7.2	Tip size . . . . .	31
7.2.1	Adding plasmonic particles on a STM tip . . . . .	34
7.3	Quantum efficiency . . . . .	35
7.3.1	Angle of Light emission . . . . .	35
<b>III</b>	<b>Experimental Section</b>	<b>37</b>

<b>1</b>	<b>Introduction</b>	<b>37</b>
1.1	Application of AuNP on HOPG . . . . .	38
1.2	Optical Setup . . . . .	39
1.3	VTSTM . . . . .	40
<b>2</b>	<b>Samples</b>	<b>41</b>
2.1	Gold Nanoparticles (AuNP) . . . . .	41
2.2	Highly Oriented Pyrolytic Graphite (HOPG) . . . . .	41
2.3	Gold crystal . . . . .	42
<b>3</b>	<b>Application of AuNP on HOPG</b>	<b>43</b>
3.1	Dropcasting Method . . . . .	43
3.1.1	Setup . . . . .	43
3.1.2	Methods and Results . . . . .	43
3.1.2.1	Increase concentration . . . . .	43
3.2	Electrospray . . . . .	45
3.2.1	Setup . . . . .	45
<b>4</b>	<b>Optical setup to detect light</b>	<b>50</b>
4.1	Setup . . . . .	50
4.1.1	Sample holder . . . . .	50
4.1.2	Light sensitive camera stingray F-145 . . . . .	50
4.1.3	Fibres . . . . .	51
4.1.4	USB2000+UV-VIS-ES Fiber Optic Spectrometer . . . . .	51
4.1.5	Single Photon detector (SPD) . . . . .	51
4.1.6	Optical Setup . . . . .	52
4.1.6.1	Lens holder . . . . .	54
4.1.6.2	Thorlabs camera . . . . .	55
4.1.6.3	Bandpass filters . . . . .	56
4.2	Experiments and methods . . . . .	56
4.2.1	Light sensitive Stingray F-145 camera . . . . .	56
4.2.2	Filters . . . . .	57
4.2.3	USB2000+ Spectrometer . . . . .	57
4.3	Results . . . . .	57
4.3.1	Light sensitive Stingray F-145 camera . . . . .	57
4.3.1.1	Measurements on a gold crystal . . . . .	57
4.3.1.1.1	Light we see above 5 eV . . . . .	57
4.3.1.2	Measurements on gold nanoparticles (AuNPs) dropcasted on HOPG . . . . .	59
4.3.2	USB2000+ Spectrometer . . . . .	60
<b>5</b>	<b>VTSTM</b>	<b>64</b>
5.1	Setup . . . . .	64
5.1.1	Calibration with HOPG . . . . .	65
5.2	Goldcrystal . . . . .	66
5.2.1	Experiments and methods . . . . .	66
5.2.1.1	Poking crystal . . . . .	66
5.2.1.2	Fibre M133L02 pointing directly in the junction . . . . .	66
5.2.1.2.1	Heatmap . . . . .	66
5.2.1.2.2	Spectroscopy . . . . .	67
5.2.1.2.3	Optical setup . . . . .	67

5.2.2	Results	67
5.2.2.1	Poking crystal	67
5.2.2.2	Fibre M133L02 pointing directly in the junction	68
5.2.2.2.1	Heatmap	68
5.2.2.2.2	Spectroscopy	69
5.2.2.3	LFM1F-1 fibre pointing directly at the junction	71
5.2.2.4	Optical setup	71
5.3	AuNP on HOPG ZYA	72
5.3.1	Experiments and methods	72
5.3.1.1	Dropcast	72
5.3.1.2	Scanning particles	72
5.3.1.3	Picking up AuNPs	73
5.3.2	Results	74
5.3.2.1	Picking up AuNPs	74

## IV Conclusion and outlook 76

### A Question and Answers A1

A.1	Why does the solution need cooling?	A1
A.2	Why shouldn't we freeze the solution?	A1
A.3	What does the component citric acid do?	A1
A.4	What does the component ether do?	A1
A.5	What is the particle density?	A2
A.6	How do the nanoparticles sediment if they do?	A2
A.7	Why is the solution pink?	A3

### B Setup A5

B.1	Nanostructuring	A5
B.2	Particles	A7
B.3	Electro spray	A10
B.4	Tip preparation	A12
B.5	Optical setup	A13
B.6	Lensholder design	A16
B.7	Calibration of the VTSPM	A18
B.7.1	xy direction	A18
B.7.2	z direction	A19
B.8	Scaling of the BX41M light microscope	A20

### C Results A21

C.1	Dropcast method	A21
C.1.1	Drying drops	A22
C.1.2	Increase AuNP density	A29
C.1.2.1	Heating	A29
C.1.2.1.1	Increase optical density of the AuNP solution.	A29
C.1.2.1.2	Make smaller drops	A30
C.1.2.2	Dropcast several drops in a area limited by silver glue	A37
C.2	AFM measurements	A37
C.2.1	Gwyddion 2.6	A37
C.2.2	ZYA	A39

C.2.3	ZYH . . . . .	A43
C.3	Light sensitive camera stingray F-145 . . . . .	A45
C.3.1	ImageJ analysis . . . . .	A45
C.3.2	Collecting the light coming from the STM junction with the Stingray camera.	A48
C.4	Single Photon detector . . . . .	54
C.4.1	Measurements with LFM1F-1 fibre pointing directly in the junction . . . . .	54

**Table 1:** Abbreviations used in the thesis.

Abb.	Meaning
SEM	Scanning electron microscopy
SPM	Scanning probe microscopy
AFM	Atomic force microscopy
STM	Scanning tunneling microscope
DOS	Density of states
UHV	Ultra High Vacuum
TTL	Transistor-transistor logic
HOPG	Highly oriented pyrolytic graphite
AuNP	Gold Nanoparticles
OD	Optical density
SPD	Single photon detector
IPES	Inverse photoemission spectroscopy
SPP	Surface plasmon polariton
SP	Surface plasmon
LSP	Localized surface plasmons
TIP	Tip induced plasmon
IET	Inelastic electron tunneling
ITS	Inelastic tunneling spectroscopy
HET	Hot electron thermalization
SNOM or NSOM	Scanning near-field optical microscope
a-SNOM	Apertureless SNOM
TERS	Tip-enhanced Raman scattering
THz-STM	Terahertz scanning tunneling microscopy
SPPX-STM	Shaken pulse pair excited STM
SERS	Surface enhanced raman
STML	Scanning tunneling microscopy-induced luminescence



# Part I

## Introduction and motivation

Luminescent STM is a powerful technique that combines the high-resolution imaging capabilities of STM with the ability to detect and map the optical emission of a sample at the nanoscale. The main theoretical concepts for luminescence in tunneling junctions and first experiments are from the 1980s performed by researchers including Berndt *et al.*, Gimzewski and Möller. In his review paper Berndt said, that luminescence adds "true colour" to STM (intensity, spectral distribution, angular emission, polarization and time correlation) [1]. A more recent paper from 2017 summarized STML measurement modalities, as seen in Figure 1 [2].

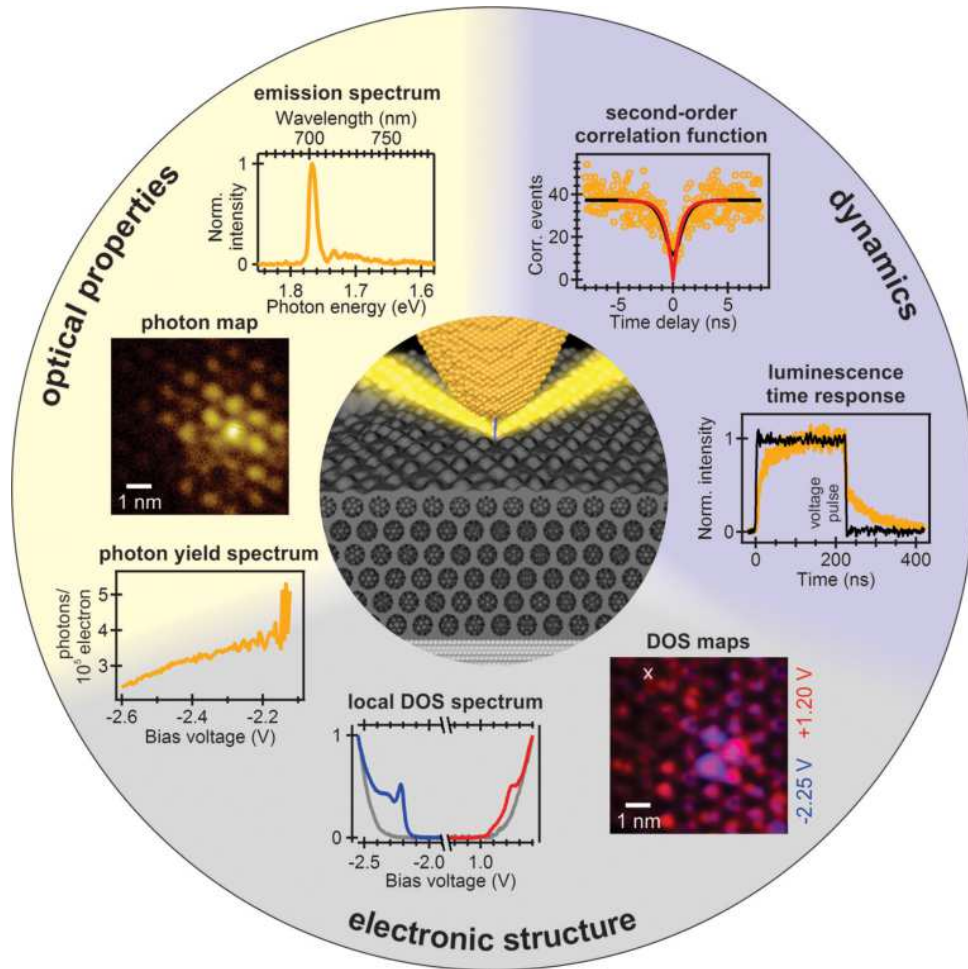


**Figure 1:** Selection of measurement modalities available in STML, illustrated by using the example of thin semiconducting  $C_{60}$  films on a crystalline metal substrate. Bottom: Electronic spectroscopy and spectrally resolved surface mapping belong to measurement modes of STM. Upper left: STML adds the capability of optical analysis, like electroluminescence-yield spectroscopy, the highly resolved mapping of electroluminescence by photon maps, and optical-emission spectroscopy from a selected position on the surface. Upper right: Both photon-photon correlation and the transient electroluminescence response to short voltage pulses exploit the time resolution of optical detectors to study dynamics in the nanosecond and picosecond ranges [2].

In my master thesis I built and tested a setup for STML from scratch. It is intended to be used as an addition of the measurement modalities the group of Prof. Natterer is already using.

One important step of the STML technique is the tip preparation using plasmonic metals. A plasmonic metal supports surface plasmons, which are collective oscillations of electrons at the interface between the metal and a dielectric material. Some common examples of plasmonic metals are gold, silver, and copper, as they have the properties to support surface plasmons in the visible and near-infrared regions of the spectrum [3]. However, other metals and alloys can also exhibit plasmonic behavior, depending on their composition and geometry.

To prepare tips for STML measurement, they either make tips from wires of plasmonic metals or coat tungsten (or Pt/Ir) tips by violent indentation into Au or Ag crystals.

Tips made from Ag, Co or Au wires are reported to be mechanically unstable.

### Tip functionalization by indentation in crystals

#### Excerpts found in papers

- "To optimise their plasmonic response, the tips are eventually indented in clean Ag(111) to cover them with silver [4]."
- "Tungsten STM tips were introduced into the sample to cover them with silver so as to tune their plasmonic response [5]."
- "The PtIr tip was sharpened by a focused ion beam before inserting into the scanner. Tips were cleaned and coated by Ag or Au material by applying voltage pulses and controlled nanoscopic indentations into the clean substrate [6]."
- "As a final step of the preparation, tips were slightly indented in the sample and, therefore, are most likely Au-coated [7]."

In the last excerpt from the gray box above, Schull *et al.* used optical spectroscopy and described the light coming from the junction. Also Benjamin Doppagne pointed out the influence of the tip shape on the spectra (see Figure 2) and how a tip shaped by indentation looks like in the SEM (see Figure 3) [8] in his PhD thesis.

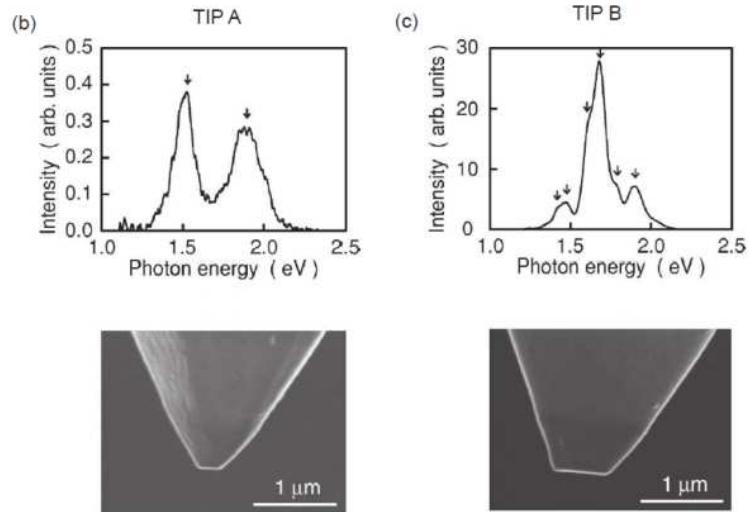


**Figure 2:** Influence of the tip shape on the STML spectrum. Top: STML spectra obtained with the corresponding tips below. Bottom: SEM image of the tips [8].

We conclude that the plunging of tungsten tips into metal substrates is rather crude and irreproducible. Therefore, as an additional goal of my thesis was to find a way to functionalize the tips in a more controlled fashion. We attempt to use concepts from both extremes by attaching gold nanoparticles (AuNPs) onto the apex of Pt/Ir tips. We dropcast commercially available colloidal AuNPs onto HOPG from which the AuNP may be transferred to the STM tip by gentle contact. We describe our setup and characterize the electroluminescence using a fiber-coupled single photon detector.

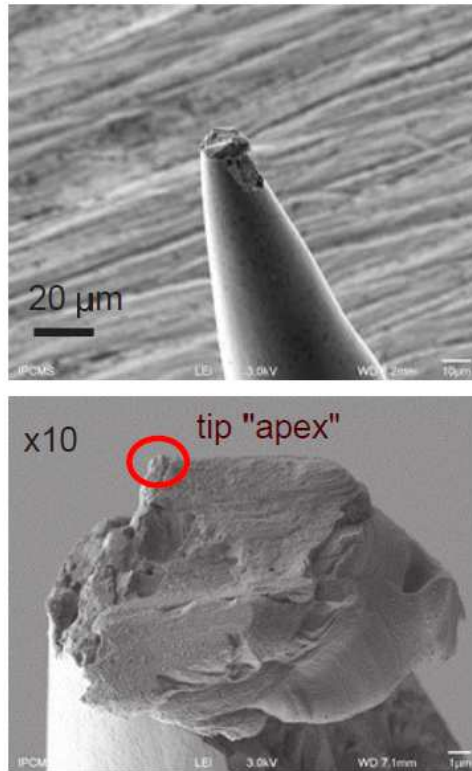


**Figure 3:** SEM image of a tungsten tip covered with silver after indentation in an Ag crystal. The tip apex area is circled in red [8].

# Part II

## Theory

---

### 1 Scanning Tunneling Microscopy (STM)

STM is used to observe the topography of a sample on the atomic scale. It works by scanning a sharp tip over a sample surface while applying a bias voltage  $V_B$  between them, which results in a tunneling current  $I$  that depends among other things on the distance  $d$  between the tip and the sample. The STM can not only provide atomic-resolution imaging of surfaces but also spectroscopic information about the electronic properties of materials. Note however, that the STM topography does not represent an image of constant surface charge density but the STM tip follows the local density of states at the Fermi level, whereas all electrons from the Fermi energy to the bias voltage contribute to the charge density.

In my thesis, I will present the theoretical working principle of STM since it will be useful to understand the concept of luminescent STM (STML). For further information, I recommend the book "Scanning Probe Microscopy" by Bert Voigtländer [9].

#### 1.1 Bardeen Model

Tersoff and Hamann developed the STM theory, using Bardeen's theoretical model for tunnelling current flowing between two metals separated by a thin oxide layer, applied to STM [10][11]. It explains the working principle of STM using the concept of density of states (DOS), which is a probability density function describing the distribution of energy states available to electrons in a material.

We consider the tip (blue in Figure 4) and the sample (red in Figure 4) as two separate systems. We use the zero-temperature limit in which all levels are filled up to the Fermi level  $E_F$  and are empty above. A bias voltage  $V_B$  (light blue) is applied between the tip and the sample. When a positive bias voltage is applied to an electrode, the energy of the states in this electrode is decreased. This causes electrons to flow from the tip to the sample if the sample is at a lower potential than the tip.

An electron initially in a tip state can scatter into a sample state. This transition is called tunneling. Tunneling can only occur in the bias window (orange arrows of Figure 4) between  $E_{F,\text{sample}}$  and  $E_{F,\text{tip}}$ . With this model, the transition rate (number of electrons per time) from a particular (initial) tip state  $i$  at  $E_{\text{tip},i}$  to a particular (final) sample state  $f$  at  $E_{\text{sample},f}$  results in equation 1.1 by using time-dependent perturbation theory.

$$\omega_{i \rightarrow f} = \frac{2\pi}{\hbar} |M_{fi}|^2 \delta(E_{\text{sample},f} - E_{\text{tip},i}) \quad (1.1)$$

Here,  $M_{fi}$  is the tunneling matrix element. The Dirac delta function in equation 1.1 shows that the energy of the final state must be the same as the energy of the initial state (solid orange lines in Figure 4), as expected from **energy conservation**. This means for STM we **only consider elastic tunneling**. The tunneling current  $I$  is proportional to the product of the DOS at the Fermi level of the sample  $D_{\text{sample}}(E_F)$  and the DOS at the corresponding energy level (shifted by the bias voltage  $V_B$ ) of the tip  $D_{\text{tip}}(E_F - V_B)$  and can be described with equation 1.2.

$$I = C(V) \int \int D_{\text{sample}}(E_F) D_{\text{tip}}(E_F - V_B) e^{-2\kappa d} dE dV \quad (1.2)$$

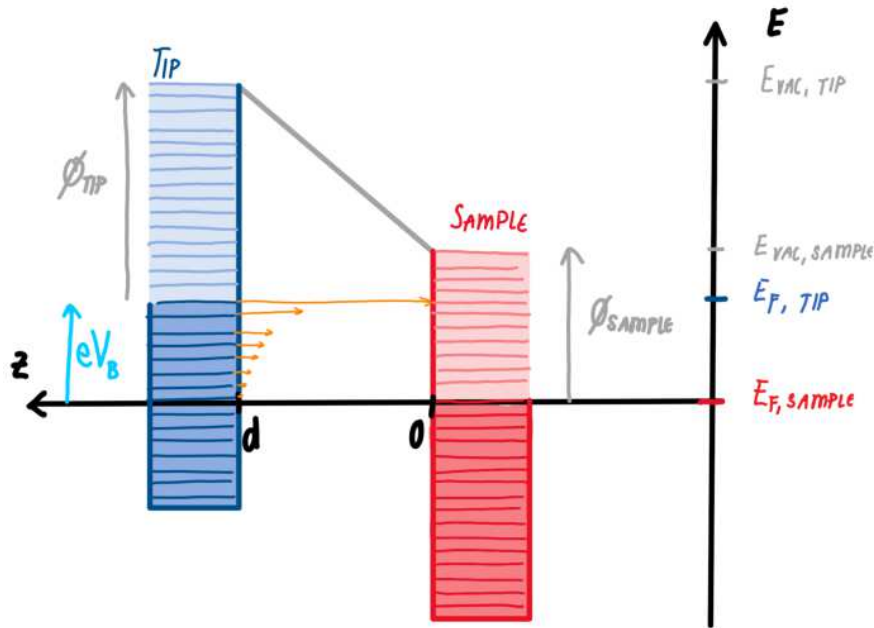


**Figure 4:** The tunnel barrier. Energy level diagram of a one-dimensional tunneling junction between tip (blue) and sample (red) states for the case of positive sample bias voltage  $V_B$ . Tunneling with energy conservation can only occur within the bias window (orange arrows), whereby the exponentially decaying probability of the tunneling is marked with increasing length of the arrows.  $\Phi$  are the workfunctions of the tip and the sample. Above the bias window, the initial states are empty, and below the final states are occupied. All energies are referred relative to the sample Fermi level.

Here,  $C(V)$  is a voltage-dependent constant,  $\kappa$  is a decay factor, and  $d$  is the distance between the tip and the sample surface. This relationship can be used to extract information about the electronic structure of materials and to identify specific electronic states [9].

## 2 Luminescence

According to the IUPAC definition [12], luminescence is the spontaneous emission of radiation from an electronically or vibrationally excited species that is not in thermal equilibrium with its environment. Light emission occurs as a result of the relaxation of electrons between different energy levels after being excited by external factors ( $E_{\text{ext.}}$ ). Luminescent processes are named after their external excitation. Examples include photoluminescence (light), which includes fluorescence and phosphorescence, chemiluminescence (chemical reactions), bioluminescence (reactions in living organisms), electroluminescence (electrical energy), sonoluminescence (ultrasound vibrations) and radioluminescence (ionizing radiation).

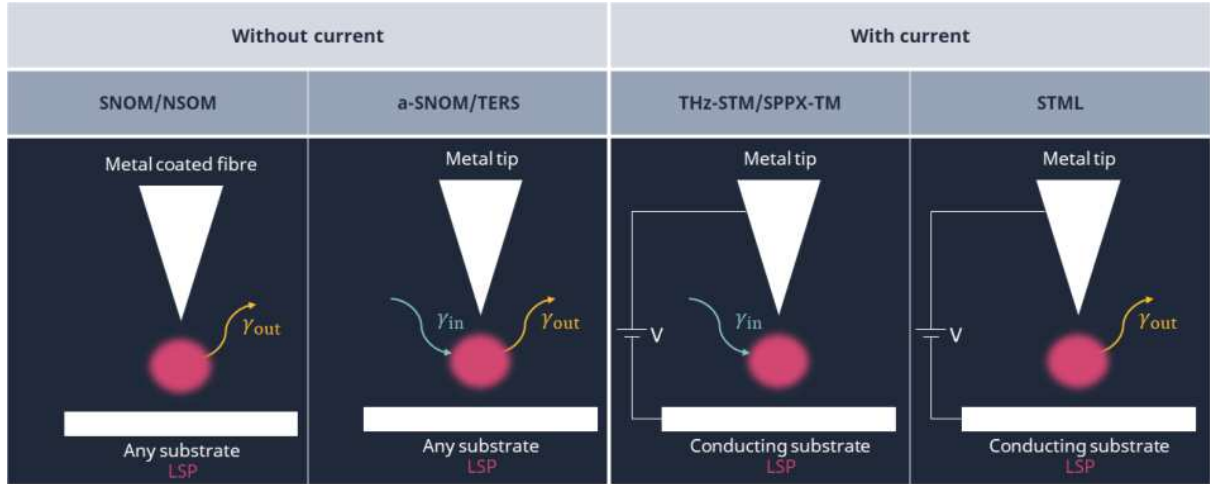


**Figure 5:** Experimental schemes probing optical near-fields by a scanning probe. Both methods on the left show scattering of the locally enhanced optical field from the object. Both methods on the right combine this principle with a measurement of the current through a tunnel barrier. This thesis focuses on electroluminescence induced by local charge injection in a scanning tunnel microscope (on the right). The acronyms are summarized in the Table 1 [2].

This thesis focuses on **electroluminescence** induced by local charge injection using a scanning tunnel microscope (see STML in Figure 5). The acronyms in Figure 5 are summarized in Table 1. We want to apply the concept of electrons relaxing from different energy levels and radiating to STML to Figure 6. Therefore, we introduce the concept of plasmons, explain TIP plasmons and their excitation.

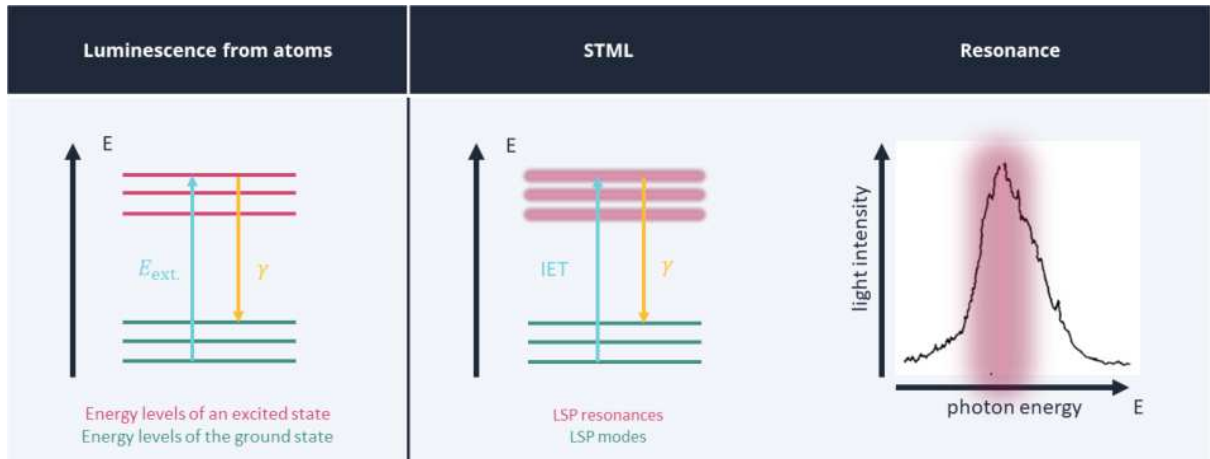


**Figure 6:** The LSP modes (middle) can be conceptually understood as analogous to energy levels in atomic systems (left), but they are not strictly bound states and can exhibit significant broadening. The excitation energy comes from the inelastic tunneling (IET). Their energy levels are typically represented as resonance frequencies (right, data are from reference [13] at  $V_t = 3.8\text{ V}$ ) rather than discrete levels. According to the different models one in 1'000 to 10'000 tunneling electrons can excite such a LSP mode.

## 2.1 Planck relation

Working with STM, the energy we give in the system is limited by the bias voltage  $V_B$ . To connect voltage with wavelengths and energies of photons emitted from the junction we use the Planck relation

$$E = h \cdot \nu = \frac{h \cdot c}{\lambda} = \hbar \omega, \quad (2.1)$$

where  $E$  is the photon energy,  $h$  is Planck's constant,  $\hbar = h/2\pi$ ,  $c$  is the speed of light,  $\omega$  is the angular frequency,  $\lambda$  is the wavelength and  $f$  the photon frequency (see Figure 7).

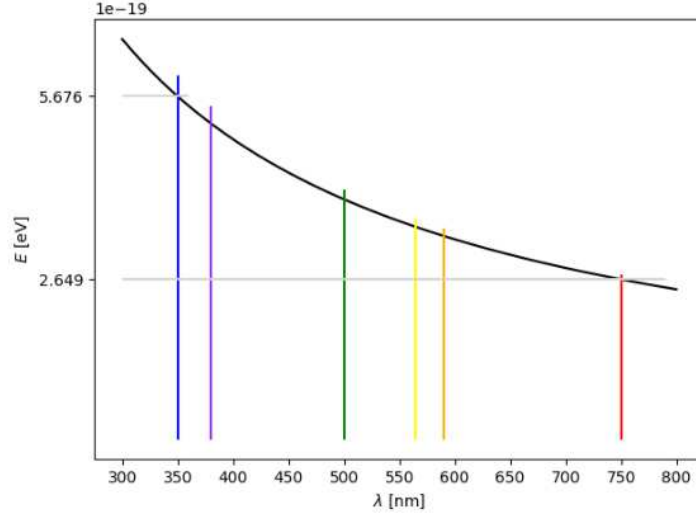


**Figure 7:** The Planck relation (see Equation 2.1). We marked the wavelengths of visible light with vertical lines of corresponding colors.

### 2.1.1 Conventional inversed photon emission

Introducing the Planck relation we remember the photoelectric effect and photoemission spectroscopy (PES) techniques describing the energy measurement of electrons emitted from samples illuminated by a photon beam. On the other hand inverse photoemission spectroscopy (IPES) uses a beam of electrons of a well defined energy directed at the sample. These electrons couple to high-lying unoccupied electronic states and decay to low-lying unoccupied states. Some of those transitions are radiative [14]. Using STM we also have an electron beam reaching a sample and emitted photons from the STM junction. But we will learn that due to the local confinement in the junction we can introduce an enhancement of the electromagnetic field leading to higher intensity resonances of decaying photons.



### 3 Historical Background of STML

To introduce the topic of STML and plasmons, we recommend starting with the review [1] and the reference [15], both summarizing papers from the beginning of STML. Taking a look at the history using NGram Viewer plot for the words "localized plasmon" and "surface plasmon polariton," we see the first big peak in 1982, a double peak in 2001/2004, and a last peak in 2012. After each peak, we found review papers for STML [1, 2, 15–17].

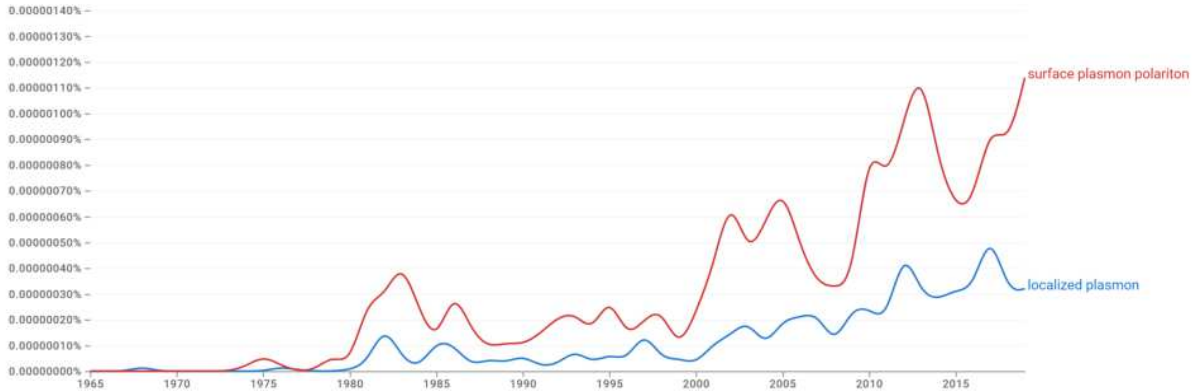


**Figure 8:** Diagram from the NGram Viewer for the keywords "Localized plasmon" and "Surface plasmon polariton" [18].

Photon emission stimulated by electron tunneling was discovered in 1976 by Lambe and McCarthy from metal-oxide-metal junctions. The emission was theoretically attributed to the radiative decay of plasmons [19]. Already in 1972, Young proposed the detection of light and secondary electrons generated by field-emitted electrons in the topografiner, a precursor of the STM [20]. The first experimental evidence of STM-induced light emission from metals and semiconductors was published in 1988 by Gimzewski *et al.*, who detected ultraviolet photons from Ta and Si(111) surfaces [1, 21].

### 4 Collective Excitations and Plasma resonance

We look at collective oscillations and plasma resonance in metals. [22]. By investigating the response of an electron gas to a time- and position dependent weak external potential with linear response theory. Considering the case of electron-hole excitations where we remove an electron from an occupied state and place it into an unoccupied one, we get a continuum of electron-hole excitation spectrum in the energy-momentum plane (see large shaded area in Figure 9).

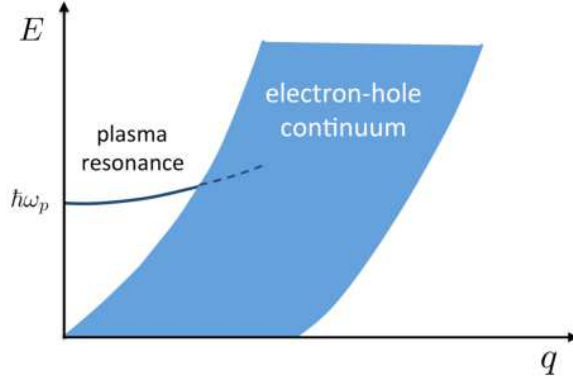


**Figure 9:** Excitation spectrum in the  $E$ - $q$  plane. The large shaded region corresponds to the electron-hole continuum and the darker line outside the continuum represents the plasma resonance which is damped when entering the continuum [22].

With Random Phase Approximation one additionally consider the Coulomb interaction amongst electrons leading to the plasma resonance which appears at rather high energies for small momenta  $q$  (see darker line in Fig. 9). Considering the limit  $q \rightarrow 0$  we get the plasma frequency

$$\omega_p^2 = \frac{4\pi e^2 n_0}{m}, \quad (4.1)$$

where  $e$  is the elementary charge,  $n_0$  is the electron density and  $m$  the mass. Plasma excitations have a well-defined energy-momentum relation and may consequently be viewed as a quasiparticle (plasmon) which has bosonic character. When the plasmon dispersion merges with the electron-hole continuum (dashed dark line in Figure 9) it is damped (Landau damping) because of the allowed decay into electron-hole excitations. This results in a finite life-time of the plasmons within the electron-hole continuum corresponding to a finite width of the resonance of the collective excitation.

It is possible to understand plasma excitation in a classical picture where one can consider negatively charged electrons in a positively charged ionic background. When the electrons are shifted uniformly with respect to the ions, a polarization results which causes an electric field acting as a restoring force. The equation of motion for an individual electron describes harmonic oscillations with the same oscillation frequency as derived above in Equation 4.1. Classically, the plasma resonance can therefore be thought as an oscillation of the whole electron gas cloud on top of a positively charged background.

We will learn, that the spectrum of light emission from the tunnel gap scales with the mean plasma frequency of the STM tip-sample system [15].

## 5 Plasmons and Models

To explain light emitted from the STM junction we need to introduce localized surface plasmons. To do so, we structure this section by following the three rows of Figure 10. First, we will explain what surface plasmon polaritons (SPPs) are. We will realize that SPPs cannot radiate light into the dielectric medium and cannot be excited directly with conventional illumination. Next, we will learn about localized surface plasmons (LSPs) and how to excite them so that they can radiate light. With theoretical models describing the LSPs we will understand their special case called tip-induced plasmons (TIPs). We use this to discuss how the radius and size of the tip will influence the light coming from the tunnel junction in the next chapter.

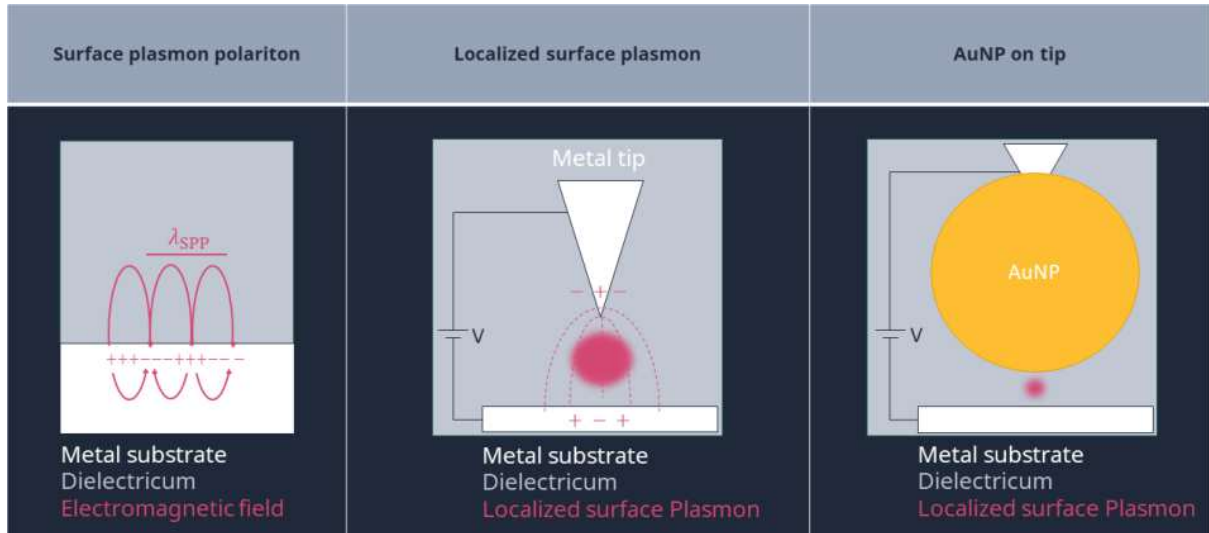


**Figure 10:** Structure of this chapter. In the first subchapter we will learn about surface plasmon polaritons and their special case of surface plasmons. We represent this section with a cropped version of Figure 11. Then we introduce the localized surface plasmon (LSP) and their special case of a dipole mode (+ and -) and finally we apply the geometry of our system.

## 5.1 Surface Plasmon Polariton (SPP)

To understand STM-induced luminescence we introduce the concept of a surface plasmon polariton in more detail in this section.

A plasmon is a bosonic quasiparticle that arises from the collective oscillation of the free electron gas density (see section 4). A polariton is a bosonic quasiparticle that arises from the strong coupling between an electromagnetic wave and an oscillation of a material's electric charge. Therefore, polaritons combine the properties of the underlying electromagnetic wave as well as the elementary excitations of matter.

A surface plasmon polariton (SPP) is an electromagnetic excitation that propagates in a wave-like fashion along the planar interface between a metal and a dielectric medium. The amplitude of the SPP decays exponentially with increasing distance into each medium from the interface. Thus, the SPP is confined to the vicinity of the interface. This confinement leads to an enhancement of the electromagnetic field at the interface. Therefore, SPPs are sensitive to surface conditions. Scanning near-field optical microscopy (SNOM) led to a breakthrough in surface polariton studies. It became possible to study SPP scattering, interference, backscattering, and localization [15].

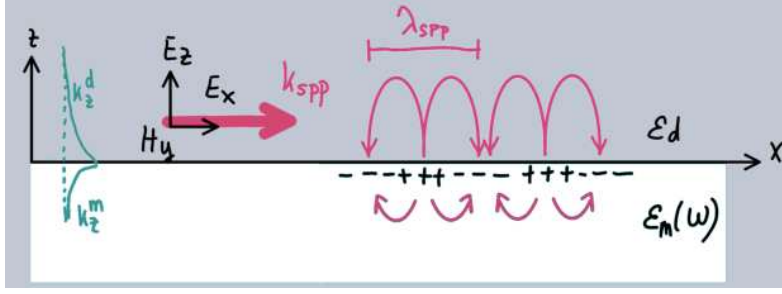


**Figure 11:** Electromagnetic excitation (curved pink arrows) that propagates in a wavelike fashion (wavenumber  $k_{SPP}$  (see Equation 5.2), wavelength  $\lambda_{SPP}$ ). The system consists of a dielectric material (gray) characterized by a dielectric constant  $\epsilon_d$  in the half-space  $z > 0$ , and a metal (white) characterized by a dielectric function  $\epsilon_m(\omega)$  in the half-space  $z < 0$ .  $k_z^{(d,m)}$  (green) determines the decay of the electromagnetic excitation with increasing distance in the material [15].

### 5.1.1 Theoretical Description of SPP

For the theoretical description we follow Zayats *et al.* from sections 1.1.1 to 1.1.4 [15]. The electromagnetic field of a surface plasmon polariton at a dielectric-metal interface is obtained from the solution of Maxwell's equations in each medium and the associated boundary conditions. Let us consider a system consisting of a dielectric material (see section 7.1 for more details) characterized by an isotropic, real, positive dielectric constant  $\epsilon_d$  in the half-space  $z > 0$ , and a metal characterized by an isotropic, frequency-dependent, complex dielectric function  $\epsilon_m(\omega) = \epsilon'(\omega) + i\epsilon''(\omega)$  in the half-space  $z < 0$  (see Figure 11).

The frequency of such electromagnetic waves can be obtained from the dispersion relation:

$$\frac{k_z^m}{k_z^d} = -\frac{\epsilon_m(\omega)}{\epsilon_d}, \quad (5.1)$$

where  $k_z^{(d,m)}$  determines the decay of the electromagnetic field with increasing distance in the material and is represented green in Figure 11. Equation 5.1 is known as a SPP and can be understood as photons coupled to collective excitations of conduction electrons near a metal surface. From this equation, we can derive the wavenumber for an SPP:

$$k_{SPP} = \frac{\omega}{c} \sqrt{\frac{\epsilon_d \cdot \epsilon_m(\omega)}{\epsilon_d + \epsilon_m(\omega)}}. \quad (5.2)$$

The real part of the wavenumber is connected to the SPP wavelength

$$\lambda_{SPP} = \frac{2\pi}{\Re(k_{SPP})}. \quad (5.3)$$

To illustrate this result, in Figure 12, we use the free electron expression (Drude) to obtain an approximation for the metal permittivity as follows:

$$\epsilon_m(\omega) = 1 - \frac{\omega_p^2}{\omega^2}, \quad (5.4)$$

where  $\omega_p$  is the plasma frequency of electron excitations.

We combine Equations 5.4 and 5.2 to

$$\omega = \frac{ck}{\sqrt{\frac{\epsilon_d \epsilon_m}{\epsilon_d + \epsilon_m}}}, \quad (5.5)$$

and plot it in Figure 12 as a solid line. To interpret this result we also plot the dispersion curve of light in the dielectric medium

$$\omega = \frac{ck}{\sqrt{\epsilon_d}}, \quad (5.6)$$

and plot it as a dotted line in Figure 12.

SPPs have a shorter wavelength than photons in vacuum at the same frequency. Hence, SPPs have a higher momentum and local field intensity.

The SPP cannot radiate light into the dielectric medium and cannot be excited directly with conventional illumination. Only if at a certain  $\omega$  the mismatch  $\delta k$  (see Figure 12) is compensated, the energy of the SPP can be converted into a photon in the far-field.

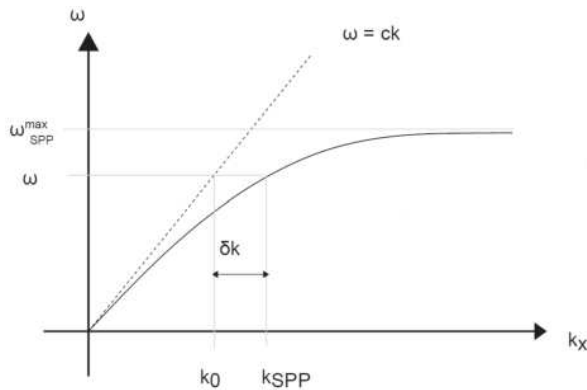


**Figure 12:** Solid line: Dispersions of SPP. Dashed line: Dispersion relation for a free propagating electromagnetic field. For the same energy, there is a mismatch  $\delta k$  in momentum [8].

## 5.2 Surface Plasmon (SP)

A subclass of SPPs is the surface plasmon (SP), which can be seen as the limiting case of SPPs. Since we have small distances in the STM junction retardation effects become negligible and we can assume that the effects are instantaneous. We can describe a surface plasmon as a delocalized and coherent electron oscillation. Equivalently, they are obtained from solutions of Laplace's equation for a scalar potential. We need a scalar potential that propagates in a wavelike fashion along a planar dielectric-metal interface, and whose amplitudes decay exponentially with increasing distance from the interface into each medium. SPs are therefore electrostatic surface waves. They are essentially non-propagating collective oscillations of the electron plasma near the metal surface.

If the metal is described by equation 5.4, the frequency of the surface plasmon can be calculated using the following equation:

$$\omega_{\text{SP}} = \frac{\omega_p}{\sqrt{\epsilon_d + 1}} \quad (5.7)$$

## 5.3 Localized Surface Polariton (LSP)

SPPs and SPs exist at a planar dielectric-metal interface. On the other hand, localized surface electromagnetic excitations can exist in special geometries, such as metallic particles or voids of

various topologies. Such surface excitations in bounded geometries are called localized surface plasmons (LSPs) or electromagnetic surface shape resonances.

The frequency of an LSP can be determined by solving Laplace's equation with appropriate boundary conditions in the non-retarded approximation. This approximation is valid if the characteristic size  $a$  of a system is much smaller than the wavelength corresponding to the LSP frequency, i.e.,  $a \ll \lambda$ . This is true for the small distances ( $a < 1$  nm) in STM junctions compared to the emitted photons in the visible range [23–26].

SPPs are a different type of excitation than LSPs. SPPs have the dispersion relation given by equation 5.2 and represent a propagating surface mode, while LSPs are confined to curved metal objects. The frequencies of LSPs are discrete, complex values that depend on the size, shape, and dielectric function of the object to which the SP is confined.

Due to the loss of translational invariance of the system, a description in terms of wavevector, as in SPPs, is not possible for LSPs. Furthermore, unlike the continuous dispersion relation in SPPs, **electromagnetic modes of the particle are discretized**. LSPs can be directly excited through incident waves, and they can be resonantly excited with light of appropriate frequency and polarization irrespective of the wave vector of the exciting light. Therefore, they effectively decay with the emission of light and can also be assigned to features on a metal surface.

Since LSPs are confined to particles or curved surfaces, they result in significant electromagnetic field enhancements at small metallic particles due to the small volume of the LSP mode. This effect contributes to numerous phenomena, such as light emission from STM tunnel junctions, enhanced scattering, surface-enhanced Raman scattering, and second-harmonic generation. LSPs also find applications in active photonic elements and apertureless scanning near-field microscopy.

## 5.4 Models describing LSP in STM

In the last section we introduced the concept of SPPs, SPs and LSPs. We want to find models describing the electromagnetic modes of our system. The exact theoretical description of the experimental situation in the STM and the localized surface plasmons is difficult. The experimental geometry of the system are two macroscopic components (tip and sample) connected with a tunneling current over a microscopic distance.

### 5.4.1 Inelastic tunneling (IET) and hot electron thermalization (HET)

To understand the following models we introduce inelastic tunneling (IET) and hot electron thermalization (HET) as described in Figure 13. Elastic tunneling ET (orange) is theoretically described in section 1.1. We remember that energy conservation is of importance describing ET. In HET we have electrons tunneling elastically and then thermalizing inside the collector electrode via plasmon generation (inelastic scattering in the sample). In IET the electrons tunnel inelastically already in the gap.

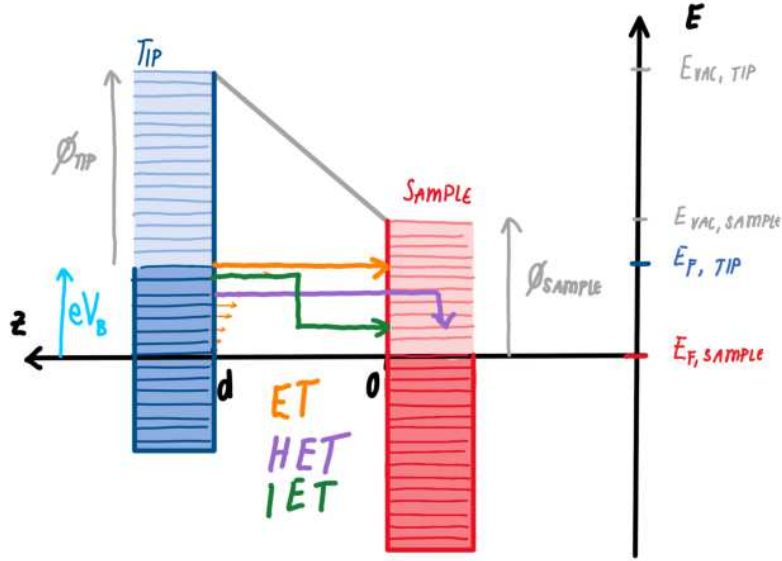


**Figure 13:** The tunnel barrier. Energy level diagram of a one-dimensional tunneling junction between tip (blue) and sample (red) states for the case of positive sample bias voltage  $V_B$ . Tunneling with energy conservation can only occur within the bias window (orange arrows) and is called *elastic tunneling (ET)*.  $\Phi$  are the workfunctions of the tip and the sample. Above the bias window, the initial states are empty, and below the final states are occupied. All energies are referred relative to the sample Fermi level. During the process of the *hot electron thermalization (HET)* we have electrons tunneling elastically and then thermalizing inside the collector electrode via plasmon generation (inelastic scattering in the sample). On the other hand when considering *inelastic electron tunneling (IET)* the electrons tunnel inelastically already in the gap.

Lü *et al.* state that finite frequency shot noise of the tunneling current can be viewed as inelastic electronic transitions between the tip and surface scattering states [27]. Shot noise is a type of random fluctuation in current that occurs when a current is carried by a stream of individual particles, such as electrons. It arises due to the random nature of the arrival of these particles at the detector or measurement device. In the case of tunneling current in STM, the electrons tunnel across a potential barrier from the tip to the sample or vice versa, creating a flow of individual electrons. The rate at which these electrons tunnel is not constant, but rather fluctuates randomly over time due to the discrete nature of electrons. Although the shot noise excitation had been suggested already in the first theoretical works by several groups it was not confirmed experimentally until 30 years later by Schneider, Schull, and Berndt [2, 28]. By writing the shot noise expression into a Fermi-golden-rule form, Lü *et al.* have established a connection with the theory of light emission in the tunneling regime, based on inelastic electronic transitions [27].

#### 5.4.2 Model of Persson and Baratoff

In this model [1, 29] electrons tunnel from an s-like orbital from the apex of the tip to a spherical free electron like metal as described in Figure 14. This geometry permits the probabilities of the competing radiative and nonradiative processes to be estimated analytically.

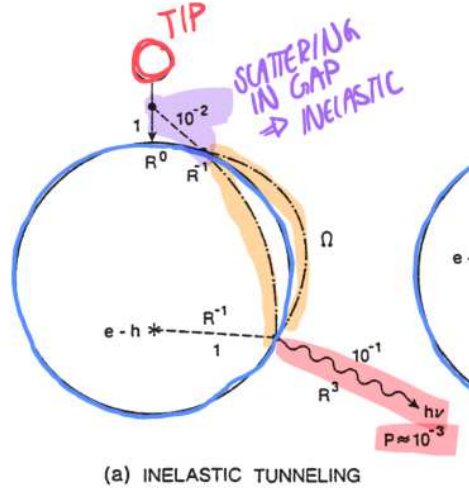


**Figure 14:** Theoretical model of Persson and Baratoff. Blue: spherical metallic particle of radius  $R$ , orange: excitation of a plasmon mode of frequency  $\Omega$ . Red: probability  $P$  (photons per electron) for photon emission after excitation of the plasmon mode. This figure summarizes the  $R$  dependences of the decay rates as well as the branching ratios for the various decay processes.

Persson and Baratoff found that there is a direct photon emission with a probability of  $P \approx 10^{-10}$  (photons per electron). The **enhanced emission occurred** if the tunneling electron excites the **Dipole plasmon resonance** of the metal particle with **IET**. Once excited, dipole resonances can decay into electron-hole pairs (e-h in Figure 14) or via photon emission (red in figure 14) with a probability for photon emission  $P \approx 10^{-3}$ . The probability for photon emission via IET is in reasonable agreement with experimental data.

For HET they calculated a probability for photon emission  $P \approx 10^{-5}$ .

#### 5.4.3 Model of Rendell

Rendell *et al.* [30, 31] treated LSP by analytically solving the Laplace equation for a metallic sphere with radius  $a$  and distance of  $d$  above a metal surface. Although several other theoretical approaches have been developed later the qualitative characteristics of the localized plasmon modes in a tunnel junction are well-described by this model [2]. The coupling between the sphere ( $\approx$  STM tip apex) and the metal surface results in a **dipole** that is aligned along the surface normal and has a maximum radiation intensity at an angle  $\theta = 60^\circ$  from the surface normal. They found that their system leads to a set of discrete modes that are confined to a region of order  $L \approx 2ad$  and have frequencies  $\omega_n$  with the mode number  $n$ . The maximum mode frequency is determined by the frequency dependence of the dielectric functions of sphere and surface [32]. Boyle *et al.* [33] qualitatively confirmed this relation by a comparison of the STML spectra of different tips with their scanning electron microscopy (SEM) images.



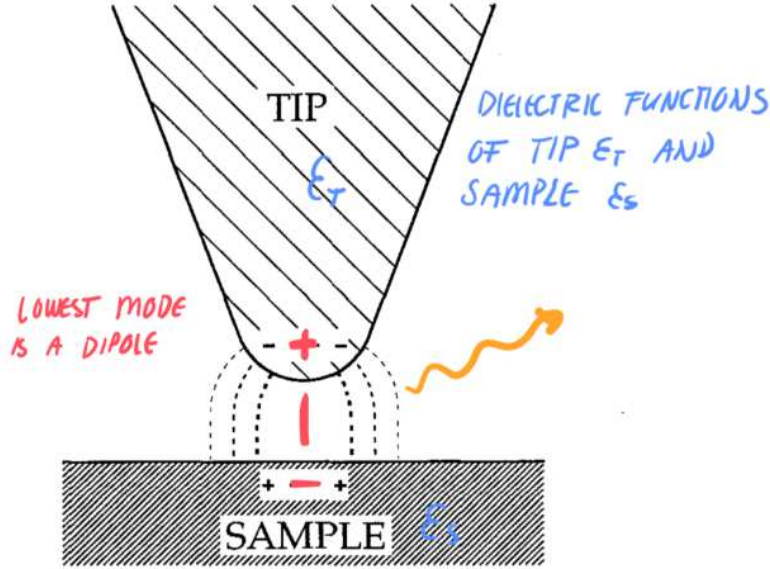


**Figure 15:** Schematic visualization of a tip-induced plasmon mode. The coupling between the tip apex and the metal surface results in a dipole aligned along the surface normal (red).

#### 5.4.4 Model of Johansson

Johansson [1, 26, 34] included the role of the tip in his theory by implementing a geometry of a spherical metal particle  $R$  above a metal film which was already used in the first theoretical study of light emission from metal-insulator-metal tunneling junctions [31, 35]. According to this model, the reason for the enhanced emission is the formation of electromagnetically coupled, localized plasmons of the tip and the sample. The **lowest-order mode, which is approximately dipolar**, gives rise to a high probability of inelastic tunneling and photon emission and they called it tip induced plasmon (TIP) mode. They used calculations with classical electromagnetic response (including plasmon resonances) to obtain the strength of field fluctuations responsible for spontaneous emission and a yield of  $10^{-4}$  photons per electron for a W tip on a Ag surface and calculated luminescence spectra reproduce many features of experimental spectra.

#### 5.4.5 Conclusion from the models

All shown models lead to a similar physical picture of STM induced photon emission. The experimentally observed intensities are consistent with **IET excitation** and radiative decay of a **localized dipolar plasmon, also called tip induced plasmons (TIPs)**.

## 6 Experimental manifestations of localized surface plasmons (LSP)

The first scanning probe microscope applied to the investigation of surface plasmon polaritons was STM. They either detected additional tunneling current induced by SPPs or the far-field scattered light.

### 6.1 Influence of LSPs on the tunneling current of STM

At the beginning Smolyaninov *et al.* realized that an **additional SPP-induced tunneling current** was observed (see Figure 16) [36]. As described above, LSPs can lead to a strong **enhancement of the electromagnetic field**, which in turn can increase the probability

of electron tunneling between the tip and the surface leading to an induced tunneling current. Localization parameters are very sensitive to the local topography and depend on it in a complex manner. As a result, the induced tunneling current can provide information about the properties of the sample surface, such as its electronic structure and topography [37].

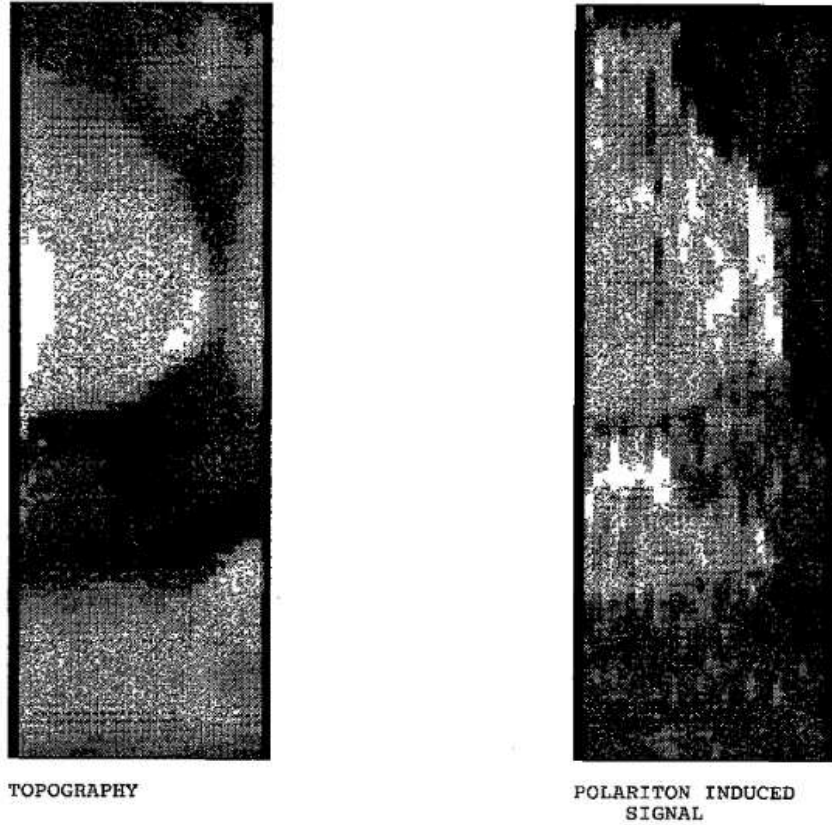


**Figure 16:**  $3.5 \times 1.2 \mu\text{m}^2$  images of an 800 nA gold film. Left: topography (vertical scale is 1200 Å from white to black), Right: LSP induced tunneling current image. The current image reveals analogous features as the topography. But the spatial variation in the tunneling current does not directly correspond to the surface height variations of the sample. This is likely due to the fact that the excitation of LSPs depends on the local electromagnetic field at the surface, which can be influenced by the topography of the sample [36].

The nonlinearity of the current-voltage characteristic of a tunnel junction and the corrections coming from the enhanced electromagnetic field give rise to induced tunneling currents of the same order of magnitude [38]. Such an induced current  $\Delta I$  is calculated as followed

$$\Delta I = \frac{1}{4} \Delta V^2 \frac{d^2 I_t}{dV_t^2}, \quad (6.1)$$

where  $\Delta V$  is the electromagnetic field induced voltage, and  $V_t$  is the tunneling voltage [39]. We notice the second derivation  $d^2 I/dV^2$  corresponds to the concept of inelastic tunneling.

## 6.2 Light emission

The STM induced light emission from metal surfaces involves localized surface plasmons (LSP) which are excited in the gap between the tip and the sample by inelastic tunneling electrons.

### 6.2.1 Historical plot and explanations

ma Gimzewski *et al.* observed the following points in the spectras of Figure 17:

1. The spectral distribution reveals a distinct high-energy threshold of photon emission at  $h\nu = eV_t$ , as expected for electron-tunnelling stimulated light emission.
2. Two characteristic emission peaks at  $h\nu = 1.9\text{eV}$  and  $h\nu = 2.4\text{eV}$  are observed in the spectra.
3. The intensities of the resonances, but not their energetic position, vary with tunnel voltage in a nonmonotonic manner. The  $1.9\text{eV}$  peak, for example, appears to be prominent in the  $V_t$ -range 2.5 V to 3.0 V and then again close to 5 V.

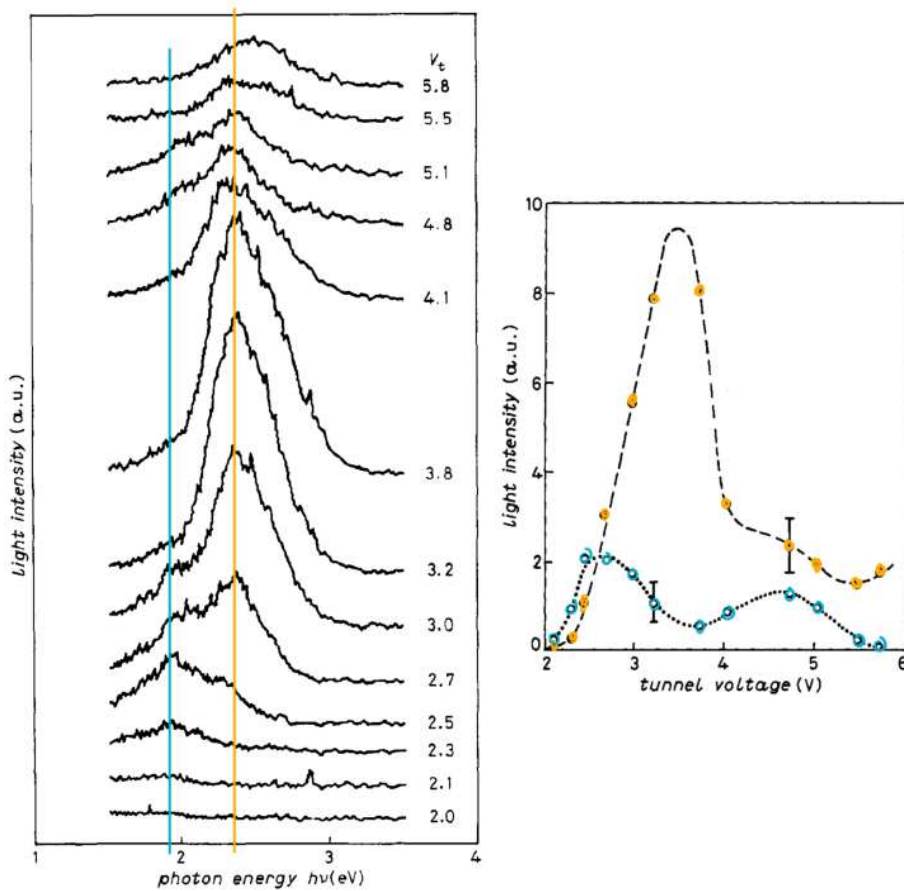


**Figure 17:** Left: Absorption spectra reported for Ag films and W tips. They discovered characteristic maxima of the photon emission at  $1.9\text{eV}$  and  $2.4\text{eV}$ , independent of tunnel voltage. Right: Photon intensity of the two resonance structures at  $h\nu = 1.9\text{eV}$  (open circles) and  $h\nu = 2.4\text{eV}$  (filled circles) as a function of tunnel voltage. The lines are a guide to the eye only [13].

**6.2.1.1 Explanations of observation 1** In general they saw, that the highest photon energy observed is limited by the electron energy  $E = eV_t$  as we know from the Planck relation introduced earlier and corresponds to the maximum energy that one electron can lose in an inelastic tunnelling process between the tip and the sample. In more recent papers we found

the word quantum cut-off describing the same observation. In Figure 19b) Martín-Jiménez *et al.* marked this threshold with a white oblique line and vertical lines in Figure 19c). If we apply for example 1.5 eV, we will not have enough energy to excite any visible light. In Figure 18 we excluded the electron charge from the energy to compare the wavelengths to the voltage applied in the STM.

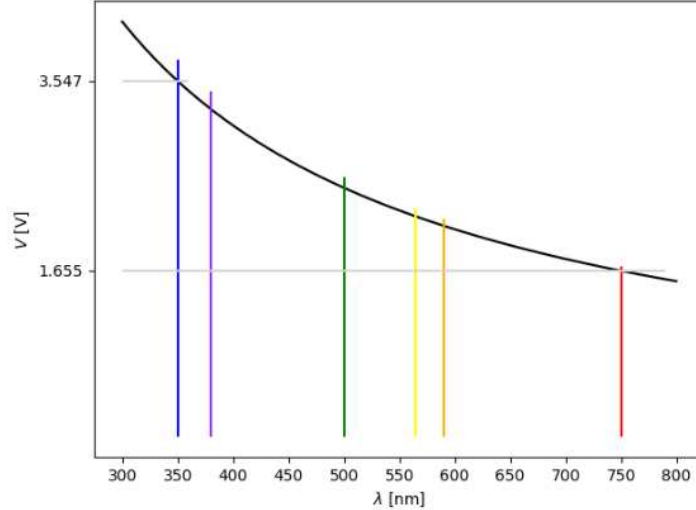


**Figure 18:** The Planck relation (see Equation 2.1). We excluded the electron charge from the energy to compare the wavelengths to the voltage applied in the STM. We marked the wavelengths of visible light with vertical lines of corresponding colors.

For sufficiently high voltages (above 3.2 V in Figure 19c)), tunnelling electrons have enough energy to excite all the localised plasmonic modes supported by the nanocavity, and the quantum cut-off is no longer relevant [40].

**6.2.1.2 Explanations of observation 2** In Figure 17 on the left they found two maxima of the photon emission at 1.9 eV and 2.4 eV, independent of tunnel voltage. Already back then, they attributed the maxima to resonant excitation and radiative decay of localized surface plasmon modes. Previously we learned, that models describing this effect lead to the physical picture of **inelastic tunneling excitation** and radiative decay of a **localized dipolar plasmon, also called tip induced plasmons (TIPs)** consistent with the experimentally observed intensities. This means we have a dipolar plasmon peak, arising from the excitation of dipolar plasmons. But as written in section 7.2, also higher order like quadrupolar plasmons can be excited. Similarly to dipole modes, quadrupolar plasmons involve the collective oscillation of electrons in a manner similar to an electric quadrupole [41, 42]. They assigned the peak at 1.9 eV to higher order modes [42]. Often higher order modes have higher energy (shorter wavelength) [43]. Also for the system chosen for Figure 19, the interaction of tunneling electrons with quadrupolar plasmons results in luminescence emitted at a shorter wavelength.

They excluded a process coming from conventional inverse photoemission spectroscopy (IPES, see section 2.1.1) since such processes have a very low photon yield. The energy dissipation for intermediate states populated with elastic tunneling in a metal, proceeds almost exclusively via nonradiative electron-hole pair excitation.

**6.2.1.3 Explanations of observation 3** To investigate point number three, they plotted the photon intensity of the two resonance structures at  $h\nu = 1.9\text{ eV}$  (open circles) and  $h\nu = 2.4\text{ eV}$  (filled circles) in Figure 17 on the right as a function of tunnel voltage. They observed that the photon peak at  $h\nu = 1.9\text{ eV}$  has a minimum as the tunnel voltage approaches the bulk plasmon energy ( $h\nu = 3.76\text{ eV}$ ) and surface plasmon energy ( $h\nu = 3.66\text{ eV}$ ), whereas the photon peak at  $h\nu = 2.4\text{ eV}$  shows a maximum in this tunnel voltage region.

**6.2.1.4 High-bias intensity suppression** As a next step we were wondering, why the intensity starts decreasing again for bias voltages higher than 4.1 V since the energy should be still in the system. The high-bias (larger than 3.8 eV) intensity suppression has been previously reported for voltages at which tunnelling into bulk states on the noble metal surface or field-emission resonances happen. Both of these causes result in a significant increase in the tunnelling conductivity. To counteract the increase in conductivity and maintain a constant tunnelling current, the tip-sample distance is enlarged under closed feedback conditions and the plasmonic modes decay [40].

**6.2.1.5 Change in peak positions** We observed that the energy peak at 2.4 eV seems to shift to higher energies for bias voltages over 4.1 V even though they wrote in the third observation that the peaks stay at the same energies. In the paper of 2020 [40] they described the shift of the peak in Figure 19d) and e). In d) they compare the spectra taken with a bias voltage of 3.3 V in red and 4.0 V in violet. The low-energy contribution shifts to higher energy by about 25 meV, whereas the shift of the high-energy contribution by 55 meV. This behaviour is not expected on the grounds of EM calculations, which predict a much similar shift for both contributions (blue line in Fig. 1d). It is worth noticing that modifying the stabilisation voltage under closed feedback conditions has the effect of changing the tip-surface distance and, thus, the optical response of the nanocavity. On the other hand, as mentioned in the introduction, STML spectra are also affected by the electronic properties of tip and sample. In order to distinguish between those two effects, it is worth comparing STML spectra with the variations in the far-field light intensity as obtained by EM calculations.

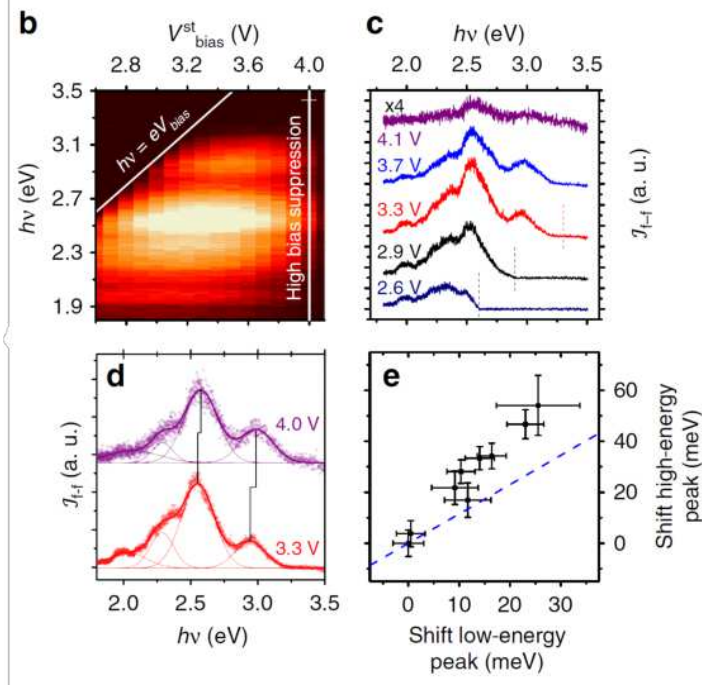


**Figure 19:** STM luminescence experiments performed in *source*. They used a gold tip and a Ag(111) substrate. *b*) Light intensity emitted for a particular tip configuration as a function of the photon energy and the stabilisation voltage. Quantum cut-off and high-bias suppression are marked by white lines. *c*) Individual spectra recorded for different stabilisation voltages. The quantum cutoff condition for each voltage (where relevant) is marked by a vertical line. The spectra have been vertically offset to enhance visibility, and the spectrum for a bias voltage of 4.1 V (above the high-bias cutoff) has been scaled to facilitate comparison. *d*) Shift of the peak energies, extracted through the fitting to Gaussian lineshapes, with bias voltage. *e*) Proportionality between the energy shifts of the low- (dipolar plasmon) and high- (quadrupolar plasmon) spectral peaks. The blue dashed line corresponds to the expected trend from our EM calculations. Errors are estimated from the residual values of the fitting as the standard deviation of the fitting parameters [40].

## 7 Experimental considerations

### 7.1 Dielectric constant or permittivity

The dielectric constant (absolut  $\epsilon$  and relative  $\epsilon_r$  permittivity,  $\epsilon_r = \frac{\epsilon}{\epsilon_0}$  with the vacuum permittivity  $\epsilon_0 = 1$ ) is a measure of the electric polarizability of a dielectric. A material with high permittivity polarizes more when an electric field is applied and stores more energy in the material than a material with low permittivity.

We can investigate the response of an electron gas to a time- and position-dependent weak external potential  $V_a(\vec{r}; t)$  by solving the equation of motion with a linear response and a dynamical linear response function  $\mathcal{X}_0(\vec{q}, \omega)$  (the Lindhard function). If we additionally include the coulomb interaction we have to introduce an effective potential

$$V(\vec{q}, \omega) = \frac{V_a(\vec{q}, \omega)}{\epsilon(\vec{q}, \omega)}, \quad (7.1)$$

where  $\epsilon(\vec{q}, \omega)$  is the dynamical dielectric function and describes the renormalization of the external potential due to the dynamical response of the electrons in the metal. It is related to the

susceptibility

$$\epsilon = (1 + \mathcal{X})\epsilon_0 \quad (7.2)$$

and we can write it as

$$\epsilon(\omega) = \epsilon'(\omega) - i\epsilon''(\omega) \quad (7.3)$$

and it satisfies the Kramers-Kronig relations. At a given frequency, the imaginary part,  $\epsilon''$ , leads to absorption loss if it is positive and gain if it is negative. If we consider the limit  $\vec{q} \rightarrow 0$  for  $\epsilon(\vec{q}, \omega)$  we get

$$\epsilon(\vec{q} \rightarrow 0, \omega) = 1 - \frac{\omega_p^2}{\omega^2} \quad (7.4)$$

with the plasma frequency we introduced in equation 4.1 [22].

To use this concept for plasmonic materials we found two references (from 1972 [44] and 2020 [45]) describing experimental methods of measuring the dielectric constant of noble metals (see Figure 20).

The dielectric constant is determined by the relaxation time  $\tau$  (or direct current conductivity) and the optical mass of the electrons according to the Drude free-electron theory

$$\tilde{\epsilon}(\omega) = 1 - \frac{\omega_p^2}{\omega(\omega + i/\tau)}. \quad (7.5)$$

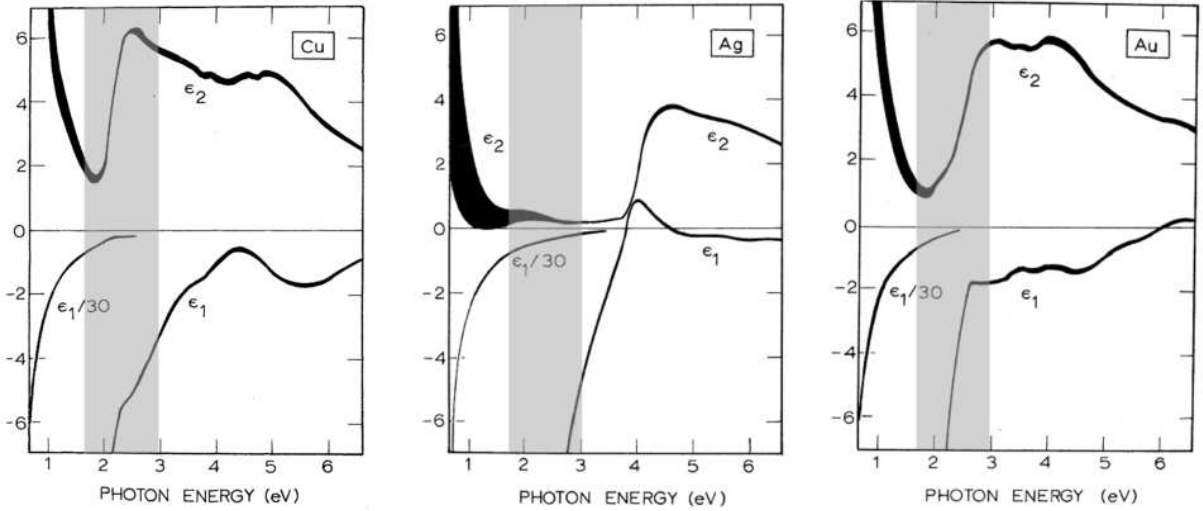


**Figure 20:** Dielectric constants for copper, silver and gold as a function of photon energy. The visible spectrum is approximately marked in gray. The width of the curves is representative of the instrumental error [44].

Separating equation 7.5 into its real and imaginary parts and considering near-infrared frequencies we find

$$\epsilon' \approx 1 - \frac{\omega_p^2}{\omega^2} = 1 - \lambda^2 \lambda_p^2 \quad \text{and} \quad \epsilon'' \approx \frac{\omega_p^2}{\omega^3 \tau} = \frac{\lambda^3}{\lambda_p^2} 2\pi c \tau \quad (7.6)$$

Johnson *et al.* used this to plot Figure 21.

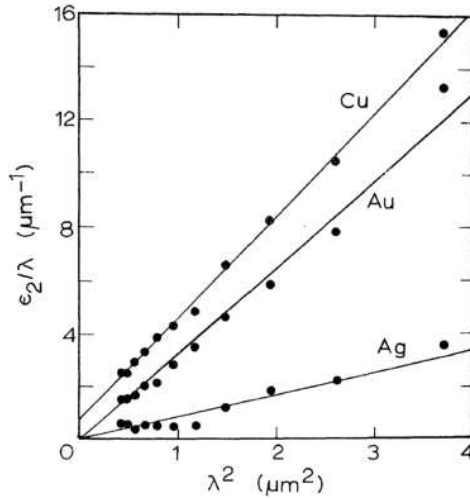


**Figure 21:** Imaginary part of the dielectric constants for copper, silver and gold, divided by wavelength vs the square of the wavelength [44].

Finally, Giannini describes in reference [46], that at visible wavelengths, the permittivity of noble metals decreases and approaches  $\epsilon_d$  in equation 5.2. This causes the real part of the denominator to vanish. EM fields then experience a fast decay along the normal direction into the dielectric material. This leads to the concentration of EM energy into subwavelength volumes at the surface of the metal and overcomes one of the main constraints of classical optics, the diffraction limit.

Among the three metals that display plasmon resonances in the visible spectrum (Ag, Au, Cu), Ag exhibits the highest efficiency of plasmon excitation and it is the only material whose plasmon resonance can be tuned to any wavelength in the visible and near infrared (NIR) range by modifying Ag NP's morphology [42, 43].

By controlling the dielectric constant of the surrounding medium, the wavelength of the localized surface plasmon resonance can be finetuned to a desired position, as is shown in Figure 8.

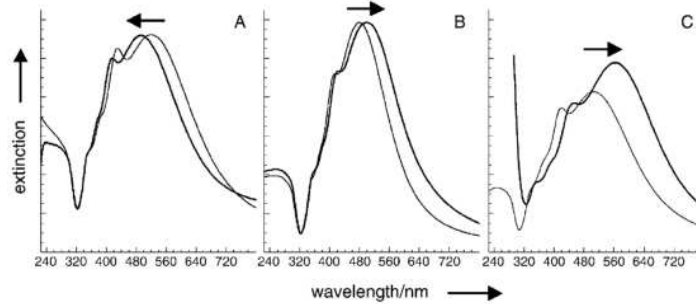


**Figure 22:** Extinction spectra of silver nanoparticle suspensions before (thin lines) and after (thick lines) changes were made to the dielectric environment from A) isopropanol to Teflon AF, B) water to silica, and C) water to titania [42].

## 7.2 Tip size

Already in the introduction we mentioned that the tip shape influences the spectra. In Figure 2 we see that the seemingly small difference in the tip leads to hundred times higher light intensity coming from the junction.



In the model of Rendell (see section 5.4.3) they found that the maximum mode frequency is determined by the frequency dependence of the dielectric functions of sphere and surface [32]. Boyle *et al.* [33] qualitatively confirmed this relation by a comparison of the STML spectra of different tips with their scanning electron microscopy (SEM) images. While the STML spectrum of their sharpest tip with a radius of curvature of  $\approx 15$  nm extended up to the near-infrared ( $1.3 \mu\text{m}$ ) and an energy of 0.95 eV, tips with large radii of curvature of  $\approx 100$  nm extended further into the infrared ( $1.7 \mu\text{m}$ ) and an energy of 0.73 eV. Furthermore, these experiments indicate that blunter and less symmetric tips result in more complex STML spectra with more emission peaks and higher emission intensities. Comparable experiments by Meguro *et al.* [47] and Raschke and Lienau [48] made similar observation.

In more recent papers [42, 43] we learn about higher order plasmons. Already Mie described the different plasmon modes in spherical gold and silver particles [41]. We can use this knowledge to apply it on the STM junction where the tip is modeled as a sphere. For localized surface plasmons the EM field is uniform across a particle such that all the conduction electrons move in-phase producing only dipole-type oscillations (Figure 23A) manifested by a single, narrow peak in the spectrum. As the size increases, the field across the particle becomes nonuniform, and this phase retardation broadens the dipole resonance and excites higher multipole resonances, such as the quadrupole, octupole, etc. (Figures 23B,C) leading to several peaks in the spectra. Most investigations have been focused on the dipolar and quadrupolar resonances in the small particle size regime (2 nm to 100 nm).

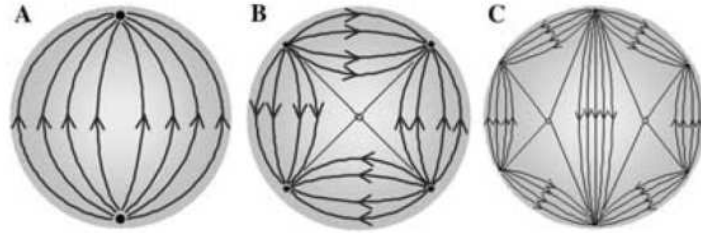


**Figure 23:** Diagrams depicting the electric field lines of the A) dipole, B) quadrupole, and C) octupole resonances [41, 42].

In Figure 24 extinction spectra of Ag suspensions of different particle diameters are shown. It is apparent that the dipole maximum rapidly shifts to longer wavelengths as the particle size increases beyond 70 nm revealing the quadrupole peak at about 420 nm. A sufficiently small particle of any conducting material exhibits resonances, yet its spectral position depends on many factors, most importantly on the material's frequency-dependent complex dielectric function [42] (see section 7.1).

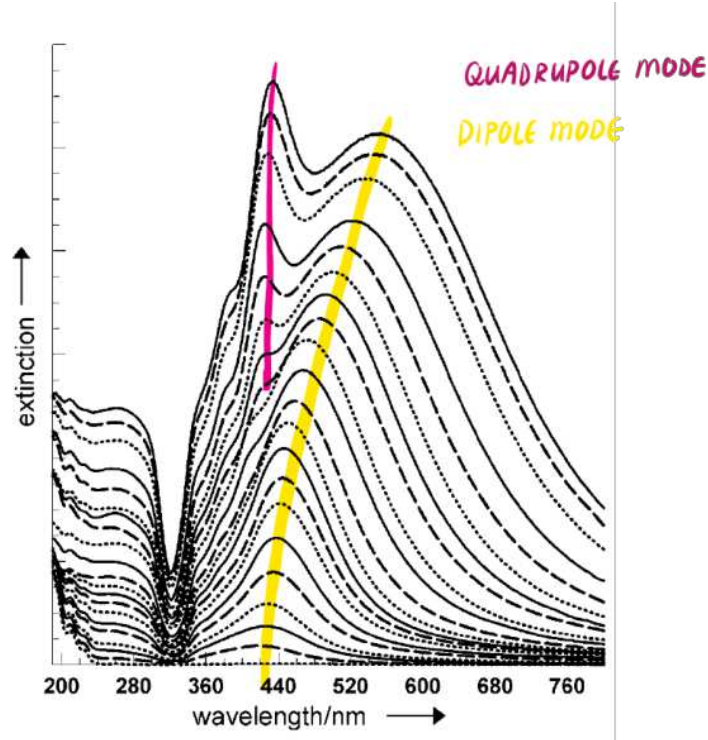


**Figure 24:** Extinction spectra of silver nanoparticle suspensions of 20 different particle diameters [42]. This is a summary of the spectra found in reference. The particle sizes are 29, 34, 37, 44, 48, 52, 58, 61, 75, 78, 92, 97, 105, 113, 120, 135 (all in nm) [49].

In the paper from 2020 [40] we found this concept used on STML spectra. Their results are in Figure 25 of a modelled STM junction where they identified the two radiative modes responsible for the far-field maxima as dipolar c) and quadrupolar d) gap plasmons. They additionally observed, that the spectra for small radii present two maxima, around 2.3 eV and 3.1 eV, that resemble with remarkable accuracy the experimental curves. For larger tip sizes, only the low-energy (dipolar) peak is apparent. Notice that this peak redshifts with larger  $R$ . All these results are robust against subtle variations of tip geometry and are preserved for more realistic tip geometries. The two maxima vary in opposite ways (the dipolar peak sharpens and increases while the quadrupolar one broadens and decreases) as the gap is reduced.

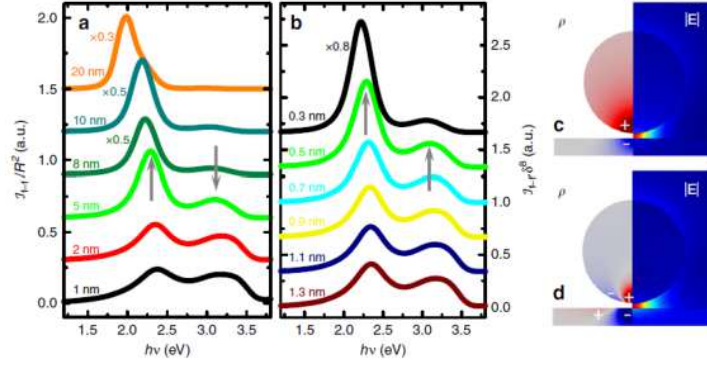


**Figure 25:** Modelling the tip-surface nanocavity. Theoretical far-field spectra for nanocavities comprising a gold sphere (tip) on top of a silver flat surface (substrate). a) Spectra for different sphere radii,  $R$ , and 0.5 nm gap size. b) Spectra for different gap size and fixed sphere radius,  $R = 5$  nm. The green curve plots the same spectrum in both panels. c) and d) render induced charge distribution (left) and electric field amplitude maps (right) for the two radiative plasmonic modes c) dipole and d) quadrupole behind the far-field peaks indicated by grey arrows in a), b) [40].

### 7.2.1 Adding plasmonic particles on a STM tip

We found examples of references, where single gold particles were applied at a tip. Kalkbrenner *et al.* [50] reported the reproducible application of single gold nanoparticles of 100 nm at the end of sharp glass fibre tips. Their idea was similar as ours, to construct a well-characterized and well-controlled tip by using a single nanoscopic metal particle of known size and material as a local scatterer. Before mounting the fibre tip in the SNOM it is placed in a solution of polyethylenimine for about 30 min in order to adsorb a monolayer which acts as a glue for our gold particles. Therefore, when the fibre tip establishes contact with a gold nanosphere it lifts the particle, and a probe as shown in Figure 26b) is obtained.

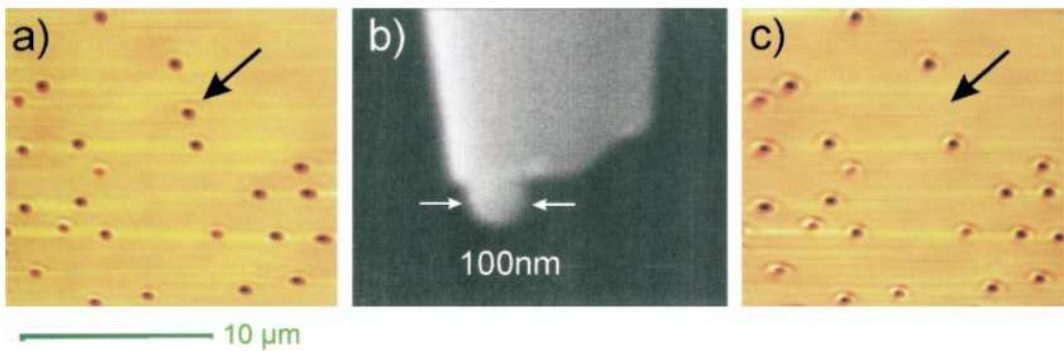


**Figure 26:** a) Confocal scan of individual gold spheres of 100 nm diameter spread on a glass substrate. A fibre tip has been approached to the particle indicated by the arrow using shear-force control. After establishing contact to the gold sphere the particle has been fixed to the tip. b) Scanning electron micrograph of the tip after the procedure described in a). c) Confocal scan of the same area as in a), verifying that the chosen particle has left the substrate. Its former position is indicated by an arrow. [50].

Also Novotny *et al.* [51] attached single 80 nm gold nanoparticles at the end of a pointed optical fibre. Their experimental setup and a SEM picture of the tip is shown in Figure 27.

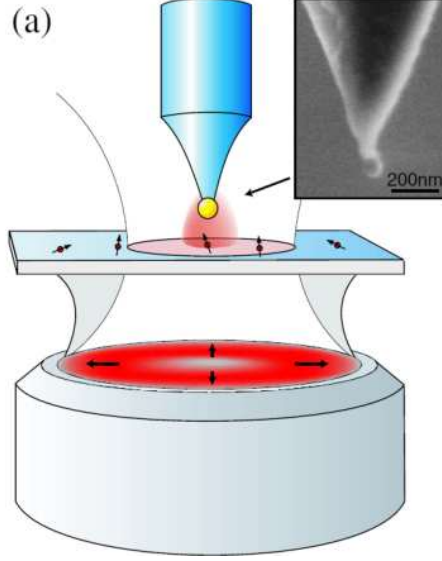


**Figure 27:** Inset: SEM image of a gold particle attached to the end of a pointed optical fiber [51].

### 7.3 Quantum efficiency

To compare the results obtained in an experiment the experimental quantum efficiency  $\eta_{\text{exp}}$  was introduced. It represents the number of detected photons per tunneling electron

$$\eta_{\text{exp}} = \frac{Je}{I}, \quad (7.7)$$

where  $J$  is the detector's photon counting rate,  $I$  is the electric current and  $e$  is the elementary charge. It relates to the real quantum efficiency  $\eta_0$

$$\eta_{\text{exp}} = \eta_0 \eta_{\text{em}} \eta_{\text{trans}} \eta_{\text{det}} \frac{\Omega}{2\pi}, \quad (7.8)$$

where  $\frac{\Omega}{2\pi}$  is the geometric collection coefficient for the solid angle  $\Omega$  covered by the optical system assuming an isotropic emission. The real quantum efficiency is for example  $P \approx 10^{-3}$  marked red on the bottom right of Figure 14.  $\eta_{\text{em}}$  and  $\eta_{\text{trans}}$  are the coupling probabilities from the tunnel junction to the far-field and the transmission probability through the coupling optics to the detector, respectively.  $\eta_{\text{det}}$  is the detection efficiency of the detector [2].

#### 7.3.1 Angle of Light emission

Angular distributions of the photons emitted from metals are described by the emission pattern of an oscillating electric dipole above a surface (see section 5.4.3). Most of the light is emitted at an angle of  $\approx 30^\circ$  with respect to the surface into an azimuthal ring of  $\approx 30^\circ$  polar width (see Figure 28) [1]. In section 7.2 we also learned about quadrupolar modes. Their emission characteristics, including the emission angle, can differ from those of dipolar modes. The emission properties of quadrupolar modes depend on the specific geometry and symmetry of the plasmonic structure.

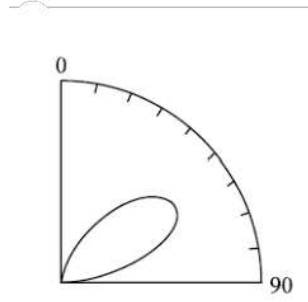


**Figure 28:** Angular distribution of the photons emitted from metals [30]

- Most of the light is emitted at an angle of  $\approx 30^\circ$  with respect to the surface into an azimuthal ring of  $\approx 30^\circ$  polar width.

As the light emitted from the tunnel junction can be considered to originate from a point source emitting photons into the hemisphere above the sample, a large collected solid angle would be ideal to ensure efficient detection of the photons. This can be partly achieved by placing a photomultiplier or an optical fiber (see Figure 29a)) close to the tunnel junction, an approach realized for experiments under ambient conditions. In ultra-high vacuum (UHV), lenses (see Figure 29b)), or ellipsoidal reflectors (see Figure 29c)) have been employed [16]. Mirrors can provide the largest solid collection angle but are not easy to adjust. Fibers do not allow a large collection angle, and only specific fibers preserve the polarization and photon timing of the emitted light [2].

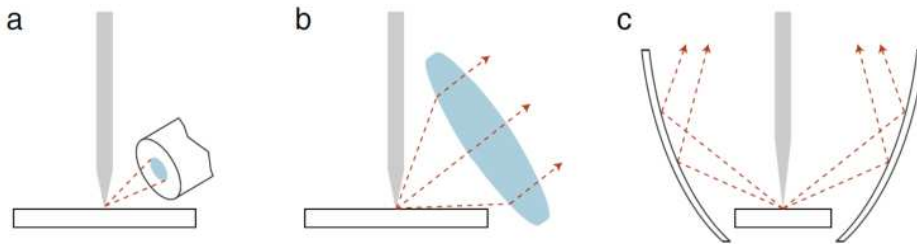


**Figure 29:** Different concepts for collecting photons emitted from the tunnel junction. The larger the acceptance solid angle, the higher the measured light emission intensity. (a) Optical fiber. (b) Lens. (c) Reflection mirror [16].

# Part III

## Experimental Section

### 1 Introduction

We want to build a setup for STM luminescence measurements. Luminescent STM is a powerful technique that combines the high-resolution imaging capabilities of STM with the ability to detect and map the optical emission of a sample at the nanoscale. To perform such measurements we need a plasmonic tip as well as an optical setup to detect photons. In this section we describe all the experiments we performed to perform the final experiment: Measure photon intensity with a Pt/Ir tip on AuNPs, pick up a AuNP for tip functionalization, measure again the photon intensity with the functionalized tip. Since we performed a series of experiments that led from one to another, we decided to structure the experimental section as shown in Figure 30 and describe everything in a short manner in the introduction. Picture of the experiments and futher descriptions are linked with the box.

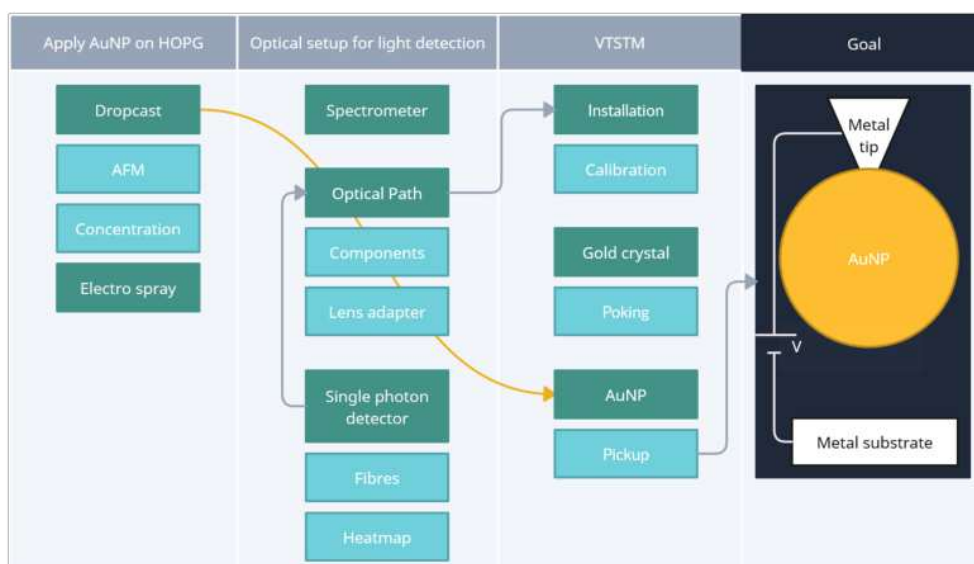


**Figure 30:** Structure of the experimental section. (1) The first part of the thesis was to figure out how to **apply the gold nanoparticles (AuNPs) on HOPG**. After performing Dropcast experiments we were checking the results with the AFM. To use this method for the STM we had to find a suitable particle concentration. We also considered the Electro spray but it was more involved than anticipated, so we focused mainly on the dropcast techqnie. (yellow arrow). (2) Then we figured out an **optical setup** to collect the emitted light from the STM junction, direct it outside the chamber and collimate the beam on a fibre connected to the single photon detector (SPD). We figured out which lenses and componets were necessary to perform the experiments and which made the experimental process easier. To plot the photon counts we programmed heatmaps. At the beginning we performed experiments with a spectrometer instead of the SPD but it was was not sensible enough to detect our collected photons. (3) We installed everything at an old **VTSTM** after we callibrated the x-/y- and z-directions with HOPG. We tested and verified the system by using a gold crystal and functionalized our tips by indenting them in the gold crystal. As a final steps we were picking up gold nanoparticles and comparing the emitted light before and after tip functionalization.

## 1.1 Application of AuNP on HOPG

### Experiment 1.1: Electrospray

To perform STM luminescence measurements we need a plasmonic tip as well as an optical setup to detect photons. To functionalize the tip we will pick up gold nanoparticles (AuNPs) from HOPG. We planned to deposit AuNPs to HOPG using two methods: dropcasting and with an electro spray. However, building up the electro spray was more involved than anticipated, so we focused mainly on the dropcast technique.

### Experiment 1.2: Dropcast

To perform STM luminescence measurements we need a plasmonic tip as well as an optical setup to detect photons. To functionalize the tip we will pick up gold nanoparticles (AuNPs) from HOPG. We planned to deposit AuNPs to HOPG using two methods: dropcasting and with an electro spray. For the dropcast experiments, after applying the first drops of AuNPs onto HOPG and observing their circular staining patterns as they dried, we inserted the samples into the AFM for further investigations.

### Experiment 1.3: AFM measurements

After applying the first drops of AuNPs onto HOPG with the Dropcast method we made the following observations using the AFM: (1) the particles arranged themselves in a layer rather than piles, (2) the distribution of particles was uneven, with clusters in cracks of the HOPG and at the circumference of the drop, (3) we do not have enough particle density to perform STM measurements which have a scan range of  $1\ \mu\text{m}$  requiring at least 10 to 100 particles in that range, and (4) there was a lot of water on the surface that we needed to remove. Hepperle et al. made similar observations discussing different application methods of AuNPs on a carbon foil and comparing dropcasting and spin coating [52]. The observations in (2) are called coffee rings [53].

### Experiment 1.4: Concentration

From our AFM measurements we concluded that we do not have enough particle density to perform STM measurements. The scan range of our STM is with  $1 \times 1\ \mu\text{m}^2$  smaller than the scan range in the AFM ( $10 \times 10\ \mu\text{m}^2$ ). To successfully detect particles, the scan range of the STM should have at least 10 to 100 particles. We were not able to use the coffee rings to increase particle density because it was not reproducible enough for STM. We wondered if the effect of gravitational sedimentation could be used to concentrate the solution [54, 55], but we did not investigate further due to the timescale of sedimentation and lack of instruments like centrifuges. We tried heating experiments to evaporate the water and densify the solution, but we observed the formation of gold clumps. In the end, we bought denser particles with OD100 instead of OD1. To insert the particles into the STM, we mixed  $4\ \mu\text{L}$  of OD100 particles with  $1\ \mu\text{L}$  of OD1 particles, dropcasted  $1\ \mu\text{L}$  of this mixture onto HOPG ZYA, heated the sample up to  $120\ ^\circ\text{C}$  for 20 min and left it in a desiccator overnight.

## 1.2 Optical Setup

### Experiment 2.1: Spectrometer

Initially, we attempted to quantify the emitted light using a USB2000+ Fiber Optic Spectrometer by directly pointing a fiber at the junction under ambient pressure and room temperature. However, despite observing light with a light-sensitive camera, we were unable to detect it with this setup.

### Experiment 2.2: Single photon detector

Since the spectrometer was not sensitive enough we ordered a single-photon detector. We tried to quantify the emitted light from the junction measured under ambient pressure and room temperature with three different fibers.

### Experiment 2.3: Fibres

We used the single photon detector to quantify the photons emitted from the junction. The fibres connected to the detector were pointing directly to the junction. The measurements we performed were under ambient pressure and at room temperature. After some tries we were finally able to detect the light with the light sensitive camera as well as photoncounts from the single photon detector.

### Experiment 2.4: Heatmap

Using the single photon detector we generated heat maps to establish a relationship between the applied bias voltage, the tunneling current and the detected photon counts. We tried to gradually change the system (different fibres, different angles, different fibres) to optimize the collected photon yield. But since the measurements were performed in air the system was not reproducible enough to optimize the yield reliably.

### Experiment 2.5: Optical Path

To make the system suitable for STM measurements performed in vacuum, we relocated the fiber outside of the STM head and the chamber. The challenge was to connect the emitted light from the junction to the fibre.

### Experiment 2.6: Components and lens adapter

To make the collection of photons suitable for vacuum measurements we chose to relocate the fibre outside the chamber. To collect the light coming from the STM junction we had to place a lens in the vacuum collimating the light from the junction into a parallel beam. Ales designed and 3D printed a lens holder fixing such a collimating lens at the sample holder with the applied metal substrat. The collimated beam was directed out of the STM chamber through a viewport and collimated back on the fibre. To verify and optimize the setup we used cameras and beamsplitters. With this setup, we were able to complete the remainder of our experiments.



## 1.3 VTSTM

### Experiment 3.1: VTSTM

After conducting experiments with the AFM, we attempted to insert particles into our group's STM. However, the piezos had limited range and were unable to reach the drop-casted particles on the HOPG. After the summer break, we obtained an 1993 Variable temperature STM by courtesy of Prof. Dr. Karl-Heinz Ernst that we moved from EMPA to UZH and set up in our laboratory. To perform the planned STM luminescence experiments we added the viewport and the optical system with the single photon detector to the STM chamber.

### Experiment 3.2: Calibration

I learned how to use VTSTM. Since the displacement of the scanner piezo in the x,y and z directions does not have a one-to-one correspondence with the applied voltage we calibrated the x, y and z channels of the scanner piezo using a sample of highly oriented pyrolytic graphite (HOPG) in a vacuum of  $\approx 10^{-7}$  bar.

### Experiment 3.3: Gold crystal

After installing and calibrating the VTSTM, we conducted experiments in a vacuum using a gold crystal and a light-sensitive camera. To verify our setup we performed the first experiments with Pt/Ir tips we indented in a gold crystal. We successfully observed light with the functionalized tip on the gold crystal as a substrate. Similarly, we also observed light with the same tip coming from AuNP applied on HOPG as a substrate. We wanted to quantify the light emission.

### Experiment 3.4: Poking

With the intention to pick up gold particles from the HOPG we learned how to use the "Nanostructuring" function of the STM. We scanned the gold crystal, poked the crystal with different voltages, currents and hight settings and afterwards scanned the crystal again to get a feeling of poking in gold.

### Experiment 3.5: Picking up AuNPs

After we dropcast the gold nanoparticles to the HOPG we inserted it to the VTSTM. We used the "Nanostructuring" function of the STM and the experience we collected from poking gold to lift up single AuNPs

### Experiment 3.6: Goal

After all the experience we gained, we were able to perform the final experiment: (1) We dropcast the right amount of particles on HOPG added on a sampleholder to (2) insert the sampleholder with the lensholder in the VTSTM. (3) We prepared a Pt/Ir tip and installed it to (4) collect photons coming from the junction of Pt/Ir tip with AuNPs on HOPG. We detected the darkcount rate of the room. (5) Then we functionalized the same tip at the same location by picking up one AuNP to (6) successfully collect photons coming from the junction of functionalized Pt/Ir tip with AuNPs on HOPG.

## 2 Samples

### 2.1 Gold Nanoparticles (AuNP)

To perform STM luminescence experiments we need a functionalized tip. Usually W or Pt/Ir tips are forcefully indented in a gold or silver crystal. We wanted to test another approach by picking up a AuNP with a Pt/It tip. In the appendix (see section A), we included a Q&A section on gold nanoparticles. For the initial experiments, we used gold nanoparticles from Sigma Aldrich (742007). After conducting a series of drop-cast experiments with those particles, we decided to purchase a more concentrated solution from Nanopartz (see Figure 31) [56]. Nanopartz also provided datasheets for the ordered particles, including the accurate spherical gold nanoparticles A11-50-CIT-DIH-1-10 (see Figure 76) and the concentrated accurate spherical gold nanoparticles AC11-50-CIT-DIH-100-1 (see Figure 75). We also ordered hollow spheres (see Figure 74). However, due to time constraints and expectations that the experimental setup was not adequate to detect reproducible differences compared to solid spheres, we limited our work on the regular AuNP and leave the hollow spheres for future studies.



**Figure 31:** Left: "Accurate Spherical Gold Nanoparticles" - 50 nm, Capping Agent Citrate, Buffer DIH, OD 1, 10mL, Right: "Accurate Concentrated Spherical Gold Nanoparticles" - 50 nm, Capping Agent Citrate, Buffer DIH, OD 100, 1 mL

### 2.2 Highly Oriented Pyrolytic Graphite (HOPG)

To pick up the AuNPs for tip functionalization we needed a conducting material suitable for STM that does not interact strongly with the AuNPs. The surface of HOPG is known for its inert nature, and it has a very weak interaction with the metal particles. We aimed to utilize this property to lift the particles with the STM tip. However, using HOPG has a drawback in that it does not allow reliable STM and AFM imaging of the nanoparticles due to the easy tip-induced

movements of the particles [57]. For the experiments, we used HOPG ZYA (Mos.Spr.  $0.4(1)^\circ$ , size  $10 \times 10 \times 1 \text{ mm}^3$ ) and HOPG ZYH (Mos.Spr.  $3.5(15)^\circ$ , size  $10 \times 10 \times 1 \text{ mm}^3$ ). ZYA and ZYH identify the quality of the surface, with ZYA marking the highest quality, which can be used to calibrate the x-/y- and z- distances of the system.

### **2.3 Gold crystal**

We used an unprepared gold single crystal, presumably Au(111), that came with the STM. In Figure 40 we see a picture of the crystal on the sampleholder.

## 3 Application of AuNP on HOPG

### 3.1 Dropcasting Method

To perform STM luminescence measurements we need a plasmonic tip as well as an optical setup to detect photons. To functionalize the tip we will pick up gold nanoparticles (AuNPs) from HOPG. We planned to deposit AuNPs to HOPG using two methods: dropcasting and with an electro spray. For the dropcast experiments, after applying the first drops of AuNPs onto HOPG and observing their circular staining patterns as they dried, we inserted the samples into the AFM for further investigations.

#### 3.1.1 Setup

We used a Pipetman P20 from Gilson and corresponding tips. To observe the particles, we used the light microscope BX41M and the AFM NX10 from Park System. When using the BF mode of the BX41M, the light hits the sample at an angle and not directly from above. In the Appendix B.8 we have the scaling of all the uncropped fotos made with the BX41M.

The oven we used to heat and dry the samples was a TR 240 LS from Nabertherm (see Figure 32).



*Figure 32: TR 240 LS oven we used for the drying experiments.*

#### 3.1.2 Methods and Results

After applying the first microliter of AuNP solution using Pipetman P20 from Gilson onto HOPG we made the following observations using the Atomic force microscope (AFM), documented in section C.2, with the help of Simon Jöhr: (1) the particles arranged themselves in a layer rather than piles, (2) the distribution of particles was uneven, with clusters in cracks of the HOPG and at the circumference of the drop (we realized that the clusters of particles were mostly big enough for us to observe in the optical microscope), (3) we do not have enough particle density to perform STM measurements which have a scan range of  $1\ \mu\text{m}$  requiring at least 10 to 100 particles in that range, and (4) there was a lot of water on the surface that we needed to remove (see Figure 85).

**3.1.2.1 Increase concentration** From our AFM measurements we concluded that we do not have enough particle density to perform STM measurements. The scan range of our STM

is with  $1 \times 1 \mu\text{m}^2$  smaller than the scan range in the AFM ( $10 \times 10 \mu\text{m}^2$ ). To successfully detect particles, the scan range of the STM should have at least 10 to 100 particles.

To increase the density of the particles, we tried the following approaches:

- We applied several drops in different ways and observed that the second one destroyed the boundary of the first one. It did not matter if the first drop dried before we applied the second one or if it was still wet. The second drop did not maintain a circular form and ran over the edge of the HOPG. Additionally, the second drop caused all the particles from the first one to be washed onto the sample holder.
- We applied several drops within a limited area and used silver glue to draw circles to contain the drops. While the walls of the silver glue held the drops, the particles were drawn into the silver glue. We documented our results in figures 91, 92, and 93.
- We heated the sample and applied particles on HOPG we heated in the oven. The particles were splattering around in an uncontrolled manner and with too big distances in between, making them not applicable for STM. See Figure 87, 88, 89, and 90.
- We heated the whole liquid to increase the optical density. After evaporating the solution, the AuNPs clumped together and lost their purpose for tip functionalization. For the drying process, we chose  $110^\circ\text{C}$  so that only water evaporates, but the citric acid in the buffer does not crystallize. We put the liquid in the oven and documented the steps in table 8.

Since all of our ideas did change the AuNP properties or changed their distribution in an uncontrolled manner, we decided to buy denser particles.

The particle distribution from the ordered Nanopartz particles appeared suitable for our investigations (see Figure 75). According to an employee, they dropcast on a TEM grid. We started looking for TEM grids with the intention to insert them into the STM. Under *et al.* used TEM grids for STM [58]. They used a 2000 grid covered by graphene. The squares were about  $7.5 \mu\text{m}$ . We ordered some gold grids (CF400-AU-ET, carbon square mesh, 400 mesh). Additionally the microscopy center lent us some Nickel 400 mesh grids. Dropcasting on the grid was difficult since the carbon layer ripped apart, and also the scanning on the big steps was challenging. We crashed the tip too much and went back to dropcasting on HOPG.

## 3.2 Electro spray

To perform STM luminescence measurements we need a plasmonic tip as well as an optical setup to detect photons. To functionalize the tip we will pick up gold nanoparticles (AuNPs) from HOPG. We planned to deposit AuNPs to HOPG using two methods: dropcasting and with an electro spray. However, building up the electro spray was more involved than anticipated, so we focused mainly on the dropcast technique.

### 3.2.1 Setup

We used the electro spray UHV4i from Molecularspray Ltd, which is a modular electro spray deposition source [59]. To understand the system, we collected schematic drawings (see Figure 33).

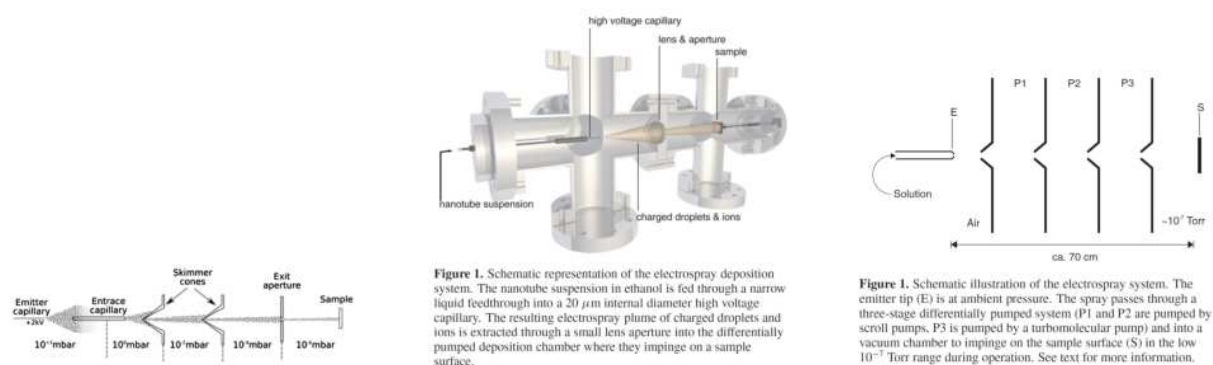


*Figure 33: Schematic drawing from the papers [60–62].*

We used a 10 mL syringe of SGE model 10 MDR-LL-GT. In Figure 34, we see how we connected the syringe to the red capillary.

We tested this setup with ethanol and looked at how much pressure was needed to get a drop through the capillary (see Figure 35).

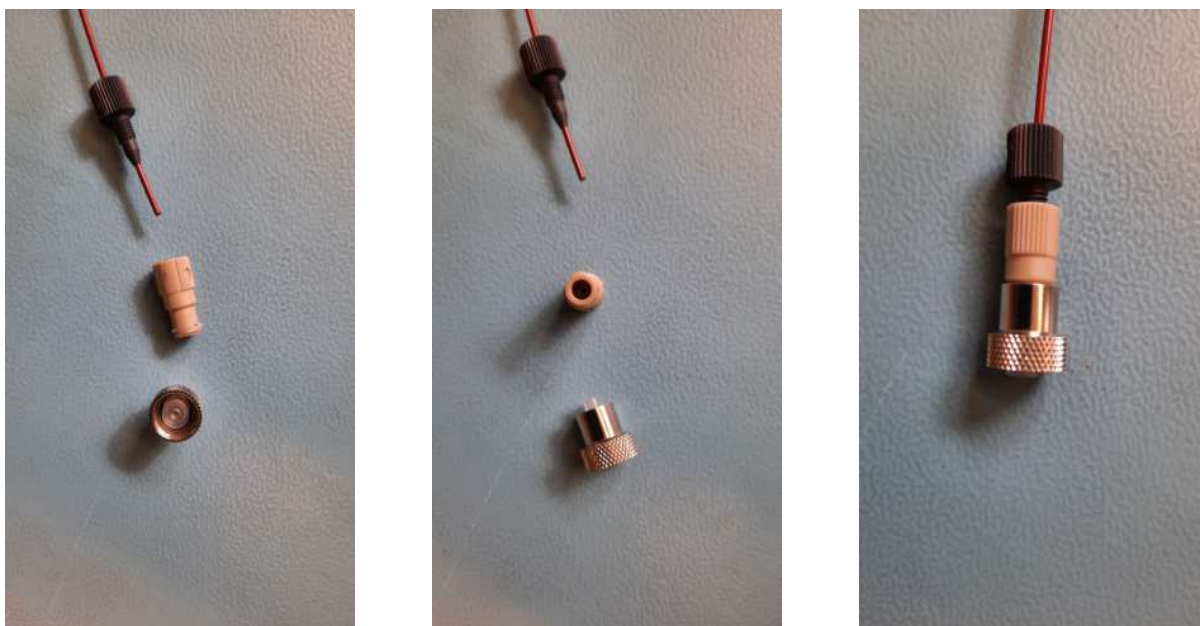


*Figure 34: Connection of capillary and syringe. Left and middle: Parts from above and from the side. We see the red capillary on top, the adapter in the middle and the syringe adapter on the bottom. Right: All the parts screwed together.*



*Figure 35: Testing of the syringe setup with ethanol. If we watch closely we see a drop leaving the capillary.*

On the other end of the capillary, we added the three-way tap with an emitter capillary. In Figure 36, we see the assembly.

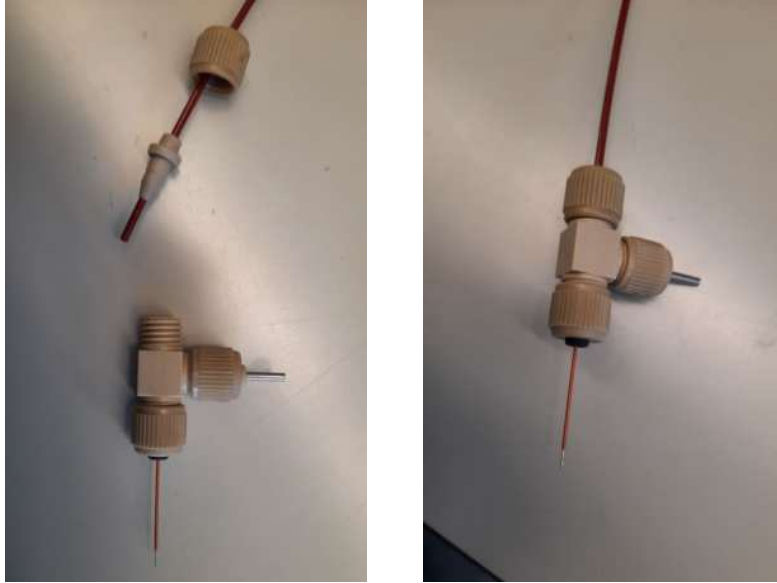


**Figure 36:** End of the red capillary connected to the manipulator with the three-way tap. On the bottom of the picture we see the emitter capillary with the metal tip.

To get the liquid out of the syringe, we want to use the syringe pump AL1000 ([manual](#)) from Wold precision instruments with the settings summarized in Table 2. It can be used to pump the volume properly with a constant flow.

Setting	Value
Diameter	14.5mm
Rate	88.0
Units	$\frac{ml}{h}$
Volume to be dispensed	50 $\mu$ l
Volume dispensed	300 $\mu$ l

**Table 2:** Settings of the AL1000 syringe pump.

We installed the 5-axis manipulator on the side of the aperture with the entrance flange as seen in Figure 37.



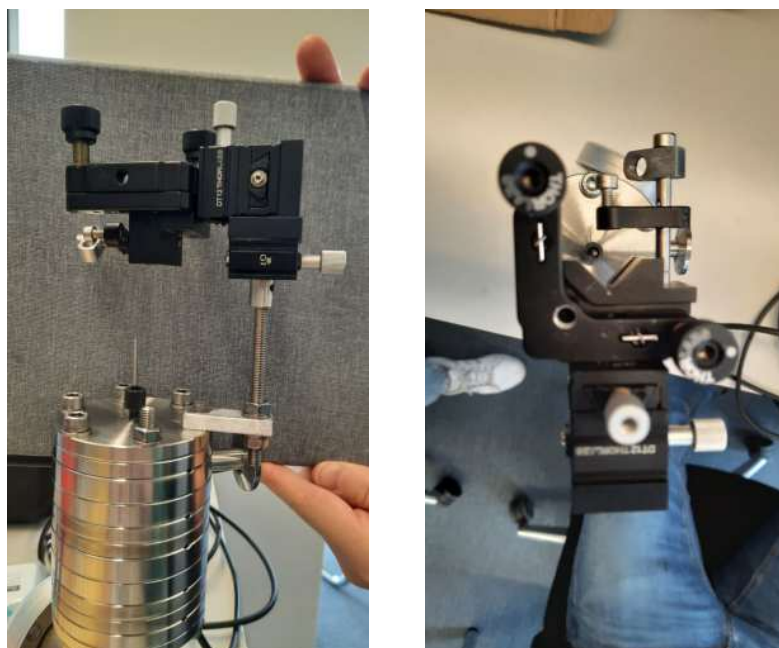


*Figure 37: On the left we see the setup from the side and on the right we see it from above with the focus on the entrance capillary (see schematic drawing in 33).*

In the Figure 38 we see the first alignment of the system. Through the microscope we took some pictures with the cellphone camera (see Figure 39).

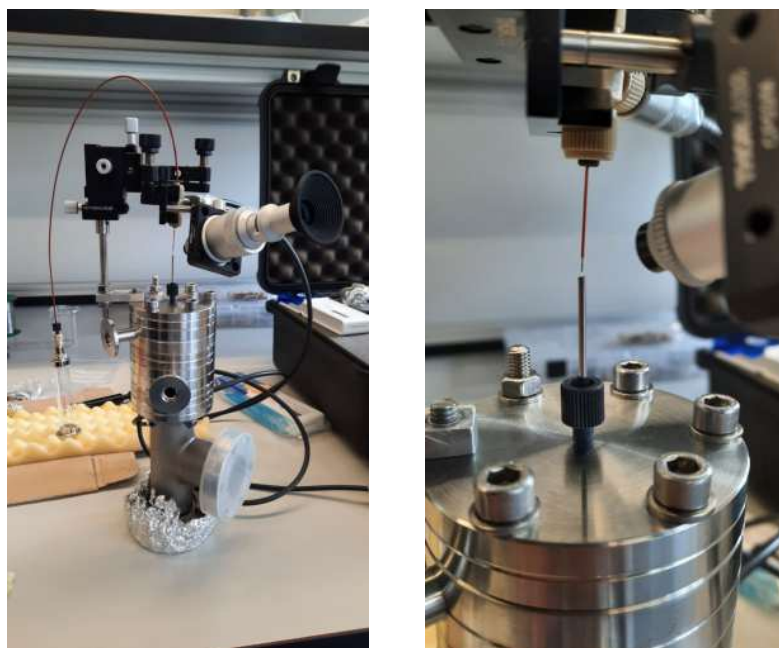


*Figure 38: Overview of the combined setups from above (left) and the approaching point of the emitter capillary connected to the syringe and the entrance capillary connected to the spray system (right).*

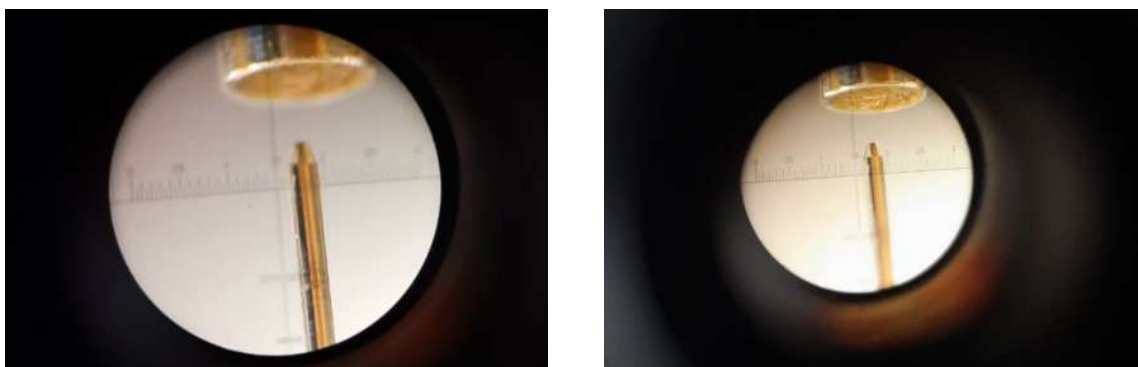


*Figure 39: The pin of the emitter capillary pointing to the entrance of the entrance capillary (metal surface above). Focus on the scale of the microscope (right).*

We started connecting the electro spray to the VTSPM (see Appendix B.3).

## 4 Optical setup to detect light

### 4.1 Setup

#### 4.1.1 Sample holder

We fixed the gold crystal on the sample holder by clamping it down with spot welded stripes of Tantalum foil  $3N+ 100 \times 200 \times 2 \text{ mm}^3$ .



*Figure 40: Sampleholder with gold crystal fixed with spot yielded Ta foil and AuNPs applied on HOPG fixed with silver glue.*

#### 4.1.2 Light sensitive camera stingray F-145

We used a stingray F-145 to detect light. In Figure 41 we see a plot of its quantum efficiency.

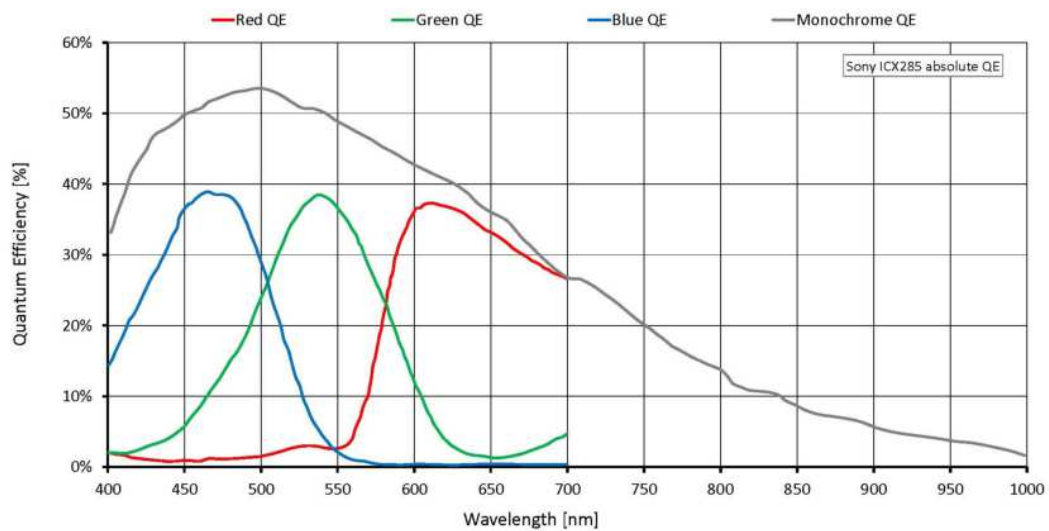


*Figure 41: Quantum efficiency Plot of Stingray F-145. [63]*

We tried to eliminate all the light sources in the room as good as possible with tape and alu foil and mounted the light sensitive camera on the VTSTM.

### 4.1.3 Fibres

*Table 3: List of used Thorlabs fibres.*

Fibre name	Group
LFM1F-1	Lensed Tip Fiber Patch Cable
M86L01	Ferrule Patch Cable
M141L02	Flat Cleave Patch Cable
M133L02	TECS Double-Clad, FC/PC-FC/PC Fiber Patch Cable

In Figure 42 we see the difference between lensed and flat fibre

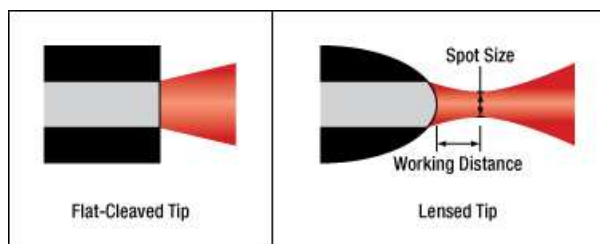


*Figure 42: Difference between flat and lensed fibres.[64]*

### 4.1.4 USB2000+UV-VIS-ES Fiber Optic Spectrometer

Dr. Matthias Hengsberger lent us a USB2000+ Fiber Optic Spectrometer. The USB2000+UV VIS-ES model is a spectrometer pre-configured for general UV and visible measurements. It covers a wavelength range from 200 to 850 nm. It was connected to a ocean optics 100  $\mu\text{m}$  UV/VIS EOS-A1246041 fibre. To fix the fibre tip in the STM head we constructed a wireloop in the shape of an eight between the two pillars of the sample stage to clamp the fibre in the head (see Figure 43 and 57).

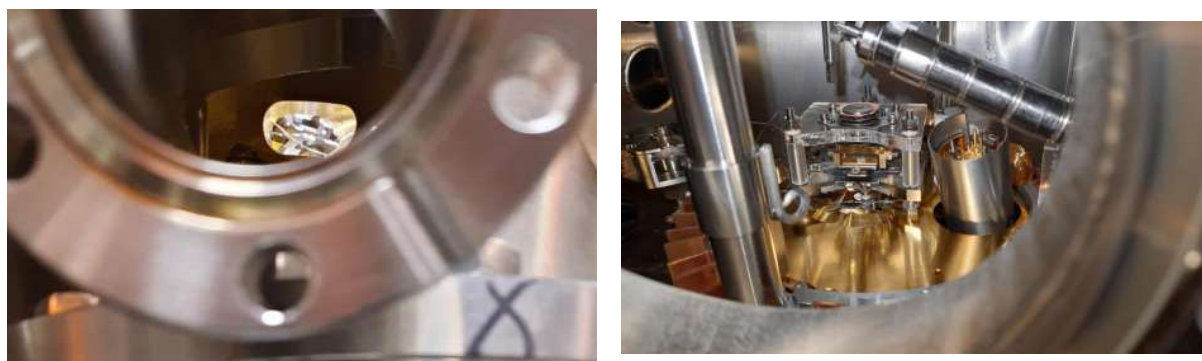


*Figure 43: Left: Looking on the wire construction from below. The fibre was entered through this flange pointing to the sample with a 30° angle. Right: Front view of the wire construction attached to the sample stage.*

### 4.1.5 Single Photon detector (SPD)

We were working with the photon counting detector modules (PDM) of micro photon devices. It reaches a photon detection efficiency of 49% at 550nm and generates a TTL output pulse

(Transistor-transistor logic (TTL), which is a digital logic design) per detected photon. For the first measurements we inserted the M86L01 Ferrule Patch Cable from thorlabs (see table 3) with the same wire construction we already used for the Spectrometer (see section 4.1.4). The second fibre we inserted, LFM1F-1, took more patience to install because it has a fragile and thin tip. Additionally to the wire construction we used scotch tape to fix this fibre in the head. In Figure 44 we see how the fibre tip was aligned with the STM junction.



**Figure 44:** Alignment of the fibre LFM1F-1. We see the gold crystal, the tip in the middle and its reflection in the sample. The bright line coming from the bottom left pointing to the tip is the fibre tip.

#### 4.1.6 Optical Setup

We wanted to build an optical setup using the same basic components as described in the review paper of Rossel *et al.* [16]. In the theory section 7.3.1 we described alternatives to setup we used.

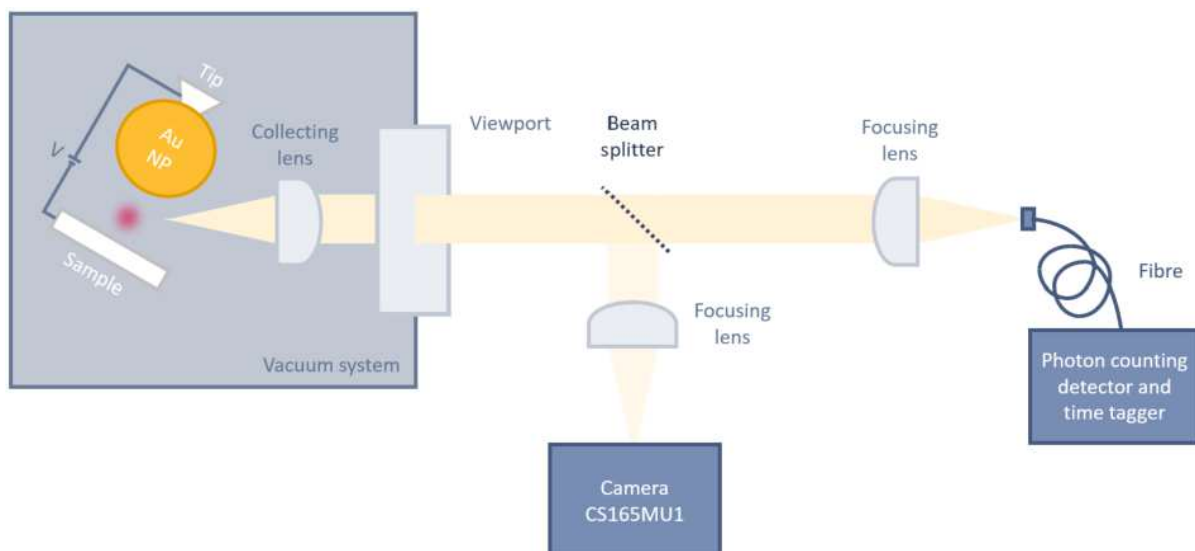


**Figure 45:** Schematic drawing of the optical setup (described in the text below).

In the vacuum chamber, the light emitted from the tunneling junction is collimated by a collect-

ing lens (Thorlabs 355397). The now parallel beam is lead through the fused silica viewport (UV grade) to a beam splitter (Thorlabs BS025) outside the vacuum chamber. The main portion (90%) of the beam is focused and coupled into an optical fibre (Thorlabs M133L02). This fibre leads to the single photon detector (SPD, see section 4.1.5). In Figure 46 we see how we attached the SPD to the system. The remaining portion (10%) of the beam was used for imaging with the Thorlabs camera (Thorlabs CS165MU1).

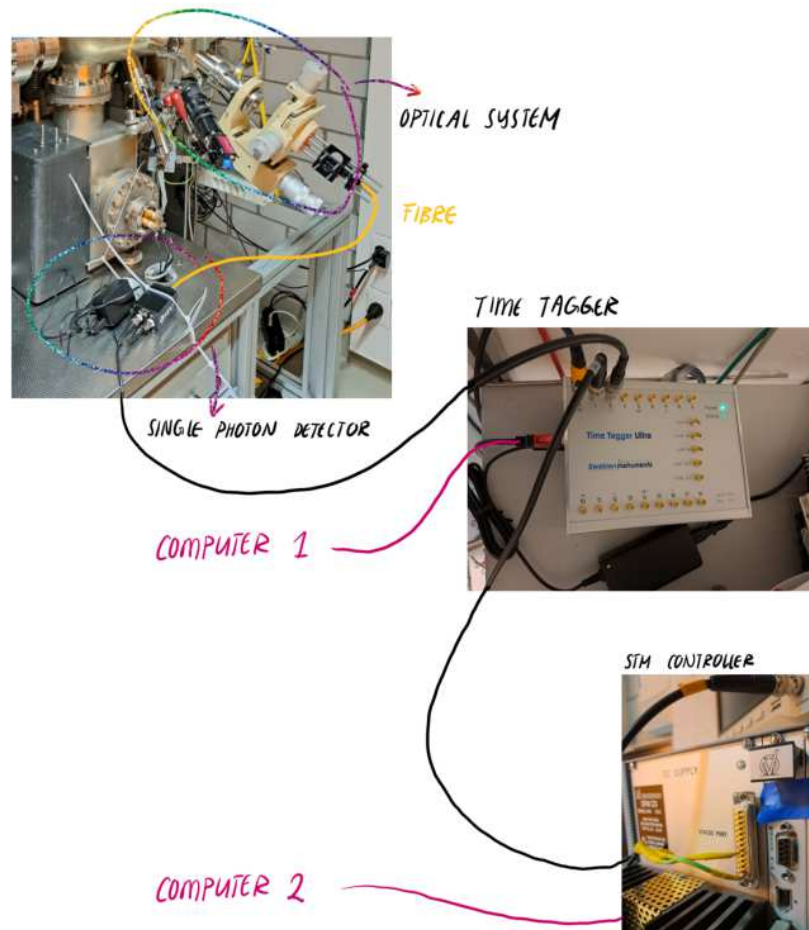


**Figure 46:** Connection of the single photon detector (SPD) with the time tagger and the STM controller. With the optical system we collected the light coming from the STM junction. The fibre collecting the photons was connected to the SPD, which in turn was connected to the Time Tagger Ultra from Swabian Instruments (see Figure 47). With scala pro on Computer 2 we controlled the speed and dimensions of the scan. The signal containing line and pixel information of the scan was wired from the status port of the STM controller (see Figure 48) to the time tagger. This allowed us to assign the digital signal of the collected photon counts to a pixel of a scanned line of the STM using a python script on Computer 1.

In the event that one wishes to replicate the experimental setup, descriptions and pictures of all utilized components are provided in the Figure 4.1.6.

For the first experiments we used the fused silica viewport with UV grade. The viewport can cause reflections which were disruptive when we aligned the fibre. Since we performed our measurements in air and not in UHV we temporarily removed the viewport.





**Figure 47:** The timetagger of Swabian instruments. Output 2 was connected to the Photon counter and Output 3 was connected to the STM controller trigger port (see Figure 48).



**Figure 48:** Trigger port of the STM control electronics that we connected to the time-tagger. The scan produces a line trigger for every scan line, enabling us to produce a spatially dependent photon map. To connect the pins we used the information provided in the SCALA pro manual (see Figures 72 and 73).

**4.1.6.1 Lens holder** We needed to fix the collimating lens in the vicinity of the junction in the vacuum chamber. After some tries with a tube which holds the lens at one end (see Figure 78) Ales designed and 3D printed a lens holder that was directly attachable on the sample holder (see Figures 49 and 50). As marked in the Figure 49 we chose an angle of  $30^\circ$  since the light emission is the strongest there (see section 7.3.1).

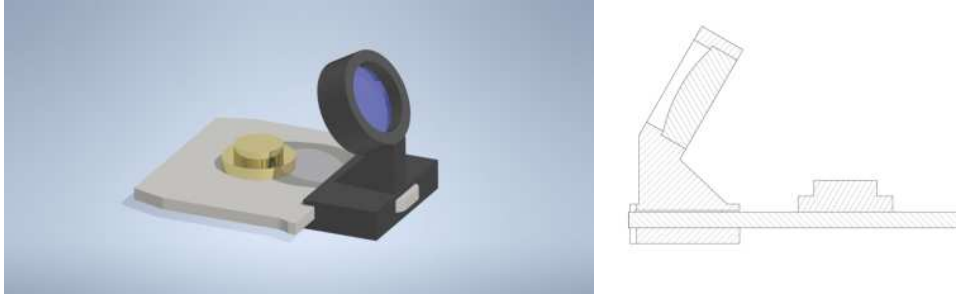


**Figure 49:** *Lensholder made by Ales to fix the collimating lens in the vicinity of the junction in the vacuum chamber.*

Since the lens holder geometry was designed for a gold crystal, the focal point of the lens is at 1 mm above the sample plate, which is why we had to add a platform for thinner samples. We realized the platform by spot welding seven layers of Tantalum foil on top of each other onto the sample holder. On the last foil we glued the HOPG with silver glue (see Figure 50).



**Figure 50:** *Photo of the lens holder added to a sample holder.*

**4.1.6.2 Thorlabs camera** To install and adjust the fiber we used the images of the Thorlabs CS165MU1 1.6 MP Monochrome CMOS Camera. With the beamsplitter we were able to see the tip through the collimating lens in the lens holder (see Figure 51 on the right).



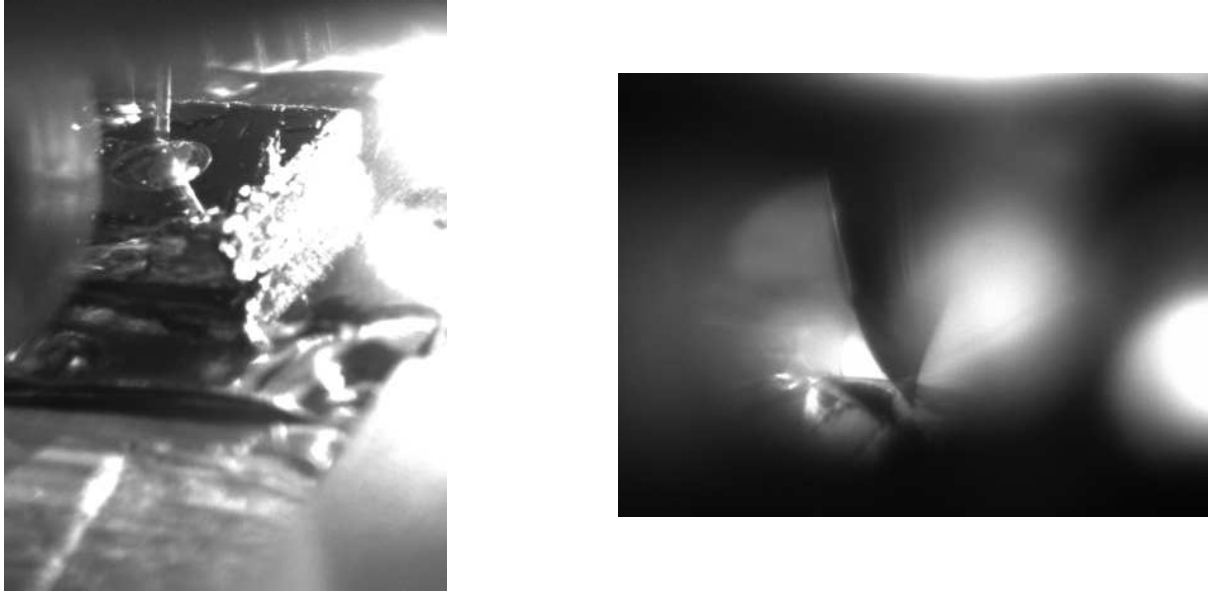


**Figure 51:** *Left: Picture from the stingray F-145 camera pointing to the sample. Right: Corresponding view on sample with Thorlabs camera through the collimating lens in the vacuum system. The dark gray background below is from the drop. Where the surrounding of the tip changes to a lighter gray is the edge from drop to HOPG. We see the tip and diffuse reflection of the tip.*

**4.1.6.3 Bandpass filters** Since the USB2000+ spectrometer was not sensible enough for our setup we tried to narrow down the wavelengths of the emitted light from the junction with the Bandpass filters listed in table 4 we borrowed from Dr. Mirco Ackermann.

**Table 4:** *Bandpass filters we used to narrow down the wavelengths of the emitted light from the junction.*

Wavelength [nm]	width [nm]	brand
610	10	Newport
600	10	Newport
580	10	Newport
570	10	Newport
550	10	Newport
520	15	BrightLine
480	20	ET Chroma

## 4.2 Experiments and methods

### 4.2.1 Light sensitive Stingray F-145 camera

To detect the photons coming from the junction between tip and the gold crystal we performed the following steps:

(1) we mount the Stingray F-145 camera on the STM and start vimba viewer [65] on the computer connected to the camera, (2) we functionalize the tip by forcefully indenting it in the gold crystal by approaching the crystal with the remote control, (3) we position the functionalized tip at another position above the crystal and save the picture on vimba viewer, (4) we shut down the

lights and make it as dark as possible, (5) we start scanning. The settings for the scanning condition are noted next to the corresponding camera photo, (6) we save ten photos in vimba viewer, each illuminated for 60 s. The settings of vimba viewer are noted next to the pictures, (7) Stack the ten photos in ImageJ [66]. The editing steps of the photos that result in the pictures presented in the result section are documented in the appendix C.3.1.

To measure on the AuNPs we performed similar steps with one crucial difference: (3) we position the functionalized tip on the sample with HOPG (once over HOPG itself and once over the dropcasted drop) and save the picture on vimba viewer. To do so we prepared a sample with both, gold crystal and HOPG (see Figure 40).

## 4.2.2 Filters

In the absence of a sensible enough spectrometer, we attempted to determine the wavelength of the light emitted from the junction by utilizing bandpass filters listed in Table 4. These filters were fixed in the light path after the beamsplitter but before to the lens that focuses the light back onto the fiber. We used the Thorlabs camera to ascertain if the junction was indeed emitting light. With each filter inserted, we positioned the tip above the sample while applying a bias voltage of  $-3.8\text{ V}$  and a current of  $50\text{ nA}$ . We identified positions where the junction emits light in the Thorlabs camera. However, none of the filters allowed us to detect any photons using the single photon counter, thus leading us to conclude that our experimental setup was not suitable for narrowing down the wavelength of the emitted light.

## 4.2.3 USB2000+ Spectrometer

We fixed the tip of the fibre as described in the section 4.1.4. We always checked on the light sensitive camera stingray F-145 if light is emitted from the junction. For every measurement we were scanning with a bias voltage of  $3.5\text{ V}$ . We recorded a dark spectrum while scanning with  $1\text{ nA}$ . Then we recorded a spectrum while scanning with  $1\text{ nA}$ . I did not record the STM pictures for those measurements.

## 4.3 Results

### 4.3.1 Light sensitive Stingray F-145 camera

**4.3.1.1 Measurements on a gold crystal** We were interested in the light emitted from the junction of the functionalized tip (indenting in gold crystal) and the gold crystal. In Figure 113 we saw that the light intensity recorded with the camera after scanning with  $30\text{ nA}$  seems weaker than the one for the  $40\text{ nA}$  and the  $50\text{ nA}$  scans. We checked if a positive or a negative bias voltage makes a difference in Figure 114. It seems that the one for the negative bias voltage is brighter. We think that this comes from the fact that our experiments are not reproducible yet or that there is an calibration mismatch since the direction of the voltage should not have an influence on the light emission [2]. In the end we continuously changed the voltage but kept the current at  $50\text{ nA}$  (see figure115). We see that the light emission started between  $-2.5\text{ V}$  and  $-3.5\text{ V}$ . We missed to record  $-3.0\text{ V}$ . Around  $-5\text{ V}$  the intensity started to weaken. Between  $-5.5\text{ V}$  and  $-6.5\text{ V}$  we measured a high intensity.

**4.3.1.1.1 Light we see above 5 eV** In the paper of 2015 by Martínez-Blanco [67] they looked at light emission from Ag(111) driven by inelastic tunneling in the field emission regime. They describe, that above the vacuum level, scanning tunneling spectroscopy shows a series of well defined resonances associated with the image states of the surface, which are Stark shifted

due to the electric field provided by the STM tip (meaning their energy is higher compared to their energy in the absence of the electric field). While both image states (modification of the electronic structure near the surface due to the presence of the electric field, ) and plasmonic modes (collective oscillation of electrons in the material, from 2 V up to 4 V in Figure 52b)) involve electronic excitations in a material, they are different phenomena with distinct energy level structures.

If we look at Figure 52, as the bias voltage approaches 4.3 V, the tunnel junction enters in resonance with the first field emission resonance and the STM feedback loop has to increase drastically the tip-surface distance to keep the tunneling current constant. Eventually, this distance becomes large enough to weaken the tip-surface electromagnetic coupling and plasmons are no longer generated, for which light emission is quenched. Already the first field emission resonance (FER, marked with the number 1) is about 20 times less intense than the plasmonic intensity detected in the tunneling regime, and gets successively smaller for the next FERs.

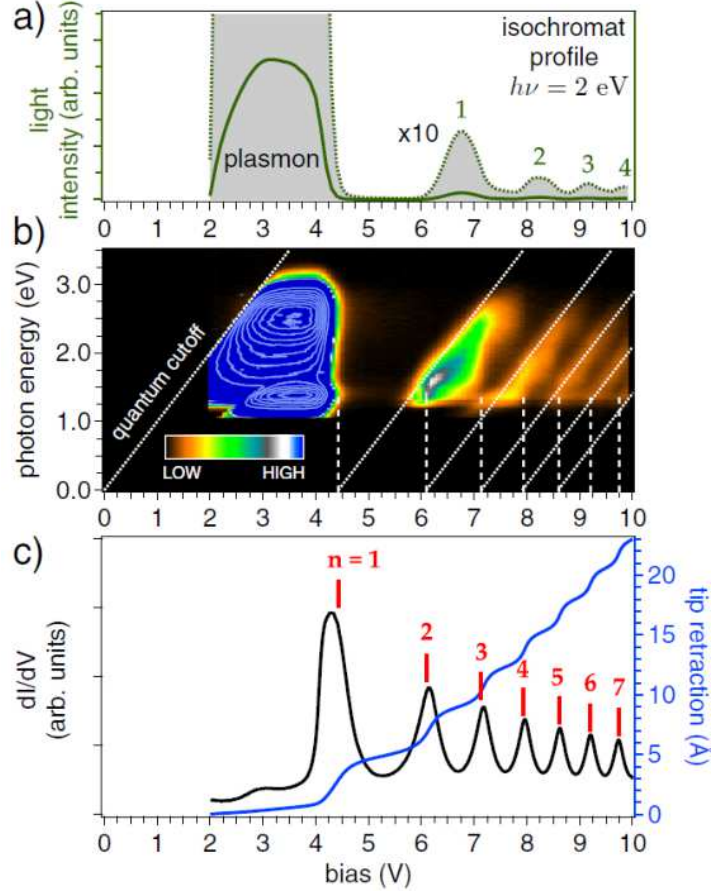


**Figure 52:** a) Profile of the light intensity map shown in b) along the isochromat line corresponding to  $h\nu = 2$  eV for bias voltages between 2 V and 10 V. The dotted line represents the same profile scaled by a factor of 10 for better visualization. b) Light intensity map as a function of bias and photon energy, measured at constant current (200 nA). Dotted white lines mark the quantum cutoff and the corresponding shifted cutoffs due to inelastic scattering into the different field emission resonances. The resonance energies are marked with vertical dashed lines. c) Black: differential conductance as a function of the bias voltage at constant current (200 nA). Blue: tip retraction with respect to the initial tip-sample distance, acquired simultaneously. The vertical red lines indicate the simulated energies of the first seven resonances according to a QM model (see paper for details) [67].

**4.3.1.2 Measurements on gold nanoparticles (AuNPs) dropcasted on HOPG** We were interested in the light emitted from the junction of the functionalized tip (indenting in gold crystal) and the HOPG sample with dropcasted AuNP solution. Figure 53 shows the light from the junction between the functionalized tip and HOPG (next to the dropcasted AuNP solution). We do not see a spot of higher intensity. The theory agrees with this result since HOPG does not have a strong enough plasmonic activity to emit light from the tunneling junction. Figure 54 shows the light from the junction between the functionalized tip and AuNPs on HOPG. We saw light at positive and negative bias voltages which corresponds to the literature and theory described in Reference [2].

### 4.3.2 USB2000+ Spectrometer

Even though we saw light with the camera stingray F-145, we were not able to detect it with the USB2000+ Spectrometer. In Figure 55 we see on the top the spectrum we recorded when we measured with the scanning conditions of  $-3.5\text{ V}$  and  $1\text{ nA}$  and saved it as a dark spectrum since we did not expect light coming from the junction under these conditions with our setup. But we see some sharp peaks around  $400\text{ nm}$ ,  $750\text{ nm}$  and  $1000\text{ nm}$ . Those peaks do not represent the light emitted from the junction. We think that they are artefacts since they also appear in all the other measurements. In the middle we recorded another spectrum with the scanning conditions of  $-3.5\text{ V}$  and  $50\text{ nA}$ . To compare the results we subtracted the dark spectrum from the spectrum in the middle and plotted it below in grey. We expect a resonance like in Figure 17. The rainbow colored lines in the last plot mark roughly the visible light spectrum. Since we were not able to see the expected resonance from the emitted light after crushing the tip (and my soul) 27 times and rearranging the fibre 12 times we conclude that the spectrometer is not sensitive enough to detect the low photon counts from our setup.

**Figure 53:** No light coming from the junction between the functionalized tip and HOPG (next to the dropcasted AuNP solution). Settings of the scan and in vimba viewer are summarized on the left of the according pictures. Bright corner on the top left is a light source in the room we were not able to eliminate.

**ON HOPG**

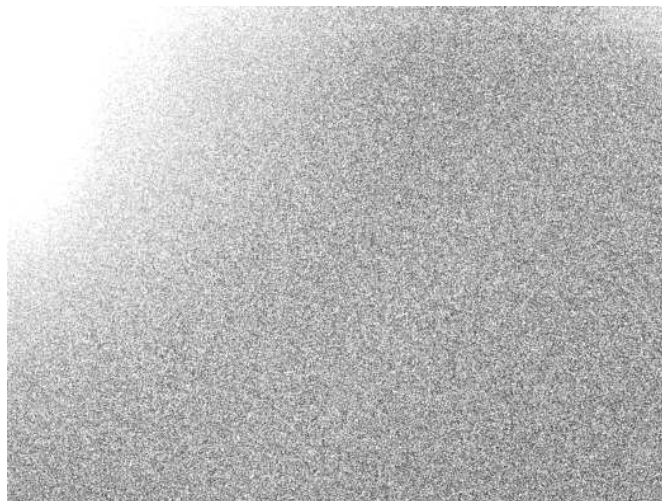
**Settings**

-3.5 V, 50 nA

Exposure: 60 s

Gain: 5 db, ATI: 50

Min: 0, Max: 3



(1)

**ON HOPG**

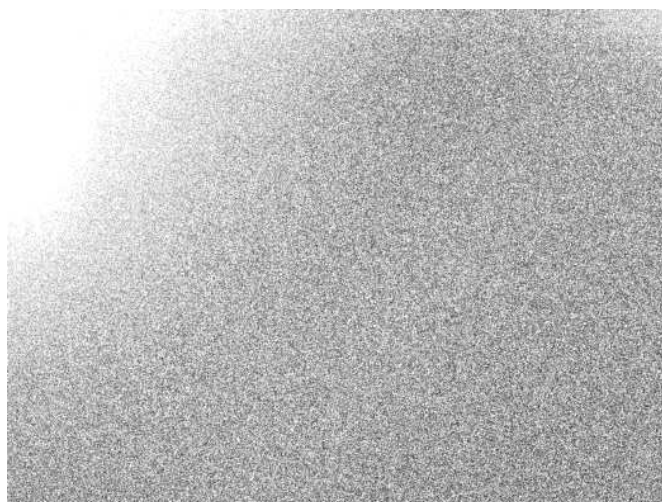
**Settings**

+3.5 V, 50 nA

Exposure: 60 s

Gain: 5 db, ATI: 50

Min: 0, Max: 3



(2)

*Figure 54: The bright spots in the middle correspond to the light coming from the junction between the functionalized tip and AuNPs on HOPG. Settings of the scan and in vimba viewer are summarized on the left of the according pictures. Bright corner on the top left is a light source in the room we were not able to eliminate.*

**ON Nanospheres**

**Settings**

-3.5 V, 50 nA

Exposure: 60 s

Gain: 5 db, ATI: 50

Min: 0, Max: 3



(1)

**ON Nanospheres**

**Settings**

+3.5 V, 50 nA

Exposure: 60 s

Gain: 5 db, ATI: 50

Min: 0, Max: 3



(2)

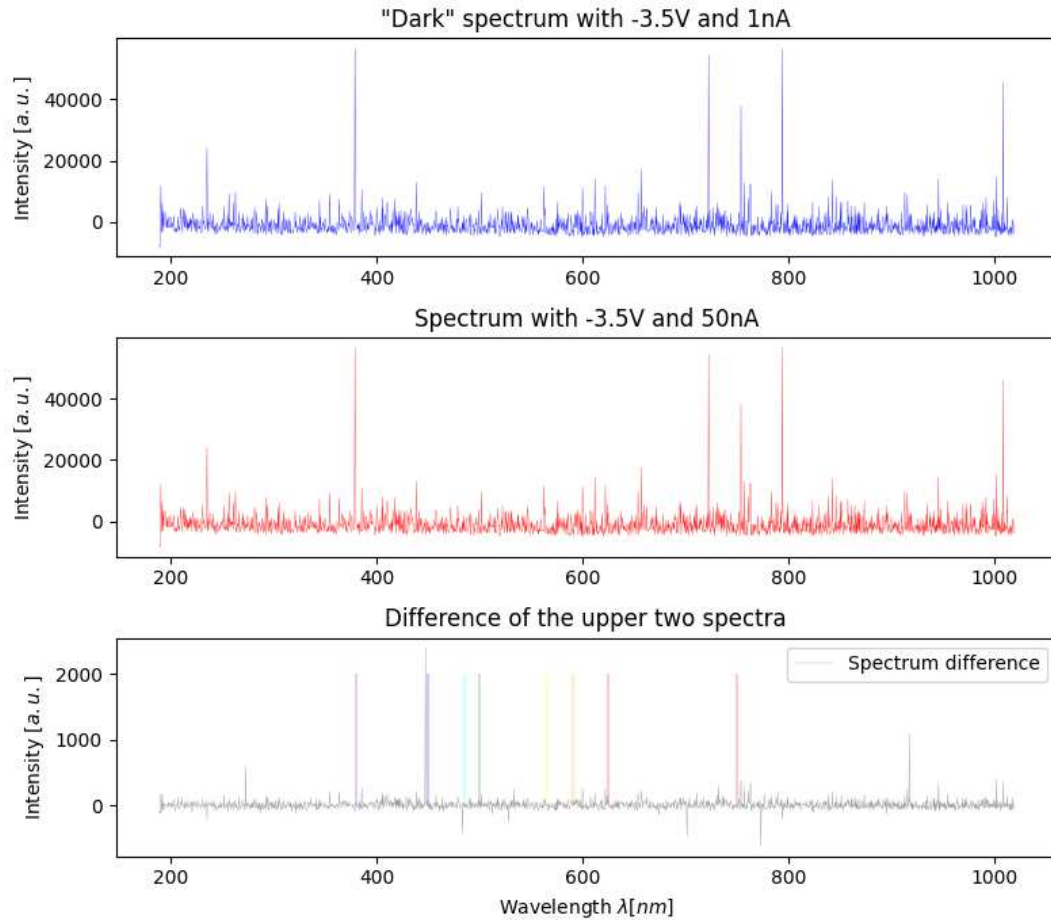


**Figure 55:** Spectras recorded with the USB200+ spectrometer. Top: Spectrum we recorded when we measured with the scanning conditions of  $-3.5\text{ V}$  and  $1\text{ nA}$ . We called it dark spectrum since we did not expect light coming from the junction under these conditions with our setup. We see some sharp peaks around  $400\text{ nm}$ ,  $750\text{ nm}$  and  $1000\text{ nm}$ . Those peaks do not represent the light emitted from the junction. We think that they are artefacts since they also appear in all the other measurements. Middle: Spectrum from the scanning conditions of  $-3.5\text{ V}$  and  $50\text{ nA}$ . Bottom: Comparison of the results by subtracting the dark spectrum from the spectrum in the middle. The rainbow colored lines mark roughly the visible light spectrum. Since we were not able to see the expected resonance from the emitted light we concluded that the spectrometer is not sensitive enough to detect the low photon counts.



## 5 VTSTM

### 5.1 Setup

We got a (1993) Variable temperature STM (see Figure 56) from Omicron by courtesy of Prof. Dr. Karl-Heinz Ernst at EMPA.

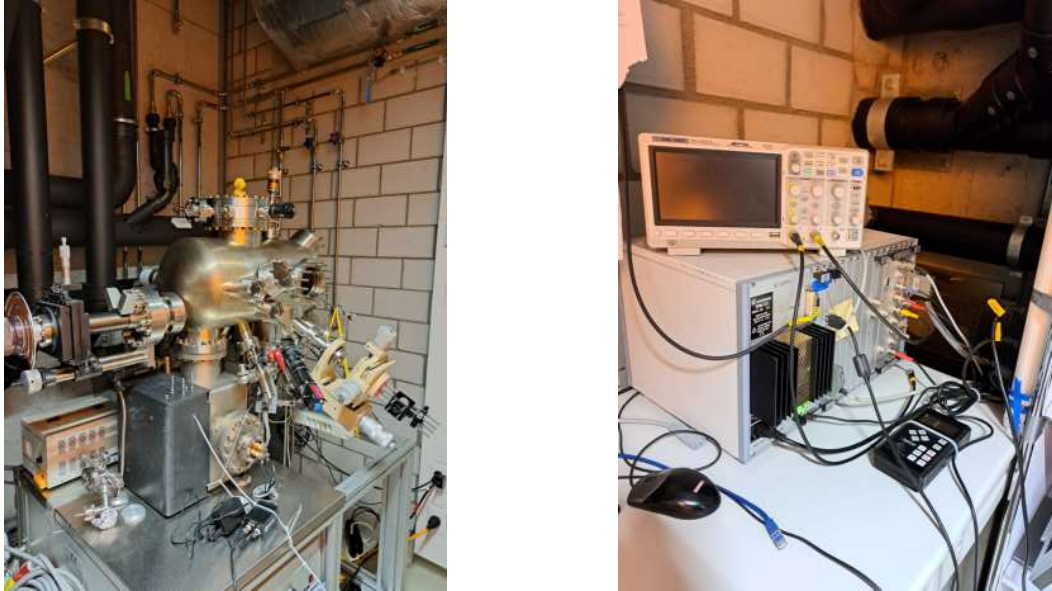


*Figure 56:* Left: The STM we used. On the microscope we see Lumi my dinosaur. The big xyz stage attached to the system is a part of the optical setup described later. We also see the light sensitive Stingray camera next to it (black with red sticker on top). Right: Controller. Since it was not possible to monitor the current in hovering mode (not scanning) we connected an oscilloscope.

From the manual we imported the pages from Figure 57. They will be useful to explain the fibre installation.

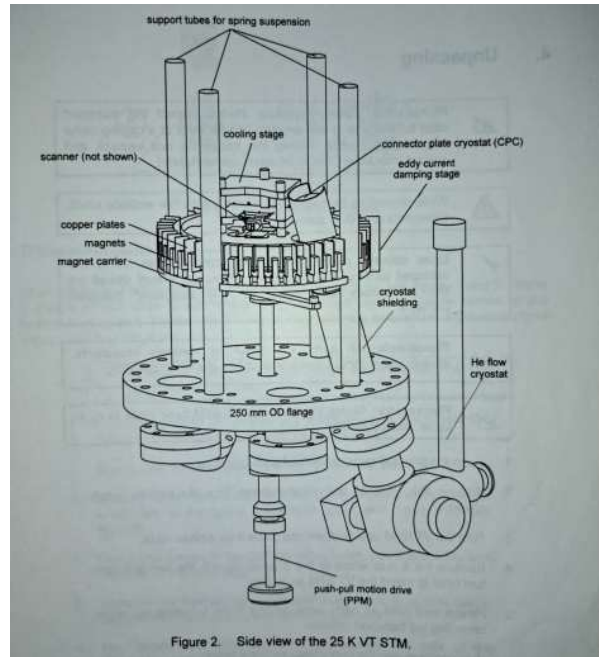
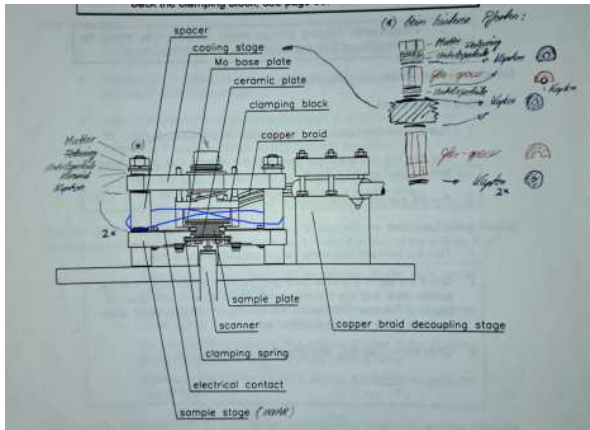


**Figure 57:** Pages from the manual. Left: Sample stage. The blue loop represents the wire installed to fix the fibres, Right: STM head.

The controller was connected to a computer with the operating system microsoft windows NT. On the computer we used the software SCALA pro.

### 5.1.1 Calibration with HOPG

I learned how to use VTSTM. Since the displacement of the scanner piezo in the x,y and z directions does not have a one-to-one correspondence with the applied voltage we calibrated the x, y and z channels of the scanner piezo using a sample of highly oriented pyrolytic graphite (HOPG) in a vacuum of  $\approx 10^{-7}$  bar. For the x and y directions we used atomically resolved images to get the distance between adjacent atoms and for the z direction we used the height of an atomic step. We compared it with literature values from Figure 58 [68]. We took 335 pm for the z channel and 246 pm for xy. The measurements and the performed steps are documented in the appendix B.7.

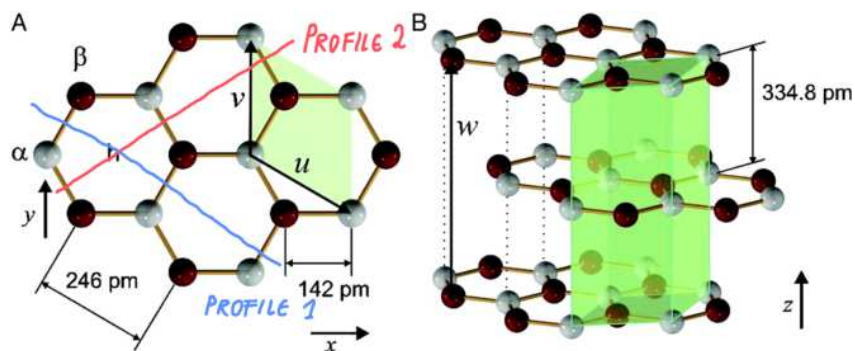


**Figure 58:** Pictures of the atomic arrangement of HOPG [68]. The blue and the red profile correspond to the profiles in Figure 80.

For the xy calibration we found the conversion factor

$$\frac{222 \text{ pm}}{246 \text{ pm}} = \mathbf{0.9} \quad (5.1)$$

and for the z calibration we found

$$\frac{557 \text{ pm}}{335 \text{ pm}} = \mathbf{1.66} \quad (5.2)$$

Both factors are from "measured" to "real".

## 5.2 Goldcrystal

### 5.2.1 Experiments and methods

**5.2.1.1 Poking crystal** With the intention to pick up gold particles from the HOPG we learned how to use the "Nanostructuring" function of the STM. We scanned the gold crystal, poked the crystal with different voltages, currents and hight settings and afterwards scanned the crystal again to get a feeling of poking in gold. We were scanning a frame of  $10 \times 10 \times 1 \text{ mm}^3$  with 120 to 120 pixel,  $3012 \text{ nm s}^{-1}$ , 1 nA, loopgain of 15% and  $-1 \text{ V}$  in the up-down scan mode on SCALA pro. Then we were poking with the macro we implemented in Scala pro > Nanostructuring > Mode: Single Event, Eventline: Macro below. We imported the nanostructuring language from the SCALA pro manual in the appendix in Figure 72 and 73.

#### Macro: Poking the crystal

```

; Voltage pulse ; Approach tip towards Sample
feedback, 0 ; Feedback loop off
set_v, 0 ; Gap voltage = 0mV
set_z, -30.0 ; Approach tip 15 nm towards the sample
delay, 1000000 ; 1000000 ms delay
set_z, 30.0 ; Pull tip away
delay, 1000 ; 1000 ms delay
reset_z ; Return to regulated position
delay, 1000000 ; 1000000 ms delay
reset_v ; Return to original gap voltage
reset_feedback ; Feedbackloop on

```

**5.2.1.2 Fibre M133L02 pointing directly in the junction** We used the single photon detector to quantify the photons emitted from the junction. The fibres connected to the detector were pointing directly to the junction. The measurements we performed were under ambient pressure and at room temperature. After some tries we were finally able to detect the light with the light sensitive camera as well as photoncounts from the single photon detector.

**5.2.1.2.1 Heatmap** Using the SPD we wanted to generate heat maps to establish a relation between the applied bias voltage, the tunneling current and the detected photon counts. We connected the fibre M133L02 to the single photon detector and fixed it in the head as described in section 4.1.4. It is important to mention that the system was not connected like described in section 4.1.6 yet. We were scanning a frame of  $300 \text{ nm}$  to  $300 \text{ nm}$  with 10 to 10 pixel,  $300 \text{ nm s}^{-1}$ , loopgain of 15% in the up-down scan mode on SCALA pro. For every heat map pixel of Figure 61 we collected data from the SPD for one minute and assigned it later with a program we wrote on python.

**5.2.1.2.2 Spectroscopy** We wanted to optimize the heatmap from the section above. To do so we used the SCALA Pro software in spectroscopy mode. It is important to mention that the system was not connected like described in section 4.1.6 yet. In its setup we chose the voltage range from  $-1\text{ V}$  to  $-7\text{ V}$ . With the shortest delay time ( $20\text{ }\mu\text{s}$ ) as well as the longest acquisition time ( $163\,840\text{ }\mu\text{s}$ ) possible. The feedbackloop was on and we measured 3200 datapoints. We connected the fibre M133L02 to the single photon detector and fixed it as described in section 4.1.4. In the program of the photon counter we also made 3200 bins with a width  $163\,840\text{ }\mu\text{s}$ . At the same time we hit the start button in both programms. We ignored the delay from the spectroscopy because I measured 524s and all delay times together are 0.064s.

**5.2.1.2.3 Optical setup** To optimize our system we changed the setup. The fibre was not pointing directly to the junction anymore but we built a lens system leading the light beam coming from the junction out of the STM chamber and focussing it on the fibre as described in section 4.1.6. As a first experiment we verified our setup described in Figure 46 and checked if the system is connected correctly as well as if the heatmap python code (on Computer 1 of Figure 46) written by Berk Zengin is working. To do so we used the gold crystal as a sample and the tip was functionalized by indentation in the gold crystal. We scanned a  $400\text{ nm}$  to  $400\text{ nm}$  scanframe with  $-3.8\text{ V}$ ,  $50\text{ nA}$ , scanspeed of  $1600\text{ nm s}^{-1}$  and  $200\text{ px}$  to  $200\text{ px}$ . We also created a  $200\text{ px}$  to  $200\text{ px}$  heatmap with the pythoncode.

## 5.2.2 Results

**5.2.2.1 Poking crystal** With the intention to pick up gold particles form the HOPG we learned how to use the "Nanostructuring" function of the STM. We scanned the gold crystal, poked the crystal with different voltages, currents and hight settings and afterwards scanned the crystal again to get a feeling of poking in gold. In Figure 59 we see on the left the scan before the poking and on the right after the poking. In the middle of the right picture we see the indentation of the poke with a surrounding imprint of the tip. After some pokings we realized, that sometimes the scans before and after were not comparablea and that they showed an apparent lateral shift of the location. We explain this effect in Figure 60.

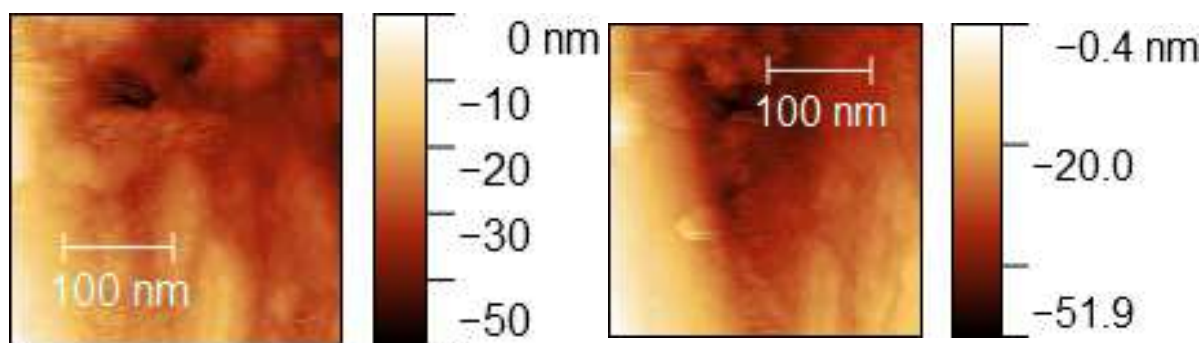


*Figure 59: Scans before (left) and after (right) the poking.*

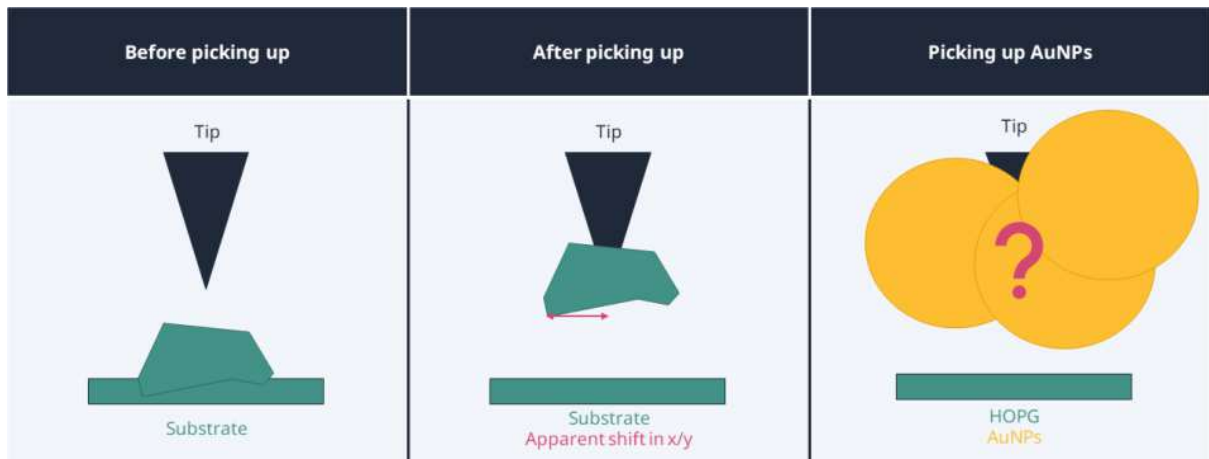


**Figure 60:** *Lifting up a particle in the STM can lead to completely different scans before and after. On the left we see that with lifting a particle the tip can relocate in x/y due to a new tip geometry. On the right we indicate that we do not know how we pick up gold particles.*

**5.2.2.2 Fibre M133L02 pointing directly in the junction** We used the single photon detector to quantify the photons emitted from the junction. The fibres connected to the detector were pointing directly to the junction. The measurements we performed were under ambient pressure and at room temperature. After some tries we were finally able to detect the light with the light sensitive camera as well as photoncounts from the single photon detector.

**5.2.2.2.1 Heatmap** Using the SPD we wanted to generate heat maps to establish a relation between the applied bias voltage, the tunneling current and the detected photon counts. With the collected data we made a current- bias voltage - photon countrate - heatmap (see Figure 61) to figure out where we have the highest photon-countrate. The resulting distribution confirms the theory that we need high enough bias voltage and currents to emit photons from the TIP plasmons. The dark count rate of the SPD is around 9 photon counts per second.

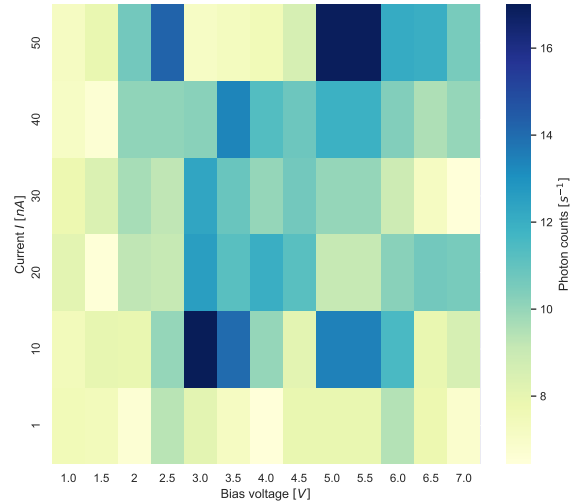


**Figure 61:** Current- bias voltage - photon countrate - heatmap. The plot helps us figuring out where we have the highest photon-countrate. The resulting distribution confirms the theory that we need high enough bias voltage and currents to emit photons from the TIP plasmons. The dark count rate of the SPD is around 9 photon counts per second.

**5.2.2.2.2 Spectroscopy** We wanted to optimize the heatmap from the section above. To do so we used the SCALA Pro software in spectroscopy mode. We performed the experiment several times and compared the data of two measurements in Figure 62. To see the distribution of the photon counts better we changed the scale of the plot to a lower maximum (see Figure 63). We noticed that the photon counts are not quite reproducible in the voltage/current space. This motivated us to use a different setup as described as described in section 4.1.6.

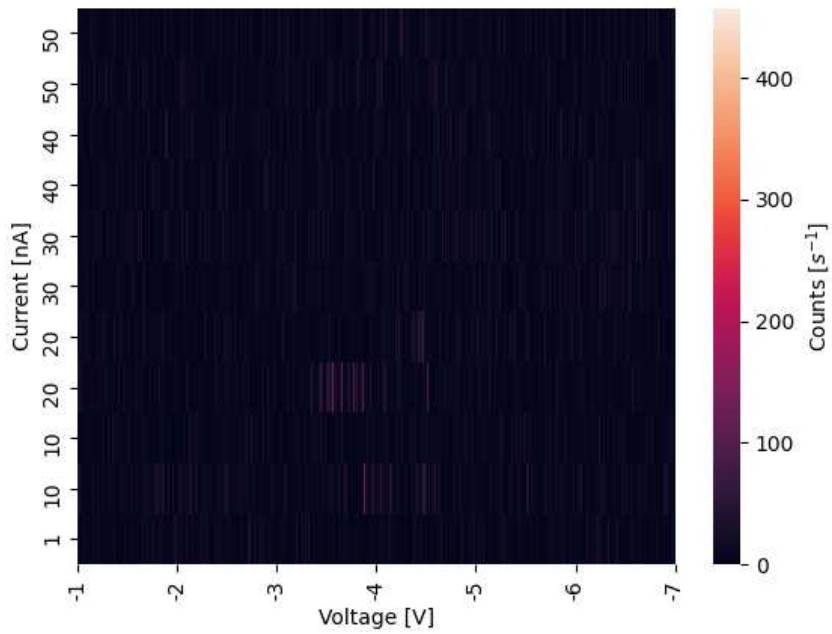


**Figure 62:** Heatmap of the spectroscopy measurement. We performed the experiment several times and compared in this plot the data of two measurements.

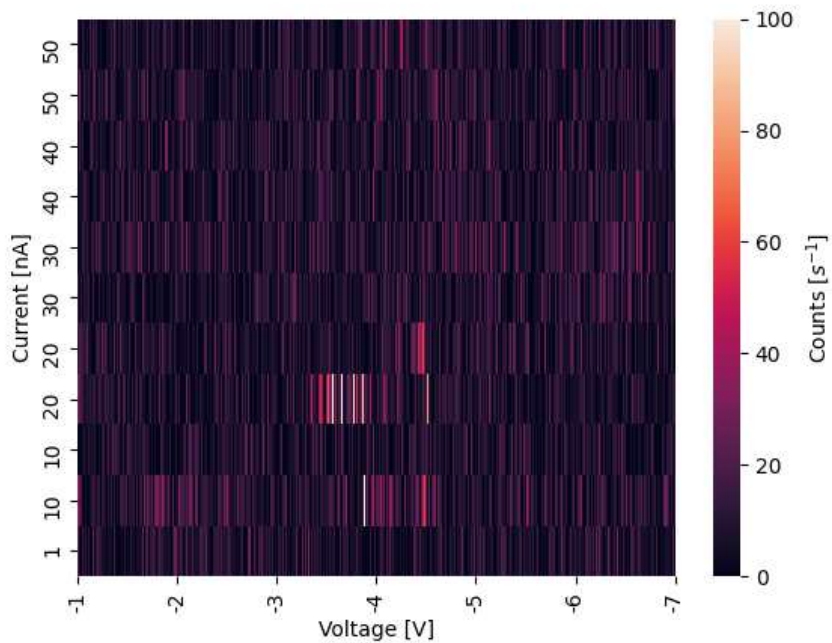


**Figure 63:** Heatmap of the spectroscopy measurement. We performed the experiment several times and compared in this plot the data of two measurements. To see the distribution of the photon counts better we changed the scale of the plot to a 4 times lower maximum. We noticed that the photon counts are not quite reproducible in the voltage/current space.

**5.2.2.3 LFM1F-1 fibre pointing directly at the junction** With the setup where the fibre was pointing directly at the junction we were not able to detect more photons than the darkcount. We averaged over the countrates taken over 5 minutes in step of 10s and compared it as countrates per second for 1 nA and 50 nA (see Figure 113).

**5.2.2.4 Optical setup** To optimize our system we changed the setup. The fibre was not pointing directly to the junction anymore but we built a lens system leading the light beam coming from the junction out of the STM chamber and focussing it on the fibre as described in section 4.1.6. As a first experiment we verified our setup described in Figure 46 and checked if the system is connected correctly as well as if the heatmap code (on Computer 1 of Figure 46) written by Berk Zengin is working. To do so we used the gold crystal as a sample and the tip was functionalized by indentation in the gold crystal. In Figure 64 on the right we have a 400 nm to 400 nm scanframe. On the left is the corresponding 200 px to 200 px heatmap. The maximal photon count per pixel was 1041. To see the results in the plot better we set the new minimum at 15 counts and the new maximum at 100 counts. To check for correlations between the current (right) and the photon counts (left) we used ImageJ. We imported the STM output of the current and the heatmap and adjusted the size of both images to 512 px to 512 px. Then we chose Process > FFT > FD Math and mirrored the heatmap stepwise over the horizontal and the vertical axis four times. In figure 65 we see no correlation. This can be explained with the theory described in section 6.1.

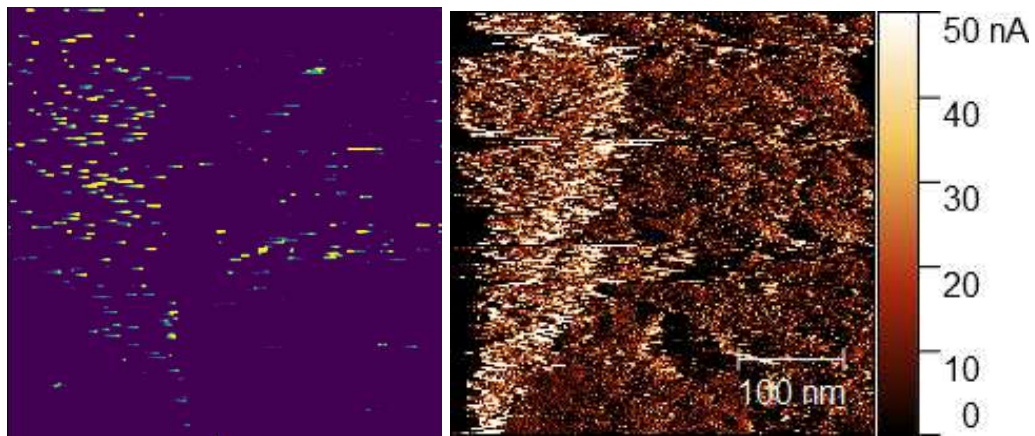


**Figure 64:** Right: 400 nm to 400 nm STM scanframe of the current (junction: Au(111) and functionalized tip by indentation in crystal) with 200 px to 200 px resolution and scanspeed of  $1600 \text{ nm s}^{-1}$ . Left: 200 px to 200 px heatmap with a photon count scale going from 15 to 100 counts.



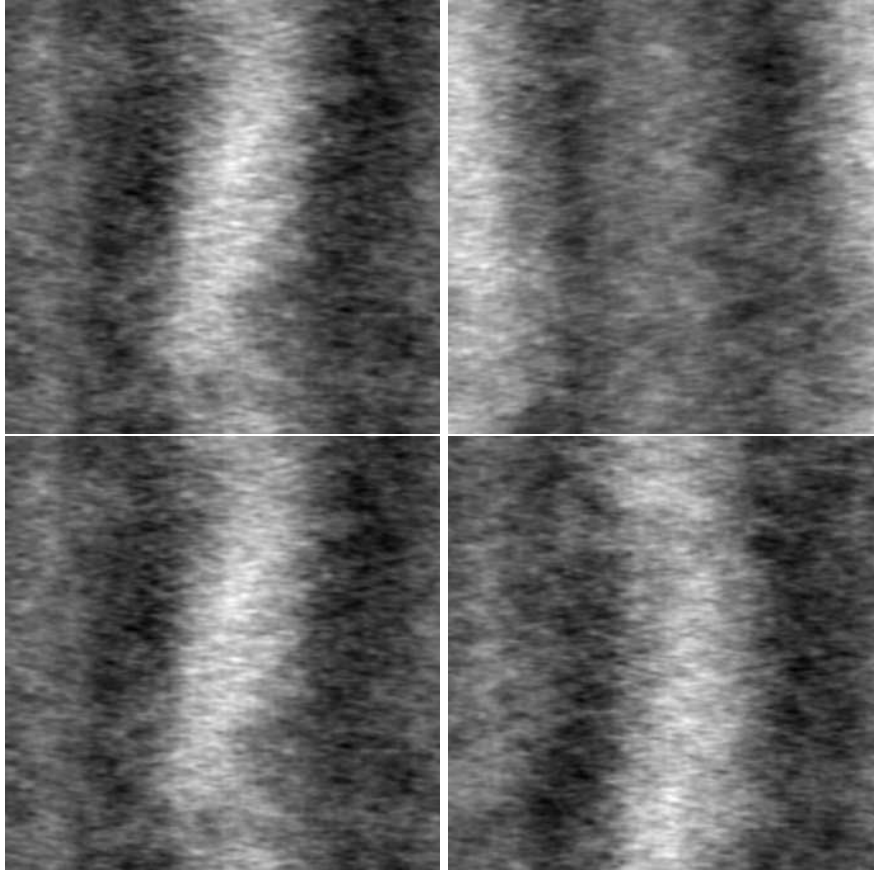


*Figure 65: Correlation figures of the current and the heatmap from Figure 64. On the top left we have the same orientation as in Figure 64. On the top right we mirrored the picture horizontally. On the bottom left we mirrored the picture from the step before vertically. On the bottom right we mirrored the picture from the last step horizontally.*

### 5.3 AuNP on HOPG ZYA

When we look at Figure 30 we see that we nearly discussed all components needed for the goal experiment. We used the following experiments and methods..

#### 5.3.1 Experiments and methods

**5.3.1.1 Dropcast** As described in Section 3.1.2 we had to figure out a concentration of AuNPs suitable for STM measurements. To perform the last experiments we performed the following recipe for the dropcast: (1) take 1  $\mu\text{L}$  of the dense AuNPs (OD10) and pipette it in a beaker glass, (2) take a new pipet tip and put 3  $\mu\text{L}$  of the OD1 AuNPs in the same beaker glass, (3) mix the 4  $\mu\text{L}$  of solution, (4) take 1  $\mu\text{L}$  from the mixed solution and dropcast it on HOPG ZYA, (5) let the drop evaporate, (6) put it in the oven for 15 min at 110  $^{\circ}\text{C}$ , (7) put the sample in the desiccator over night. Like this we found particles in nearly every scan. After approximately 3 scans of 800 nm to 800 nm we usually reached the edge of a cluster of AuNPs (see for example Figure 66 on the top left) which is a suitable region for picking up particles.

**5.3.1.2 Scanning particles** After depositing AuNP as described in Section 5.3.1.1, we noticed while scanning the particles with the STM that they were easily pushed around by the tip. This is ascribed to the weak AuNP/HOPG interaction and is a known problem as described in

section 2.2. In the pictures of Figure 66 we see four scans that followed each other. We start with two piles of particles (one on the top left and one on the bottom left). In the next scan the pile on the top left was pushed together and the pile on the bottom was shifted on the edge. To the next scan the particles on the top left tried to resist, but the one on the edge is already gone. We scanned a 800 nm to 800 nm with  $1600 \text{ nm s}^{-1}$  scanframe with 100 to 100 pixel, 10 nA,  $-3.8 \text{ V}$ , 90 % gain in up-down scanning mode on SCALA pro.

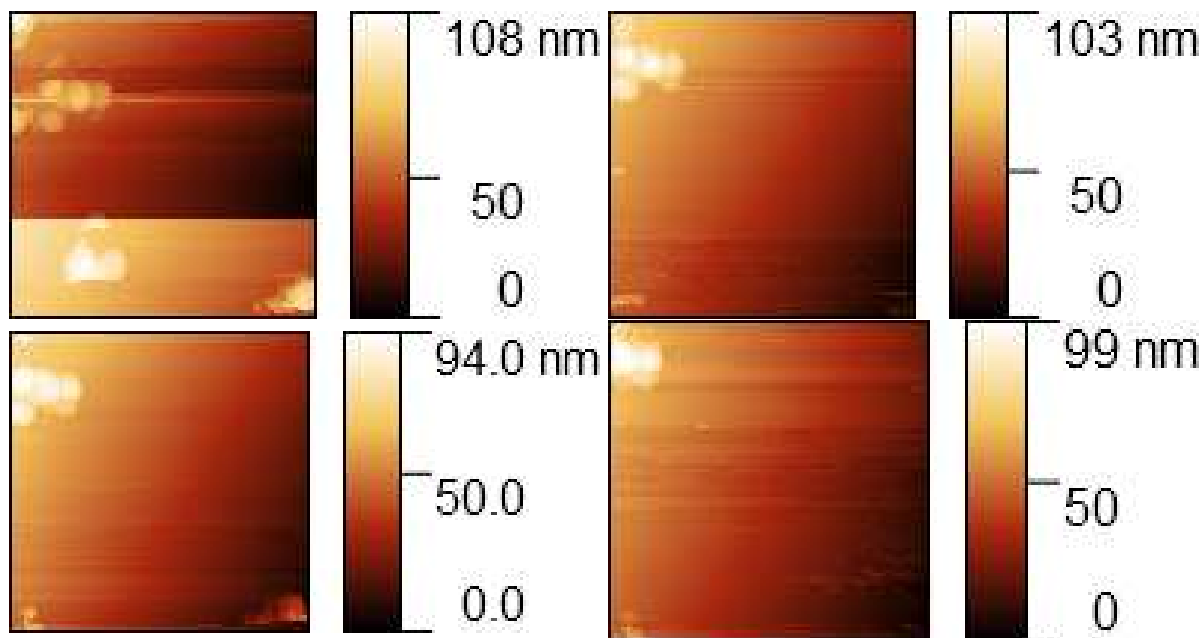


**Figure 66:** Topographic image of AuNPs dropcasted on HOPG and evolution after repeated scans of the same region. The tip pushes the AuNPs to the frame border as can be seen by the consecutive images.

We figured out the following scan settings to find a suitable region (single AuNPs lying on HOPG) for picking up particles as fast as possible: start with a 800 nm to 800 nm scan frame and  $1600 \text{ nm s}^{-1}$ , already scanning with  $-3.8 \text{ V}$ , currents around 0.2 nA and a loop gain over 60%.

**5.3.1.3 Picking up AuNPs** To functionalize the tip we needed to pick up a single AuNP. To do so the tip was positioned over the drop of the dropcasted AuNPs on HOPG (as in Figure 51) and scanned as described in the section above. Then we were picking up the AuNPs with the macro we implemented in SCALA pro > Nanostructuring > Mode: Single Event, Eventline: Macro below. We imported the nanostructuring language from the SCALA pro manual in the appendix in position Figure 72 and 73.

### Macro: Picking up AuNPs

```
; Voltage pulse ; Approach tip towards Sample
feedback, 0 ; Feedback loop off
set_v, 50 ; Gap voltage = 50mV
set_z, -15.0 ; Approach tip 15 nm towards the sample
delay, 1000000 ; 1000000 ms delay
set_z, 75.0 ; Pull tip away
delay, 1000 ; 1000 ms delay
reset_z ; Return to regulated position
delay, 1000000 ; 1000000 ms delay
reset_v ; Return to original gap voltage
reset_feedback ; Feedbackloop on
```

## 5.3.2 Results

**5.3.2.1 Picking up AuNPs** In the first experiments we realized that we were not picking up particles but poking them (see Figure 67).

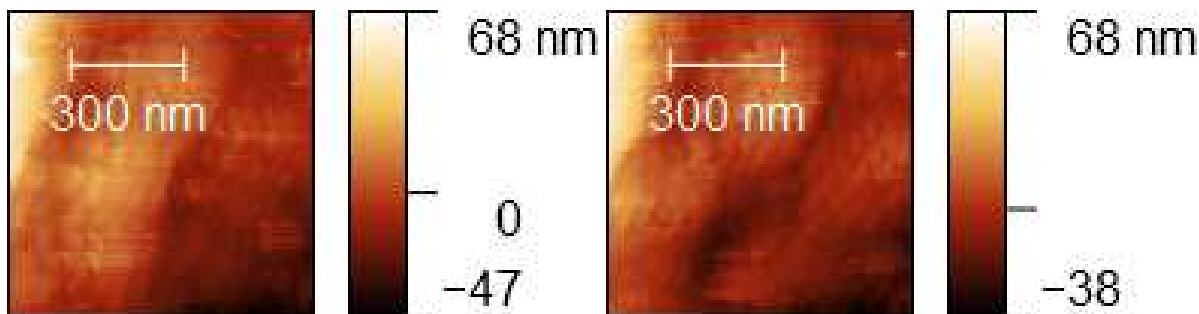


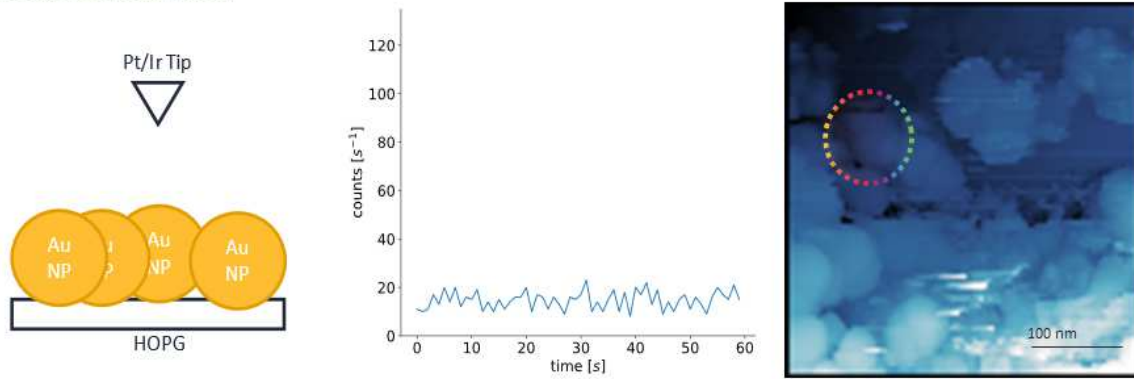
*Figure 67: Before and after the poking a pile of AuNPs dropcasted on HOPG.*

We went to edge of particle piles as described in Figure 66 on the top left.

We repeated the AuNP transfer to the tip several times until we found a the example from Figure 68. We noticed a similar shifting effect as described in figure 60. On the end of the day or before inserting a new tip in the system we poked in a pile of gold particles and detected higher count rates than when we only picked up one particle. Qualitatively, the attached AuNP behaved in similar fashion but we were still struggling to obtain reproducibly count rates.

In Figure 68 we describe the final experiment and its results. In the top row we have the photon count measurements from the junction with a naked Pt/Ir tip and AuNPs. In the bottom row we detected the light coming from the junction of a functionalized tip with AuNPs and AuNPs. We scanned the 400 nm to 400 nm scanframe with 100 px to 100 px resolution,  $1200 \text{ nm s}^{-1}$ ,  $-3.8 \text{ V}$ , currents around 50 nA and a loop gain of 60% scanning in up-down mode on SCALA pro.

**Before tip functionalization**



**After tip functionalization**

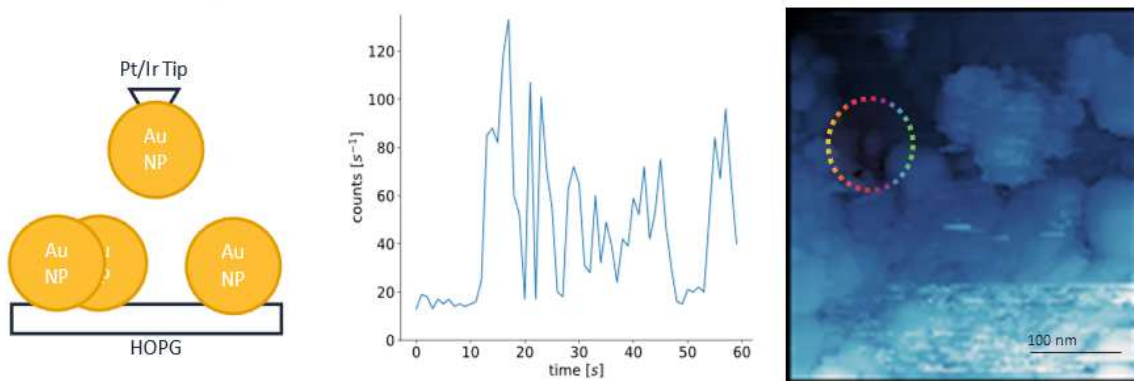


**Figure 68:** Process and results of the last experiment. Top row: Photon count measurements from the junction with a naked Pt/Ir tip and AuNPs, Bottom row: Photon count measurements from the junction of a functionalized tip with AuNPs and AuNPs. Further results are described in the text.

Before the tip functionalization the SPD detected the count rate in the middle of the top row in Figure 68, which corresponds to the photon count rate of the room. It is a little higher than the dark count rate of the SPD (8 to 9 photons per second) since we were not able to eliminate every light source in the room.

Then we picked up the one particular particle marked with a rainbow circle in Figure 68 using the macro described above.

After tip functionalization we recorded the photon count rate again (see bottom row middle of Figure 68) and the corresponding scan on the right.

## Part IV

# Conclusion and outlook

---

Luminescent scanning tunneling microscopy (STML) is a technique that combines the high-resolution imaging capabilities of STM with the ability to detect and map the optical emission of a sample at the nanoscale. In this master thesis, we present the development of a setup for STML, where we attached gold nanoparticles (AuNPs) onto the apex of tungsten or Pt/Ir tips. We verified our luminescent setup and found that AuNPs can serve as plasmonic tips for STML. After all the experiments we performed and the experience we gained we were able to perform the final experiment: (1) We dropcast the right amount of AuNPs on HOPG added on a sampleholder to (2) insert it attached to the lensholder in the VTSTM. (3) We prepared a Pt/Ir tip and installed it to (4) collect photons coming from the junction of Pt/Ir tip with AuNPs on HOPG. We detected the darkcount rate of the room. (5) Then we functionalized the same tip at the same location by picking up one AuNP to (6) successfully collect photons coming from the junction of functionalized Pt/Ir tip with AuNPs on HOPG. We were not able to achieve a reproducibility with the setup and conditions (air, RT) we were experimenting with.

---

As an outlook we suggest following experiments

- Test reproducibility  
We can test the reproducibility by performing the experiments with a vacuum and lower temperatures or cleaning the samples. We should test and optimize the materials in the vacuum which are the sample, tip and lensholder with collimating lens. The gold crystal we used was never cleaned and we do not know what purpose it served before we found it in the VTSTM.
- Increase the photon yield  
One easy and fast way to increase the yield is adding more AuNPs to the tip. Using AuNPs for tip functionalization lead to lower photon yields than using a tip indented in the Au(111) crystal. Before changing the tip we were indenting the tip in a pile of particles which already lead to higher photon yields. We guess that would still be an improvement compared to indenting in a gold crystal since "the last particle" produces the luminescent tip with a defined and tunable radius. Probably TEM pictures of the tip can help in the understanding of how one particle vs. several particles arrange at the tip apex. Another more time and resource consuming possibility to increase the photon yield is the optimization of the geometry of the collecting system. There are groups performing LSTM with really elaborate setups.
- Optimize scanning conditions  
It was challenging to scan the particles on HOPG since the tip was shifting around the particles. One possibility is to search for a material substituting the HOPG.
- Optimize particle distribution  
We already achieved a good particle distribution. But the distribution of the particles Nanopartz sent to us would still be perfect. We could investigate the use of TEM grids further. We already have gold grids.

- Functionalize with different plasmonic particles  
There is a variety of plasmonic particles. We verified that it is possible to pick a nanoparticle up with the tip and perform LSTM experiments. It would be interesting to check in which way different plasmonic nanoparticles lead to different results. There are for example different shapes of particles made of the same material. We already ordered hollow gold nanoparticles but never tested them. There are starshaped particles probably leading to a sharper tip. It would be interesting to insert a magnetic particle or a particle with excitons. We could check if a sphere of some random material in nanoparticle shape covered in gold can be used as a tip. To use the particles in the STM some limitations to keep in mind are conductivity and vacuum compatibility.
- Determine the wavelength  
One information we were missing was the energy of photons we got from the junction. To compare different experiments with different shapes or materials of plasmonic particles it would be interesting to find a way determining the spectra of the light.

## References

- <sup>1</sup>R. Berndt, “Photon emission from the scanning tunneling microscope”, in *Scanning probe microscopy: analytical methods*, edited by R. Wiesendanger, NanoScience and Technology (Springer, Berlin, Heidelberg, 1998), pp. 97–134.
- <sup>2</sup>K. Kuhnke, C. Große, P. Merino, and K. Kern, “Atomic-scale imaging and spectroscopy of electroluminescence at molecular interfaces”, *Chemical Reviews* **117**, Publisher: American Chemical Society, 5174–5222 (2017).
- <sup>3</sup>S. A. Maier, *Plasmonics - fundamentals and applications* (Springer, New York, U. S. A., 2007), 17-18.
- <sup>4</sup>K. Vasilev, B. Doppagne, T. Neuman, A. Rosławska, H. Bulou, A. Boeglin, F. Scheurer, and G. Schull, “Internal stark effect of single-molecule fluorescence”, *Nature Communications* **13**, 677 (2022).
- <sup>5</sup>S. Cao, A. Rosławska, B. Doppagne, M. Romeo, M. Féron, F. Chérioux, H. Bulou, F. Scheurer, and G. Schull, “Energy funnelling within multichromophore architectures monitored with subnanometre resolution”, *Nature Chemistry* **13**, 766–770 (2021).
- <sup>6</sup>J. Doležal, S. Canola, P. Hapala, R. C. de Campos Ferreira, P. Merino, and M. Švec, “Real space visualization of entangled excitonic states in charged molecular assemblies”, *ACS Nano* **16**, 1082–1088 (2022).
- <sup>7</sup>G. Schull, N. Néel, P. Johansson, and R. Berndt, “Electron-plasmon and electron-electron interactions at a single atom contact”, *Physical Review Letters* **102**, 057401 (2009).
- <sup>8</sup>B. Doppagne and G. Schull, “Hyper-resolved fluorescence microscopy with STM”, PhD thesis (Institut de physique et chimie des matériaux (Strasbourg), Feb. 3, 2020).
- <sup>9</sup>B. Voigtländer, *Scanning probe microscopy: atomic force microscopy and scanning tunneling microscopy*, NanoScience and Technology (Springer, Berlin, Heidelberg, 2015).
- <sup>10</sup>J. Tersoff and D. R. Hamann, “Theory of the scanning tunneling microscope”, *Physical Review B* **31**, 805–813 (1985).
- <sup>11</sup>J. Bardeen, “Tunnelling from a many-particle point of view”, *Physical Review Letters* **6**, Publisher: American Physical Society, 57–59 (1961).
- <sup>12</sup>J. W. Verhoeven, “Glossary of terms used in photochemistry (IUPAC recommendations 1996)”, *Pure and Applied Chemistry* **68**, 2223–2286 (1996).
- <sup>13</sup>J. K. Gimzewski, J. K. Sass, R. R. Schlitter, and J. Schott, “Enhanced photon emission in scanning tunnelling microscopy”, *Europhysics Letters (EPL)* **8**, 435–440 (1989).
- <sup>14</sup>S. Hüfner, *Photoelectron spectroscopy: principles and applications*, Google-Books-ID: vhjp-CAAAQBAJ (Springer Science & Business Media, Nov. 11, 2013), 525 pp.
- <sup>15</sup>A. V. Zayats, I. I. Smolyaninov, and A. A. Maradudin, “Nano-optics of surface plasmon polaritons”, *Physics Reports* **408**, 131–314 (2005).
- <sup>16</sup>F. Rossel, M. Pivetta, and W.-D. Schneider, “Luminescence experiments on supported molecules with the scanning tunneling microscope”, *Surface Science Reports* **65**, 129–144 (2010).
- <sup>17</sup>C. Zhang, L. Chen, R. Zhang, and Z. Dong, “Scanning tunneling microscope based nanoscale optical imaging of molecules on surfaces”, *Japanese Journal of Applied Physics* **54**, 08LA01 (2015).

- <sup>18</sup>J.-B. Michel, Y. K. Shen, A. P. Aiden, A. Veres, M. K. Gray, THE GOOGLE BOOKS TEAM, J. P. Pickett, D. Hoiberg, D. Clancy, P. Norvig, J. Orwant, S. Pinker, M. A. Nowak, and E. L. Aiden, “Quantitative analysis of culture using millions of digitized books”, *Science* **331**, Publisher: American Association for the Advancement of Science, 176–182 (2011).
- <sup>19</sup>J. Lambe and S. L. McCarthy, “Light emission from inelastic electron tunneling”, *Physical Review Letters* **37**, Publisher: American Physical Society, 923–925 (1976).
- <sup>20</sup>R. Young, J. Ward, and F. Scire, “The topografiner: an instrument for measuring surface microtopography”, *Review of Scientific Instruments* **43**, Publisher: American Institute of Physics, 999–1011 (1972).
- <sup>21</sup>J. K. Gimzewski, B. Reihl, J. H. Coombs, and R. R. Schlittler, “Photon emission with the scanning tunneling microscope”, *Zeitschrift fuer Physik B Condensed Matter* **72**, 497–501 (1988).
- <sup>22</sup>M. Sigrist, “Solid state theory”, Vorlesungsmanuskript, Vorlesungsmanuskript, Institut f ur Theoretische Physik ETH, 2020.
- <sup>23</sup>A. G. Mal’shukov, “Surface-enhanced raman scattering. the present status”, *Physics Reports* **194**, 343–349 (1990).
- <sup>24</sup>U. C. Fischer and D. W. Pohl, “Observation of single-particle plasmons by near-field optical microscopy”, *Physical Review Letters* **62**, Publisher: American Physical Society, 458–461 (1989).
- <sup>25</sup>A. V. Zayats, “Electromagnetic field enhancement in the context of apertureless near-field microscopy”, *Optics Communications* **161**, 156–162 (1999).
- <sup>26</sup>P. Johansson, R. Monreal, and P. Apell, “Theory for light emission from a scanning tunneling microscope”, *Physical Review B* **42**, 9210–9213 (1990).
- <sup>27</sup>J.-T. Lü, R. B. Christensen, and M. Brandbyge, “Light emission and finite-frequency shot noise in molecular junctions: from tunneling to contact”, *Physical Review B* **88**, Publisher: American Physical Society, 045413 (2013).
- <sup>28</sup>N. L. Schneider, G. Schull, and R. Berndt, “Optical probe of quantum shot-noise reduction at a single-atom contact”, *Physical Review Letters* **105**, Publisher: American Physical Society, 026601 (2010).
- <sup>29</sup>B. N. J. Persson and A. Baratoff, “Theory of photon emission in electron tunneling to metallic particles”, *Physical Review Letters* **68**, Publisher: American Physical Society, 3224–3227 (1992).
- <sup>30</sup>R. W. Rendell and D. J. Scalapino, “Surface plasmons confined by microstructures on tunnel junctions”, *Physical Review B* **24**, Publisher: American Physical Society, 3276–3294 (1981).
- <sup>31</sup>R. W. Rendell, D. J. Scalapino, and B. Mühlischlegel, “Role of local plasmon modes in light emission from small-particle tunnel junctions”, *Physical Review Letters* **41**, Publisher: American Physical Society, 1746–1750 (1978).
- <sup>32</sup>R. L. Olmon, B. Slovick, T. W. Johnson, D. Shelton, S.-H. Oh, G. D. Boreman, and M. B. Raschke, “Optical dielectric function of gold”, *Physical Review B* **86**, Publisher: American Physical Society, 235147 (2012).
- <sup>33</sup>M. G. Boyle, J. Mitra, and P. Dawson, “Infrared emission from tunneling electrons: the end of the rainbow in scanning tunneling microscopy”, *Applied Physics Letters* **94**, 233118 (2009).
- <sup>34</sup>P. Johansson and R. Monreal, “Theory for photon emission from a scanning tunneling microscope”, *Zeitschrift fuer Physik B Condensed Matter* **84**, 269–275 (1991).



- <sup>35</sup>D. Hone, B. Mühlischlegel, and D. J. Scalapino, “Theory of light emission from small particle tunnel junctions”, *Applied Physics Letters* **33**, Publisher: American Institute of Physics, 203–204 (1978).
- <sup>36</sup>I. Smolyaninov, A. Zayats, and O. Keller, “The effect of the surface enhanced polariton field on the tunneling current of a STM”, *Physics Letters A* **200**, 438–444 (1995).
- <sup>37</sup>S. Grafström, “Photoassisted scanning tunneling microscopy”, *Journal of Applied Physics* **91**, Publisher: American Institute of Physics, 1717–1753 (2002).
- <sup>38</sup>D. W. Pohl and D. Courjon, eds., *Near field optics* (Springer Netherlands, Dordrecht, 1993).
- <sup>39</sup>R. Möller, U. Albrecht, J. Boneberg, B. Koslowski, P. Leiderer, and K. Dransfeld, “Detection of surface plasmons by scanning tunneling microscopy”, *Journal of Vacuum Science & Technology B: Microelectronics and Nanometer Structures Processing, Measurement, and Phenomena* **9**, Publisher: American Institute of Physics, 506–509 (1991).
- <sup>40</sup>A. Martín-Jiménez, A. I. Fernández-Domínguez, K. Lauwaet, D. Granados, R. Miranda, F. J. García-Vidal, and R. Otero, “Unveiling the radiative local density of optical states of a plasmonic nanocavity by STM”, *Nature Communications* **11**, Number: 1 Publisher: Nature Publishing Group, 1021 (2020).
- <sup>41</sup>G. Mie, “Beiträge zur optik trüber medien, speziell kolloidaler metallösungen”, *Annalen der Physik* **330**, 377–445 (1908).
- <sup>42</sup>D. D. Evanoff and G. Chumanov, “Synthesis and optical properties of silver nanoparticles and arrays”, *Chemphyschem: A European Journal of Chemical Physics and Physical Chemistry* **6**, 1221–1231 (2005).
- <sup>43</sup>N. G. Bastús, J. Piella, and V. Puntès, “Quantifying the sensitivity of multipolar (dipolar, quadrupolar, and octapolar) surface plasmon resonances in silver nanoparticles: the effect of size, composition, and surface coating”, *Langmuir* **32**, Publisher: American Chemical Society, 290–300 (2016).
- <sup>44</sup>P. B. Johnson and R. W. Christy, “Optical constants of the noble metals”, *Physical Review B* **6**, Publisher: American Physical Society, 4370–4379 (1972).
- <sup>45</sup>L. Tao, S. Deng, H. Gao, H. Lv, X. Wen, and M. Li, “Experimental investigation of the dielectric constants of thin noble metallic films using a surface plasmon resonance sensor”, *Sensors* **20**, Number: 5 Publisher: Multidisciplinary Digital Publishing Institute, 1505 (2020).
- <sup>46</sup>V. Giannini, A. I. Fernández-Domínguez, S. C. Heck, and S. A. Maier, “Plasmonic nanoantennas: fundamentals and their use in controlling the radiative properties of nanoemitters”, *Chemical Reviews* **111**, Publisher: American Chemical Society, 3888–3912 (2011).
- <sup>47</sup>K. Meguro, K. Sakamoto, R. Arafune, M. Satoh, and S. Ushioda, “Origin of multiple peaks in the light emission spectra of a Au(111) surface induced by the scanning tunneling microscope”, *Physical Review B* **65**, Publisher: American Physical Society, 165405 (2002).
- <sup>48</sup>M. B. Raschke and C. Lienau, “Apertureless near-field optical microscopy: tip-sample coupling in elastic light scattering”, *Applied Physics Letters* **83**, Publisher: American Institute of Physics, 5089–5091 (2003).
- <sup>49</sup>D. D. Evanoff and G. Chumanov, “Size-controlled synthesis of nanoparticles. 2. measurement of extinction, scattering, and absorption cross sections”, *The Journal of Physical Chemistry B*, Publisher: American Chemical Society (2004).
- <sup>50</sup>T. Kalkbrenner, M. Ramstein, J. Mlynek, and V. Sandoghdar, “A single gold particle as a probe for apertureless scanning near-field optical microscopy”, *Journal of Microscopy* **202**, 72–76 (2001).

- <sup>51</sup>P. Anger, P. Bharadwaj, and L. Novotny, “Enhancement and quenching of single-molecule fluorescence”, *Physical Review Letters* **96**, Publisher: American Physical Society, 113002 (2006).
- <sup>52</sup>P. Hepperle, W. Y. Baek, H. Nettelbeck, and H. Rabus, “Deposition of gold nanoparticles on a self-supporting carbon foil”, *Particle & Particle Systems Characterization* **39**, [\\_eprint: https://onlinelibrary.wiley.com/doi/pdf/10.1002/ppsc.202200136](https://onlinelibrary.wiley.com/doi/pdf/10.1002/ppsc.202200136), 2200136 (2022).
- <sup>53</sup>A. Kaliyaraj Selva Kumar, Y. Zhang, D. Li, and R. G. Compton, “A mini-review: how reliable is the drop casting technique?”, *Electrochemistry Communications* **121**, 106867 (2020).
- <sup>54</sup>C. M. Alexander, “Gravitational sedimentation of gold nanoparticles”, *Journal of Colloid and Interface Science*, 10 (2013).
- <sup>55</sup>J. Midelet, A. El-Sagheer, T. Brown, A. G. Kanaras, and M. H. V. Werts, “The sedimentation of colloidal nanoparticles in solution and its study using quantitative digital photography”, *Particle & Particle Systems Characterization* **Volume 34** (2017).
- <sup>56</sup>*Spherical gold nanoparticles - nanopartz*, [https://www.nanopartz.com/spherical\\_gold\\_nanoparticles.asp](https://www.nanopartz.com/spherical_gold_nanoparticles.asp) (visited on 03/10/2023).
- <sup>57</sup>I. Lopez-Salido, D. C. Lim, R. Dietsche, N. Bertram, and Y. D. Kim, “Electronic and geometric properties of au nanoparticles on highly ordered pyrolytic graphite (HOPG) studied using x-ray photoelectron spectroscopy (XPS) and scanning tunneling microscopy (STM)”, *The Journal of Physical Chemistry B* **110**, 1128–1136 (2006).
- <sup>58</sup>B. Uder and U. Hartmann, “A convenient method for large-scale STM mapping of freestanding atomically thin conductive membranes”, *Review of Scientific Instruments* **88**, Publisher: American Institute of Physics, 063702 (2017).
- <sup>59</sup>*UHV4i ultra-high vacuum compatible electro spray deposition – molecular spray ltd*, <https://www.molecularspray.co.uk/products/uhv4i-electrospray-deposition-source/> (visited on 03/13/2023).
- <sup>60</sup>E. Fornari, C. J. Roberts, R. H. Temperton, and J. N. O’Shea, “Electrospray deposition in vacuum as method to create functionally active protein immobilization on polymeric substrates”, *Journal of Colloid and Interface Science* **453**, 252–259 (2015).
- <sup>61</sup>J. N. O’Shea, J. B. Taylor, J. C. Swarbrick, G. Magnano, L. C. Mayor, and K. Schulte, “Electrospray deposition of carbon nanotubes in vacuum”, *Nanotechnology* **18**, 035707 (2007).
- <sup>62</sup>C. J. Satterley, L. M. A. Perdigão, A. Saywell, G. Magnano, A. Rienzo, L. C. Mayor, V. R. Dhanak, P. H. Beton, and J. N. O’Shea, “Electrospray deposition of fullerenes in ultra-high vacuum: *in situ* scanning tunneling microscopy and photoemission spectroscopy”, *Nanotechnology* **18**, 455304 (2007).
- <sup>63</sup>*Stingray f-145 sony ICX285 EXview HAD sensor, IEEE 1394b - allied vision*, <https://www.alliedvision.com/en/camera-selector/detail/stingray/f-145/> (visited on 03/13/2023).
- <sup>64</sup>*Multimode fiber and patch cables with lensed tips*, <https://www.thorlabs.com> (visited on 03/13/2023).
- <sup>65</sup>*Vimba SDK for machine vision cameras*, Allied Vision, <https://www.alliedvision.com/en/products/vimba-sdk/> (visited on 03/15/2023).
- <sup>66</sup>C. A. Schneider, W. S. Rasband, and K. W. Eliceiri, “NIH image to ImageJ: 25 years of image analysis”, *Nature Methods* **9**, 671–675 (2012).
- <sup>67</sup>J. Martínez-Blanco and S. Fölsch, “Light emission from ag(111) driven by inelastic tunneling in the field emission regime”, *Journal of Physics: Condensed Matter* **27**, Publisher: IOP Publishing, 255008 (2015).

- <sup>68</sup>S. Hembacher, F. J. Giessibl, J. Mannhart, and C. F. Quate, “Revealing the hidden atom in graphite by low-temperature atomic force microscopy”, *Proceedings of the National Academy of Sciences* **100**, 12539–12542 (2003).
- <sup>69</sup>T. Stuchinskaya, M. Moreno, M. J. Cook, D. R. Edwards, and D. A. Russell, “Targeted photodynamic therapy of breast cancer cells using antibody-phthalocyanine-gold nanoparticle conjugates”, *Photochemical & Photobiological Sciences* **10**, 822–831 (2011).
- <sup>70</sup>X. Huang, I. H. El-Sayed, W. Qian, and M. A. El-Sayed, “Cancer cell imaging and photothermal therapy in the near-infrared region by using gold nanorods”, *Journal of the American Chemical Society* **128**, 2115–2120 (2006).
- <sup>71</sup>*Spherical gold nanoparticles - nanopartz - diagnostics*, [https://www.nanopartz.com/invitro\\_diagnostics\\_zeroorder.asp](https://www.nanopartz.com/invitro_diagnostics_zeroorder.asp).
- <sup>72</sup>I. Freestone, N. Meeks, M. Sax, and C. Higgitt, “The lycurgus cup — a roman nanotechnology”, *Gold Bulletin* **40**, 270–277 (2007).

## Appendix A Question and Answers

To perform STM luminescence experiments we need a functionalized tip. Usually W or Pt/Ir tips are forcefully indented in a gold or silver crystal. We wanted to test another approach by picking up a AuNP with a Pt/It tip. In the appendix (see section A), we included a Q&A section on gold nanoparticles.

- (I) Why does the solution containing the AuNPs need cooling?
- (II) Why shouldn't we freeze the solution?
- (III) What do the components citric acid and ether do?
- (IV) What is the particle density?
- (V) How do the nanoparticles sediment, if they do?
- (VI) Why is the solution red?

### A.1 Why does the solution need cooling?

The stability of the citric acid is given in the storage temperature of 2 °C to 8 °C.

### A.2 Why shouldn't we freeze the solution?

According to the manufacturer freezing causes irreversible aggregation of the AuNPs. Especially when combined with biomolecules.

### A.3 What does the component citric acid do?

Citrate provides a highly negatively charged surface which introduces a repulsive force preventing their coalescence.

*Table 5: Citrate buffer from Sigma Aldrich. The data from the table are from the data sheet or from Wikipedia.*

Ingredient	Physical properties
Citric acid	Concentration: $\geq 1 - < 10$ % Melting point 156 °C Boiling point 310 °C but decomposes from 175 °C
Chloroform	Concentration: $\geq 1 - < 3$ % Melting point -63.5 °C Boiling point 61.15 °C

### A.4 What does the component ether do?

The solution contains a proprietary surfactant as stabilizer. Surfactants lower the surface tension between all kind of combinations of liquids and gases and solids. We summarized some properties in the Table 6.

**Table 6:** Citrate buffer from Sigma Aldrich. The data from the table are from the data sheet or from Wikipedia.

Ingredient	Physical properties
Citric acid	Concentration: $\geq 1 - < 10$ % Melting point $156^\circ\text{C}$ Boiling point $310^\circ\text{C}$ but decomposes from $175^\circ\text{C}$
Chloroform	Concentration: $\geq 1 - < 3$ % Melting point $-63.5^\circ\text{C}$ Boiling point $61.15^\circ\text{C}$

## A.5 What is the particle density?

According to the datasheet the AuNPs have a molecular weight of  $196.97 \text{ g mol}^{-1}$ . The bottle is filled with 25 mL of solution containing the AuNPs. On the homepage of Sigma Aldrich we found that we can expect  $3.51 \times 10^{10}$  particles/mL. We calculate how many particles we could find in the droplet on the surface in the following manner: we used 1  $\mu\text{L}$  of the solution containing  $3.51 \times 10^7$  particles. In Figure 87 we see that the drop is approximately 2 mm of diameter. To check the size we used the table in Figure 69 listing the scaling factors of the optical microscope Mikon MBS-10-1.

**Tabelle 4 - Tabelle zur Vergrößerung der Mikroskopvergrößerung**

Gerundete Werte Legenden Koyatkah-Trommel, falten	Eine Abteilung Maßstab 0,1 mm	Seite 1 mm quadratisch
	entspricht dem Wert in der Anlage	entspricht dem Wert in der Anlage
0,6	0,17	1,7
1	0,1	1,0
2	0,05	0,5
4	0,025	0,25
7	0,014	0,14

**Figure 69:** To calculate the density of particles in a drop we looked at a dropcasted drop in the microscope MBS-10-1 (see Figure 87). To check the size of the drop we used the sizechart of the manufacturer.

The area of the drop is approximately  $A = \pi r^2 = \pi \cdot 1 \text{ mm}^2 = 3.14 \text{ mm}^2$ . We assume that in this area  $A$  the  $3.51 \times 10^7$  particles distribute evenly. This means in a scan range of 1  $\mu\text{m}$  we find 11 particles. Since we know that the particles are not distributed evenly we expect, that we will have large areas without particles.

## A.6 How do the nanoparticles sediment if they do?

There are reports that suggest that colloidal nanoparticles can sediment [55][54]. However, those reports were described for particles without citrate buffer that may inhibit or slow the sedimentation of the AuNP.

In order to homogenize the solution, several approaches are suggested like

- shaking
- using a pipette and pipette the solution "up-down"
- vortexing (with a vortex mixer - circular motion)

- sonicating (ultrasound motion)

According to the manufacturer Nanopartz the sedimentation of gold nanoparticles is reversible through sonication. However, our conclusion is, shaking the solution by hand is enough for our purpose.

### A.7 Why is the solution pink?

Gold nanoparticles interact with light. This interaction is strongly dictated by their environment, size and physical dimensions. To explain the pink color we use the concept of surface plasmons. Oscillating electric fields of a light ray propagating near a colloidal nanoparticle interact with the surface plasmons of the particle leading in a surface plasmon resonance with the frequency of visible light. [69, 70]

For gold nanoparticles ( $\approx 30$  nm), the surface plasmon resonance causes an absorption of blue-green light ( $\approx 450$  nm, in our case a peak at 531 nm), while red light ( $\approx 700$  nm) is reflected, yielding to the pink-red colour in transmission. In Figure 70 we see the absorbance of the used Nanopartz particles.

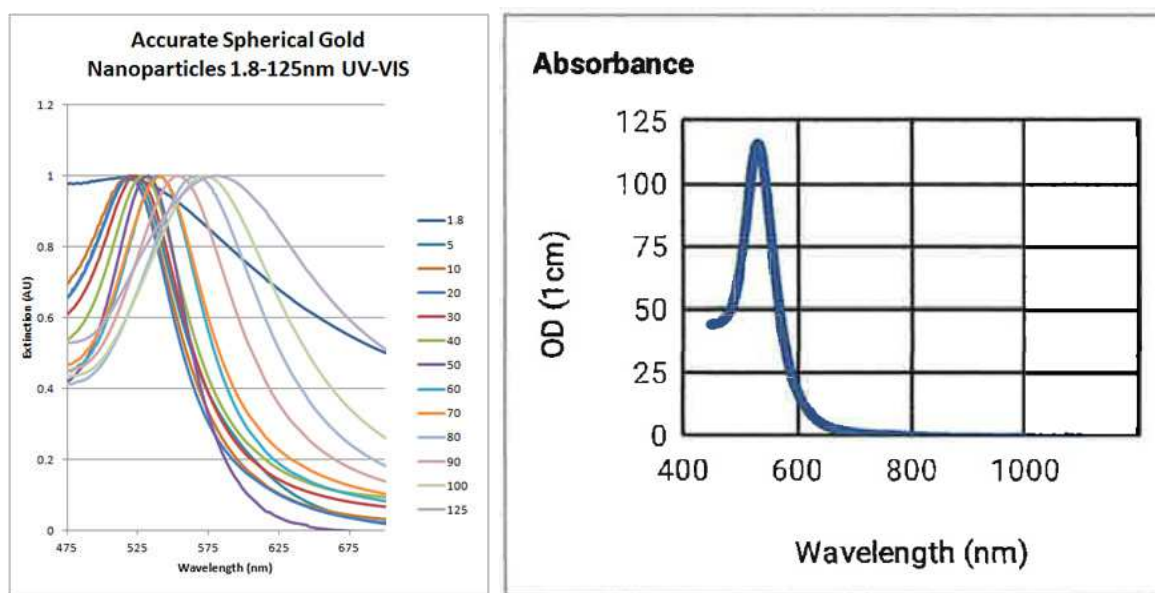


**Figure 70:** Extinction v.s. Wavelength plot for the solid gold spheres (left, [71]) and absorption vs. wavelength plot for our particles (right, surface plasmon resonance peak measured at 531 nm from Datasheet 75).

As particle size continues to increase, surface plasmon resonance wavelengths move into the infra red spectrum and most visible wavelengths are reflected. Those nanoparticles have a translucent color. The surface plasmon resonance can be tuned by varying the size or shape of the nanoparticles, leading to particles with tailored optical properties for different applications. This high degree of tunability of their optical properties makes AuNP and other NP attractive for luminescence applications.

Gold nanoparticles have been used since the 4th century for staining glass. This glass staining technique was already found in the roman Lycurgus cup. [72] The glass contains colloidal metallic particles leading to the green or pink appearance visible in Figure 71

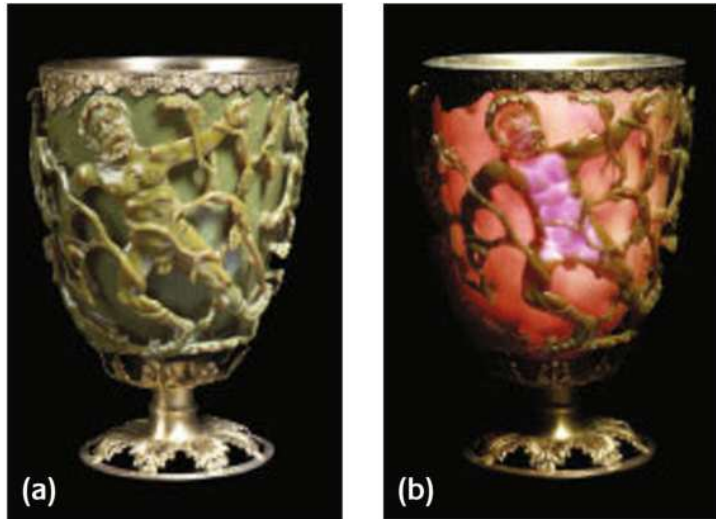


*Figure 71: The Lycurgus cup in reflected (a) and transmitted (b) light. ©The Trustees of the British Museum*

## Appendix B Setup


### B.1 Nanostructuring

*Figure 72: Pages from the SCALA pro manual. We used those commands to create the macros for poking gold and picking up the gold nanoparticles.*

Command	Parameters and Comment
feedback, flag	'flag' = 0: Switch feedback loop off (Status port signal 7 becomes low). 'flag' = 1: Switch feedback loop on (Status port signal 7 becomes high). Never forget to switch feedback loop on before a program ends.
set_v, v	Set gap voltage to 'v' volts. 'v' is in the range (-10.0 to 10.0) V or (-1.0 to 1.0) V, depending on the state of the corresponding range switch in the window 'Measurement Control'.
add_v, dv	Increase gap voltage by 'dv' volts. Before using 'add_v' first in an event program, always use 'set_v' to set a well defined start point.
reset_v	Return to the normal gap voltage set in 'Measurement Control'. If the gap voltage has been changed during an event program, always use 'reset_v' before the program ends.
set_z, z	Set tip height to 'z' nanometers with respect to the regulated position. Positive 'z' means larger distance from the sample. 'z' is restricted to the same range as in Spectroscopy Preset. (Usually the feedback loop should be switched off before changing z, because otherwise the regulator would always compensate the change.)
add_z, dz	Increase tip height by 'dz' nanometers. Before using 'add_z' first in an event program, always use 'set_z' to set a well defined start point.
reset_z	Return to regulated tip height. (Same as 'set_z, 0'). If the tip height has been changed during an event program, always use 'reset_z' before the program ends. (Usually use this command before reactivating the feedback loop.)
set_i0, i	Set feedback current set point to 'i' nanoamperes. 'i' is in the range 0...50 or 0...5, depending on the state of the corresponding range switch in the window 'Measurement Control'. (Changing the set point does not have any effect, when the feedback loop is off.)
add_i0, di	Increase feedback current set point by 'di' nanoamperes. Before using 'add_i0' first in an event program, always use 'set_i0' to set a well defined start point.
reset_i0	Return to the normal current set point set in 'Measurement Control'. If the current set point has been changed during an event program, always use 'reset_i0' before the program ends.
set_signal, n	Activate status port signal 'n'. The corresponding open collector output goes to low.



*Figure 73: Pages from the SCALA pro manual. We used those commands to create the macros for poking gold and picking up the gold nanoparticles. We used the pin numbers to make the plug in Figure 48. We see that signal 1 is active while moving forward.*

Command	Parameters and Comment
	<p>Signal numbers: 15 13 11 9 7 5 3 1</p> <p>Pin numbers: </p> <p>Signal numbers: 14 12 10 8 6 4 2 0</p> <p>Some signals are already used by the RTMC to indicate the state of the scan (1: Line forward, 2: Line backward, 7: Loop off, ...) and therefore are not suitable for use with this command.</p> <p>Signals 12, 13, 14, 15 (Pins 23, 11, 24, 12) are recommended for use as external triggers.</p>
reset_signal, n	Deactivate status port signal 'n'. The corresponding open collector output goes to high.
delay, t	Pause 't' microseconds. 't' = 10, 20, ..., 655350. (For delay longer than 0.6 seconds use 'loop_times'.)
loop_times, n	Repeat the following sequence of commands 'n' times. The end of the sequence is marked by 'loop_end'. 'n' = 1, 2, ..., 32767. (Loops can be nested.)
loop_end	Mark end of loop.

### Status Port

Signal	Bus Address	Name	Function
0	\$0100	SIG_FRAME	Active while scanning (Pause too!)
1	\$0102	SIG_L_FOR	Active while moving forward (1)
2	\$0104	SIG_L_BACK	Active while moving backward (1)
3	\$0106	SIG_SET_POINT	Inactive (high) while averaging (2)
4	\$0108	f.e.	
5	\$010A	f.e.	
6	\$010C	f.e.	
7	\$010E	SIG_FEEDBACK	Active when feedback loop is off (3)
8	\$0110	SIG_GAP	Active for 100µs, when Vgap changes (4)
9	\$0112	f.e.	
10	\$0114	f.e.	
11	\$0116	f.e.	
12	\$0118	---	Recommended for nanostructuring
13	\$011A	---	Recommended for nanostructuring
14	\$011C	---	Recommended for nanostructuring
15	\$011E	---	Recommended for nanostructuring

## B.2 Particles

Figure 74: Data sheets we received together with the AuNPs from Nanopartz.

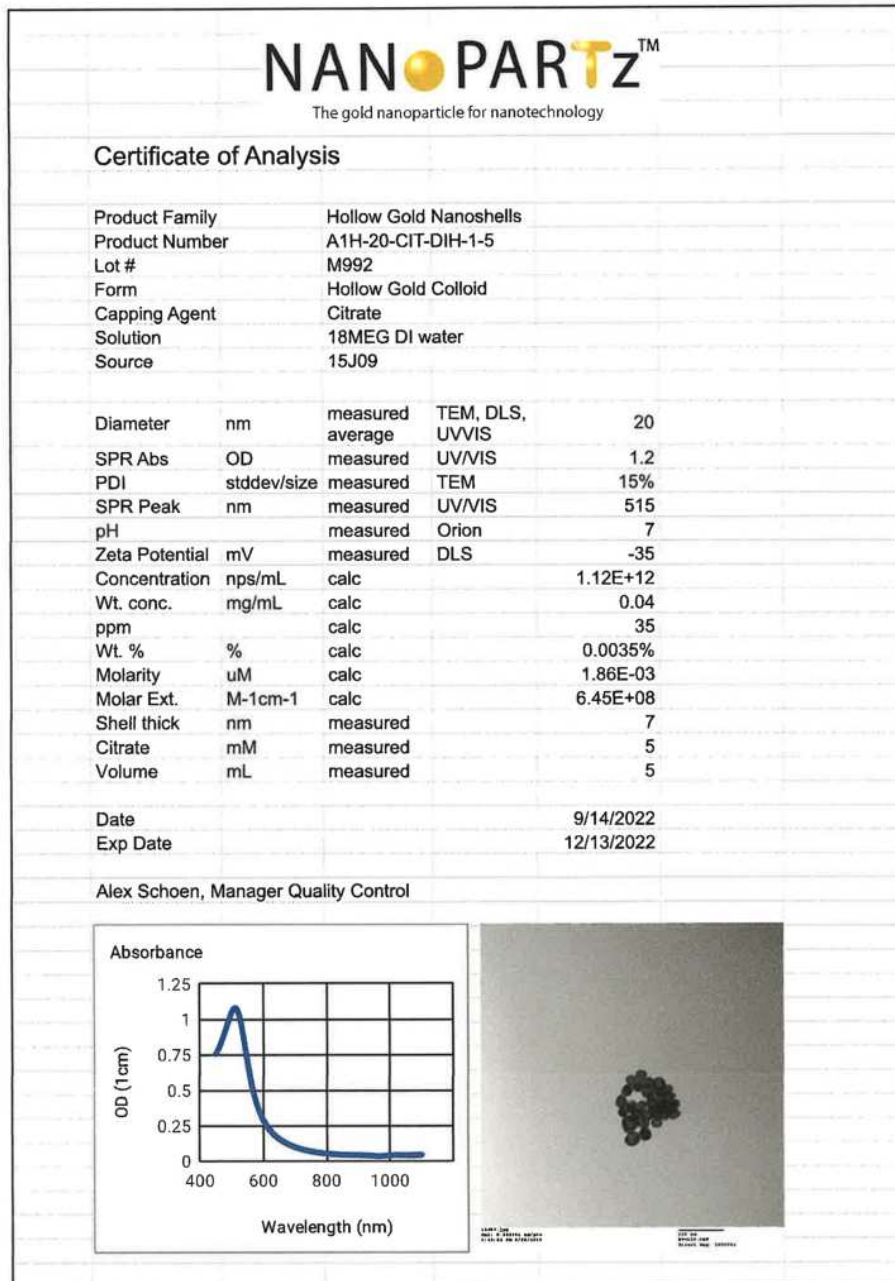


Figure 75: Data sheets we received together with the AuNPs from Nanopartz.

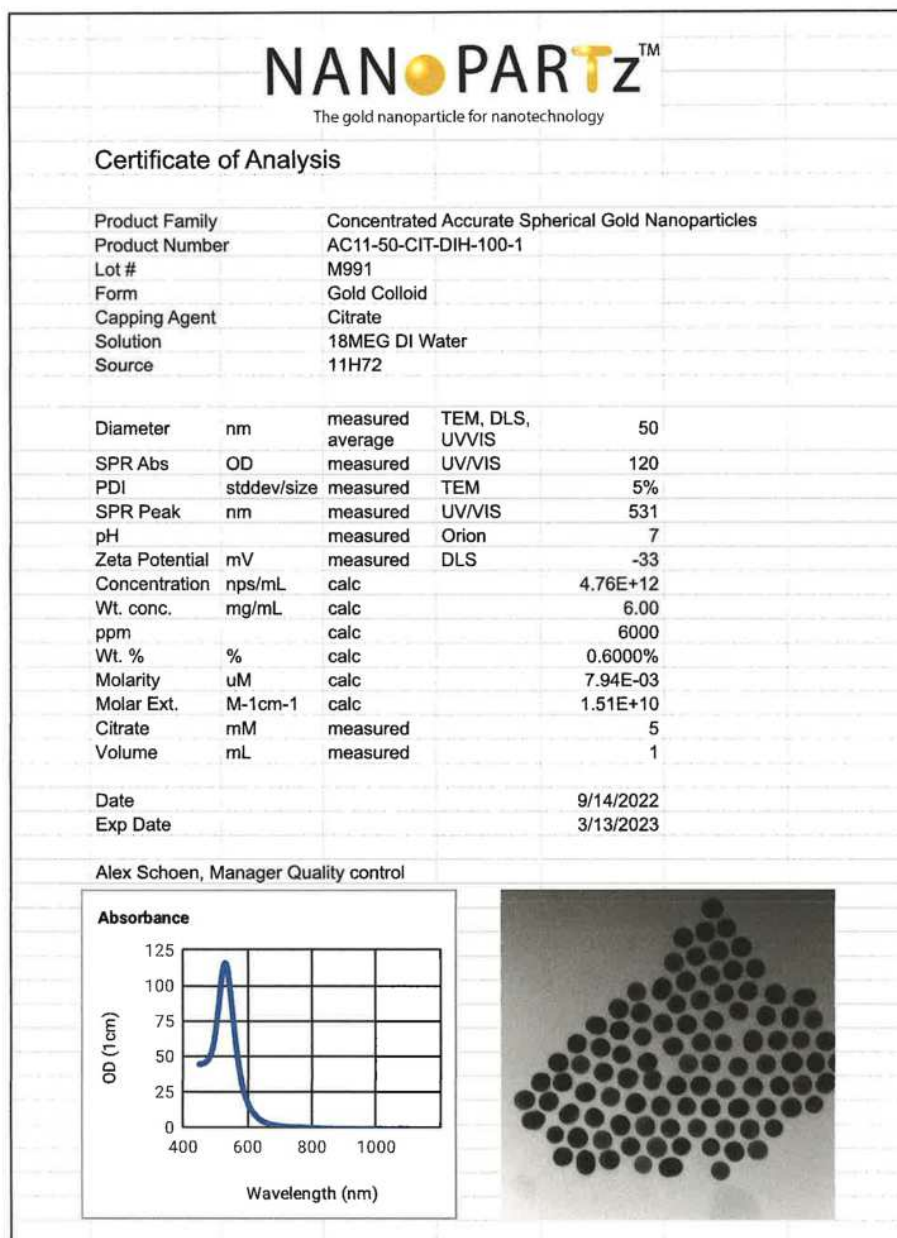


Figure 76: Data sheets we received together with the AuNPs from Nanopartz.

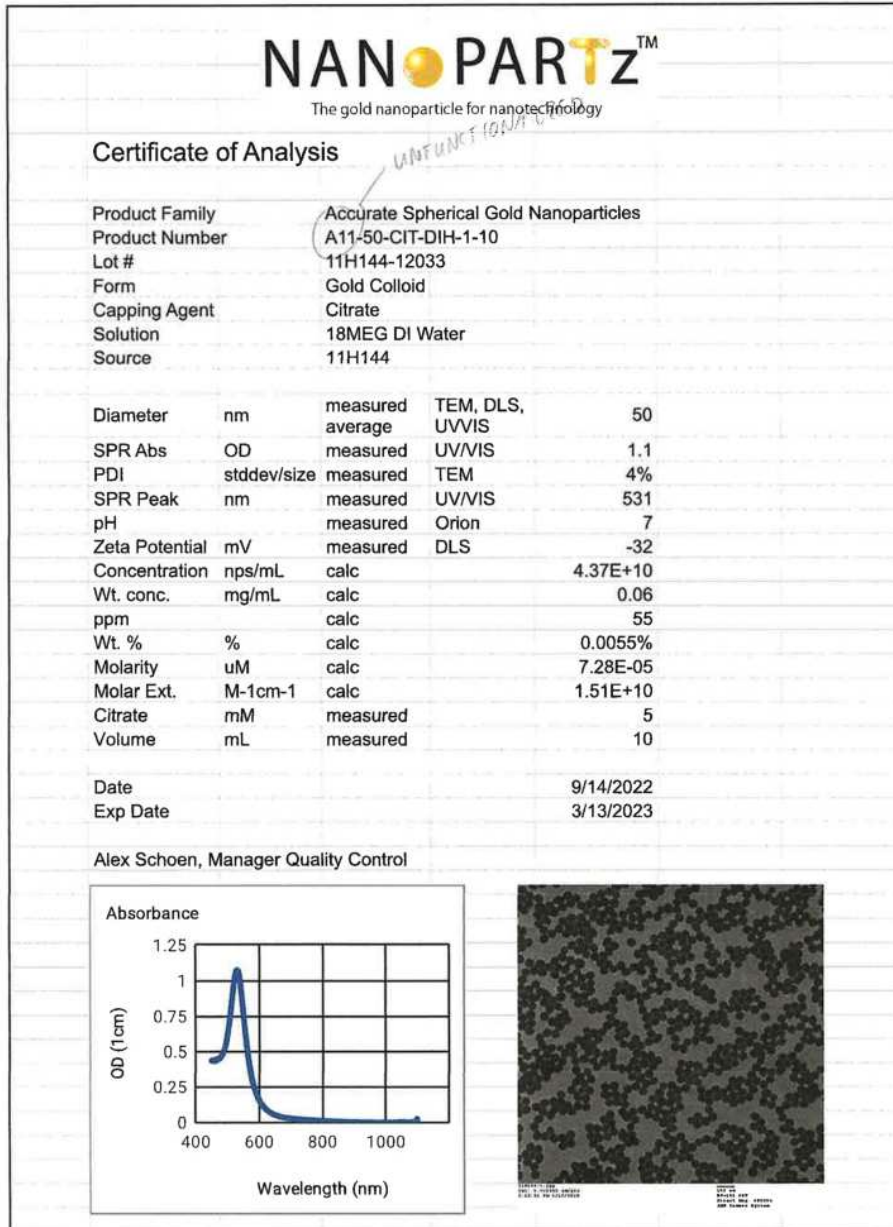




Figure 77: Data sheets we received together with the AuNPs from Nanopartz.



## Nanopartz Recommended Storage and Handling

### Storage

Table 1 Maximum shelf life times for Nanopartz products by family

Product	Shelf Life	Storage
All bare spherical, nanorod, microgold	6 months	4C
Functionalized products	3 months	4C
Organic	3 months	4C
Bare Nanowires	6 months	room temp

Do not freeze the nanoparticle products. In general, once conjugated, neutravidin and custom conjugations should see much greater shelf lives than when left unconjugated. For the longest shelf life, leave the functionalized products in their concentrated form and remove only what is immediately needed.

### Disposal

We recommend the customer consult their in house or local health and safety office. Please consult the specific SDS for that product.

### Handling

Some of our products may reversibly aggregate and settle with time in storage. In these cases, these particles may be resuspended by sonication for five minutes, followed by a two minute vortex.

In shipping, sometimes particles get lodged in the cap of the microcentrifuge container. A quick and easy solution is to put the tube on a vortex mixer for 3-5 seconds. Then centrifuge at less than <1000 revs/min for 30 seconds. This should recollect any particles back into the bulk reservoir.

### Dilution

Table 2. Recommended dilution buffers and methods

Product	Dilution Recommendation
Adsorbed Ligand	Please match the concentration of the adsorbed ligand specified on the COA
Functionalized, In Vitro	18 MEG DI Water, any salt based buffer
Organic Spherical, Nsol	Dilute with your choice of organic solvent

### Checking viability

To check the viability of the solutions, test the material using a UV VIS and match the spectrum to the original COA. Go here: <https://www.nanopartz.com/gold-nanoparticles-expiration-date.asp>.

### SDS

All Nanopartz SDS' may be found on the web at <https://www.nanopartz.com/sds.asp>.

### Product Use

Customer confirms that the products ordered will only be used by trained personnel in laboratories equipped for this purpose and are NOT PURCHASED FOR PERSONAL USE. Furthermore the products ordered will only be employed for Research Purposes or for In Vitro Diagnostic Use in case the products have been certified for this purpose. The user is acquainted with the use of these products and is aware of relevant regulations.

### Terms and Conditions

Terms and Conditions are listed here: <https://www.nanopartz.com/legal.asp>.

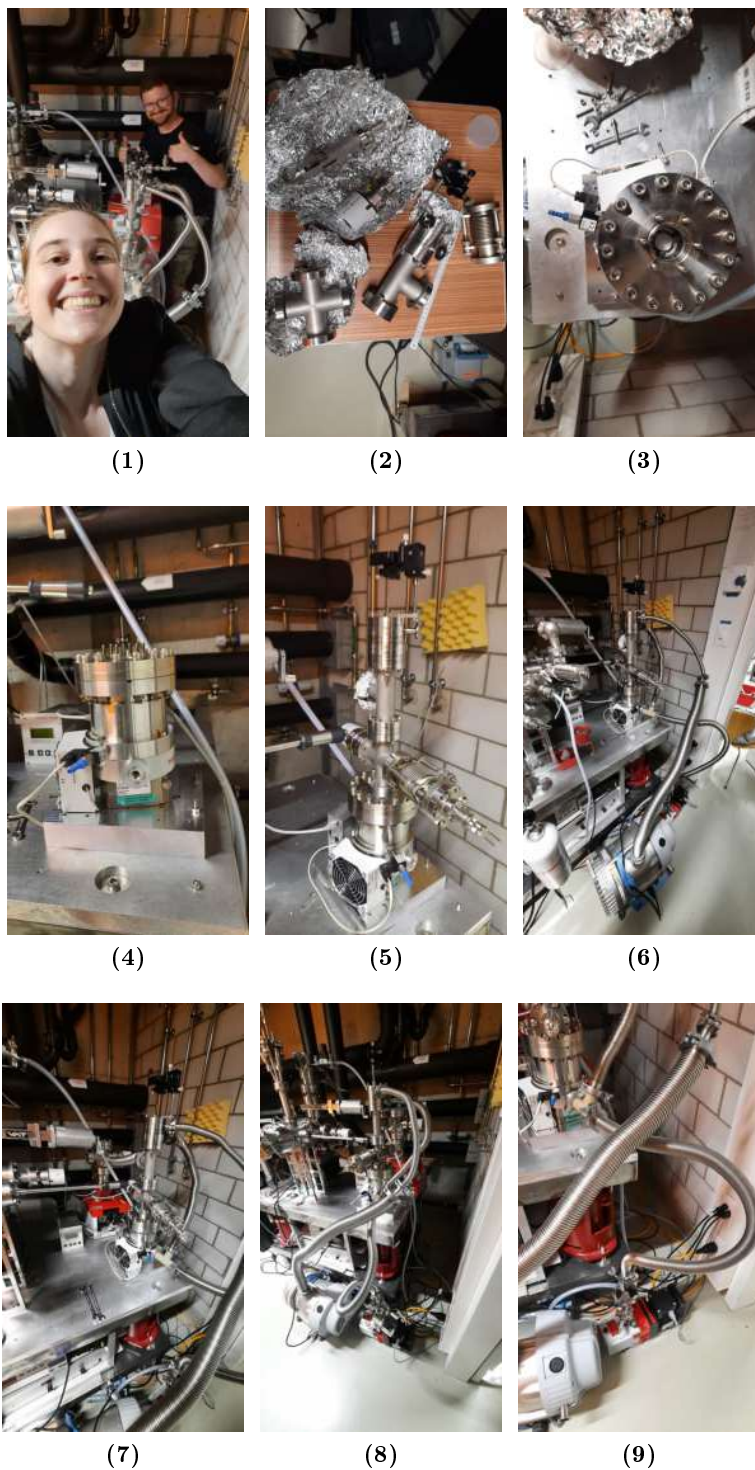
[www.nanopartz.com](http://www.nanopartz.com)

## B.3 Electro spray

To perform STM luminescence measurements we need a plasmonic tip as well as an optical setup to detect photons. To functionalize the tip we will pick up gold nanoparticles (AuNPs) from

HOPG. We planned to deposit AuNPs to HOPG using two methods: dropcasting and with an electro spray. However, building up the electro spray was more involved than anticipated, so we focused mainly on the dropcast technique.

*Figure 78: Summary and impressions of the setup and installation of the electro spray that we intended to commission for AuNP deposition.*



#### B.4 Tip preparation

We used a Platinum/Iridium wire (Pt80/Ir20, 0.25 mm diameter) and cut it in 45 deg (see Figure 79) using sharp pliers. Since we were performing the experiments in air we did not perform electrochemical edching.



*Figure 79: Left: Tip in the tipholder , Right: How we cut the tip.*

## B.5 Optical setup

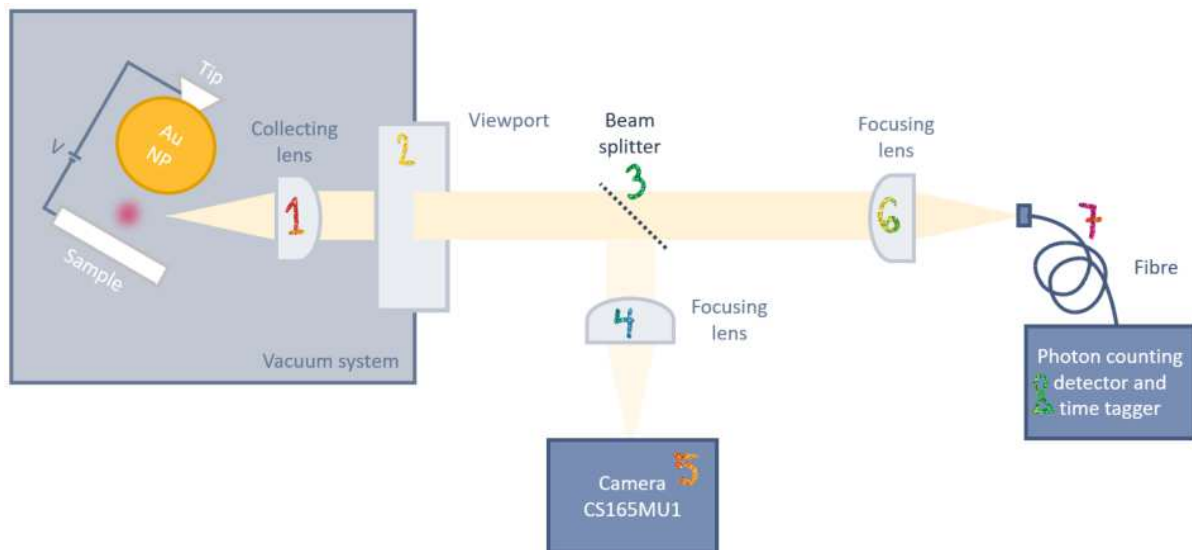


**Figure 80:** Schematic drawing of the optical setup with Numbers. 1: Collecting lens, 2: Viewport, 2: Beam splitter, 4: Focusing lens, 5: Thorlabs Camera, 6: Focusing lens, 7: Fibre, 8: Photon counting detector and time tagger. In Table 7 we listed all the parts we used at a for a number (e.g. 1: collecting lens, Lens holder) in the schematic drawing with their function and product name. In Figure 81 we made a foto table of the parts we used

**Table 7:** List of the parts we used.

Number	Name	Function
1	Thorlabs 355397 Design by Ales	Collecting lens Lens holder
2	Fused Silica Viewport - UV grade Design by Ales Huntington Mechanical Laboratories MPM-275	Viewport with increased transmission of UV and IR wavelengths. Flange adapter for cage system three-axis XYZ manipulator Serial No. 60808
3	Thorlabs DFM1T5 Thorlabs BS028 Thorlabs BS025	beam splitter cage beam splitter used for rough beam adjustment beam splitter for camera feedback
4	Thorlabs LA1509 Thorlabs SM1NR1 Thorlabs CP37	Lens Tube to fix lens Tube holder
5	Thorlabs CS165MU1 Thorlabs SM1T4 Thorlabs CXY1A	1.6 MP Monochrome CMOS Camera Adjustment connection pieces xy-stage
6	Thorlabs AC254-030-AB	Focusing lens
7	Thorlabs M133L02 CXYZ05A	Fibre xyz stage
8		described in section 4.1.6



*Figure 81: Close-up of the optical components used in the optical setup sketched in Figure 80 and summarized in Table 7.*

Overview



View through UV flange



2  
Cage-Flange  
adapter



2  
Cage-Flange  
adapter



6,7  
Lens and  
fibre adapter



1  
Collecting lens  
We used 355397



3  
Beam splitter  
cage



3  
Beam splitter  
cubes



4  
Tube from above



4  
Vision through  
tube



4  
Lens in tube



5  
Thorlabs camera



5  
Thorlabs Cam



5  
Camera and  
to xy stage



5  
Thorlabs and  
stage



3  
Focusing lens



7  
Fibre



7  
Fibre xyz stage



## B.6 Lensholder design

The light coming from the junction needs to be collected and guided out of the vacuum chamber. We needed to fix the lens in the vicinity of the junction. Before we ended up with the final design described in Figure 50 we tried a construction with tubes designed by Ales. At the end of the tube there was the possibility to fix the lens. In Figure 79 we see how we tried to fix the tubes in the head. We struggled with the alignment of the tube and realized that the cutout in the STM head were at an angle not aligned with the viewports which made the installation cumbersome. This design was also not easily adaptable to another STM since it was constructed for the geometry of the VTSTM.



*Figure 78: These are the Tube-Lens holder designed by Ales.*

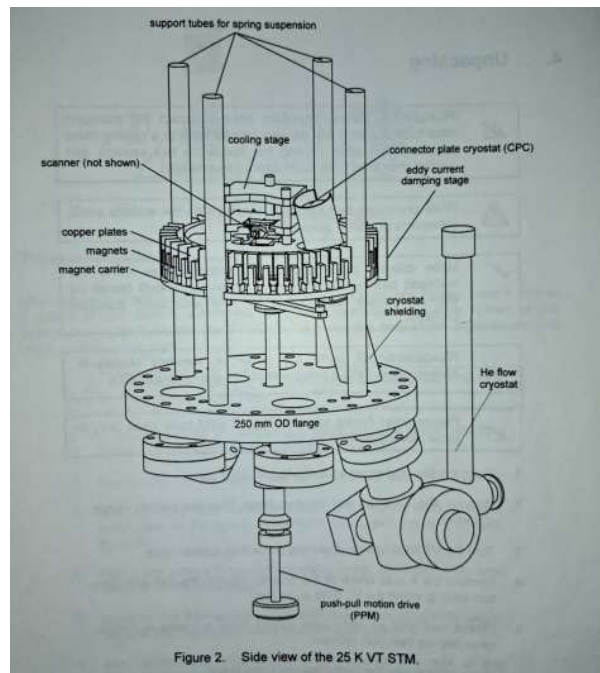


Figure 2. Side view of the 25 K VT STM.

*Figure 79: This is a page from the manual with a schematic drawing of the head. With orange we marked how the tube was hanging in the head. To access the tube and change its direction we fixed a wire (blue) in the head.*

## B.7 Calibration of the VTSPM

I learned how to use VTSTM. Since the displacement of the scanner piezo in the x,y and z directions does not have a one-to-one correspondence with the applied voltage we calibrated the x, y and z channels of the scanner piezo using a sample of highly oriented pyrolytic graphite (HOPG) in a vacuum of  $\approx 10^{-7}$  bar.

### B.7.1 xy direction

In Figure 80 we see the STM picture of atomically resolved HOPG edited in Gwyddion (left) and the corresponding extracted lineprofiles (right). The maxima and minima in the lineprofile show individual atoms from which the lattice spacing can be measured.

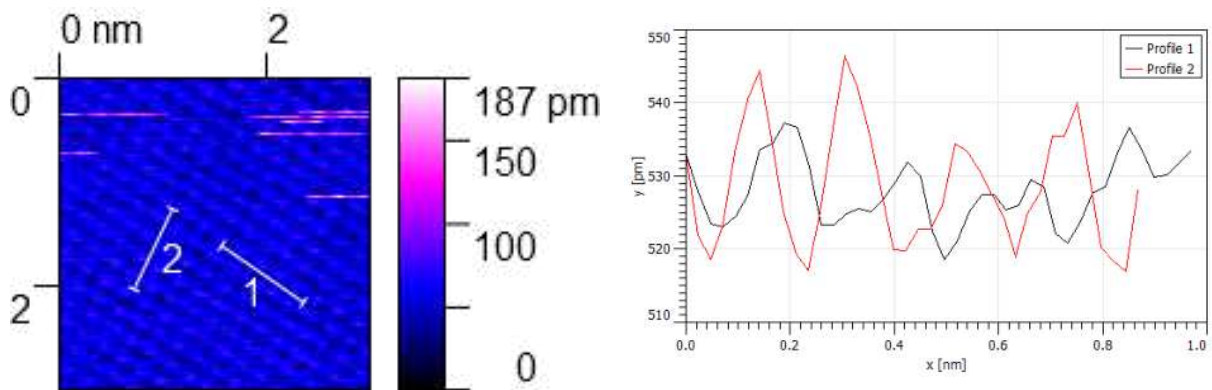


**Figure 80:** Left: STM picture of atomically resolved HOPG used for xy calibration, Right: corresponding line profiles. The maxima and minima show individual atoms from which the lattice spacing can be measured.

We extracted the minimal values from the lineprofile one (see Figure 81) and two (see Figure 82). We marked the middle of the pits. The corresponding values are on the right.

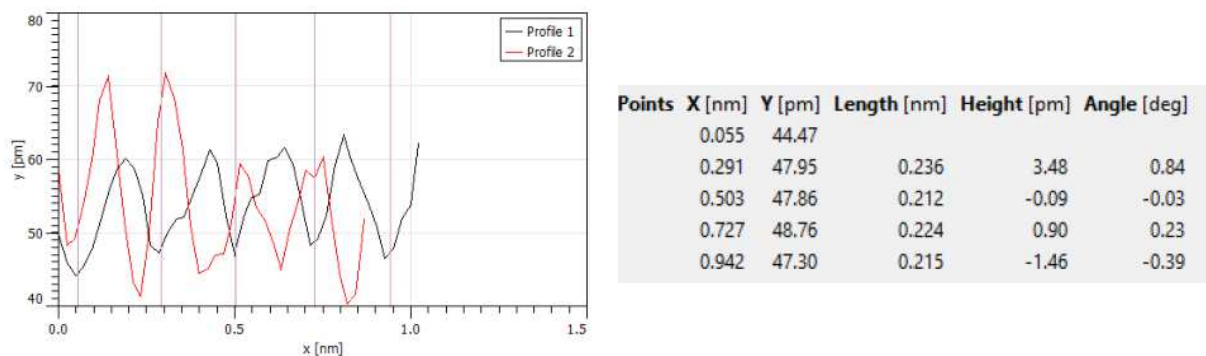


**Figure 81:** Values for xy calibration.

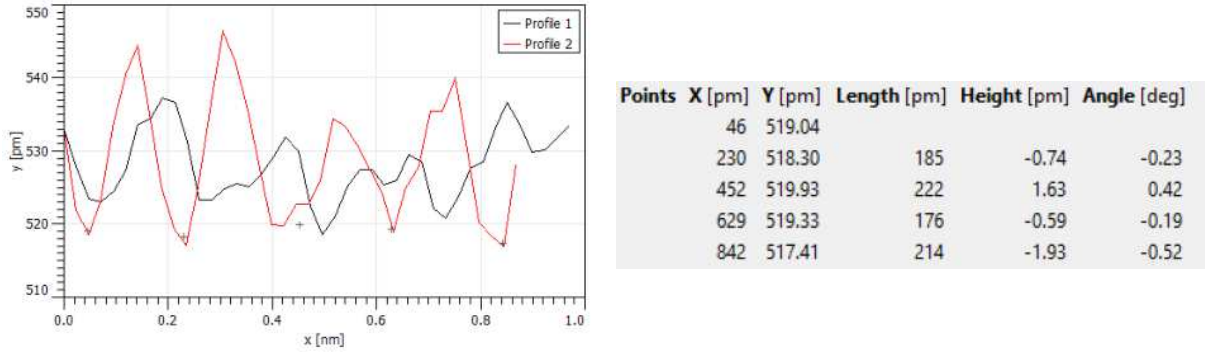


**Figure 82:** Values for  $xy$  calibration.

We take an average over the collected distances.

$$\begin{aligned} \text{avg1} &= \frac{942 \text{ pm} - 55 \text{ pm}}{4} = 222 \text{ pm} \\ \text{avg2} &= \frac{842 \text{ pm} - 46 \text{ pm}}{4} = 199 \text{ pm} \end{aligned} \quad (\text{B.1})$$

The two different values are caused by thermal drift that influences the slow scan direction ( $y$ ) more than the fast scan direction ( $x$ ). Therefore we took 222 pm to find the conversion factor  $\frac{222 \text{ pm}}{246 \text{ pm}} = \mathbf{0.9}$  (from measured to "real" value). This scaling factor needs to be applied to all topographic data to scale it to the proper height information.

### B.7.2 $z$ direction

We chose Figure 83 to calibrate the  $z$  direction. We had some problems with the leveling. Therefore we chose two options (left and right) and then compared the results.

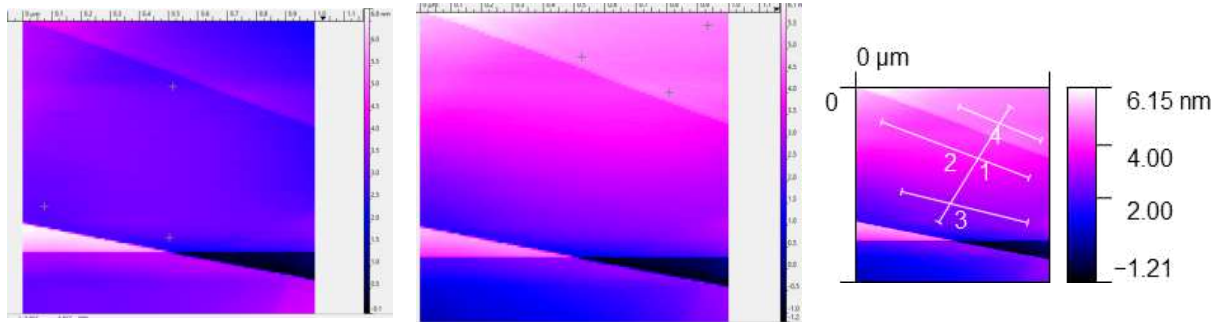


**Figure 83:** Left and middle: STM measurements showing several graphite step edges used for the  $z$  calibration. We chose two leveling options and then compared the results of option 1 (left) and option 2 (middle).

The profiles from Figure 83 on the right were used to extract the lineprofiles from Figure 84 to extract the data in Figure 85.



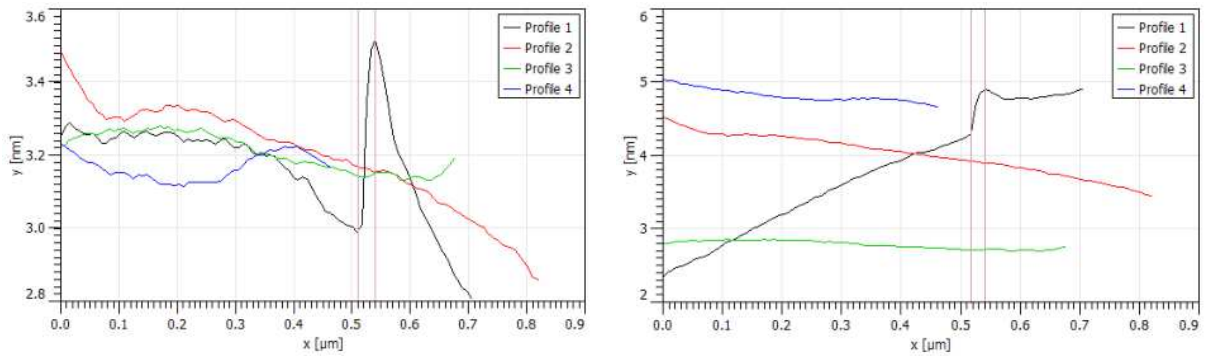


**Figure 84:** Option 1 lead to the lineprofile in the middle and the level option 2 to the profile on the right as described in Figure 83.

Points	X [nm]	Y [pm]	Length [nm]	Height [pm]	Angle [deg]
	510	2994			
	540	3517	30	523	1.01

Points	X [nm]	Y [nm]	Length [nm]	Height [nm]	Angle [deg]
	517	4.316			
	541	4.908	24	0.592	1.44

**Figure 85:** Data extracted from Figure 84.

From the leveling Option 1 we have a stepheight of  $3517 \text{ pm} - 2994 \text{ pm} = 523 \text{ pm}$  for the distance of 30 nm (see Figure 85).

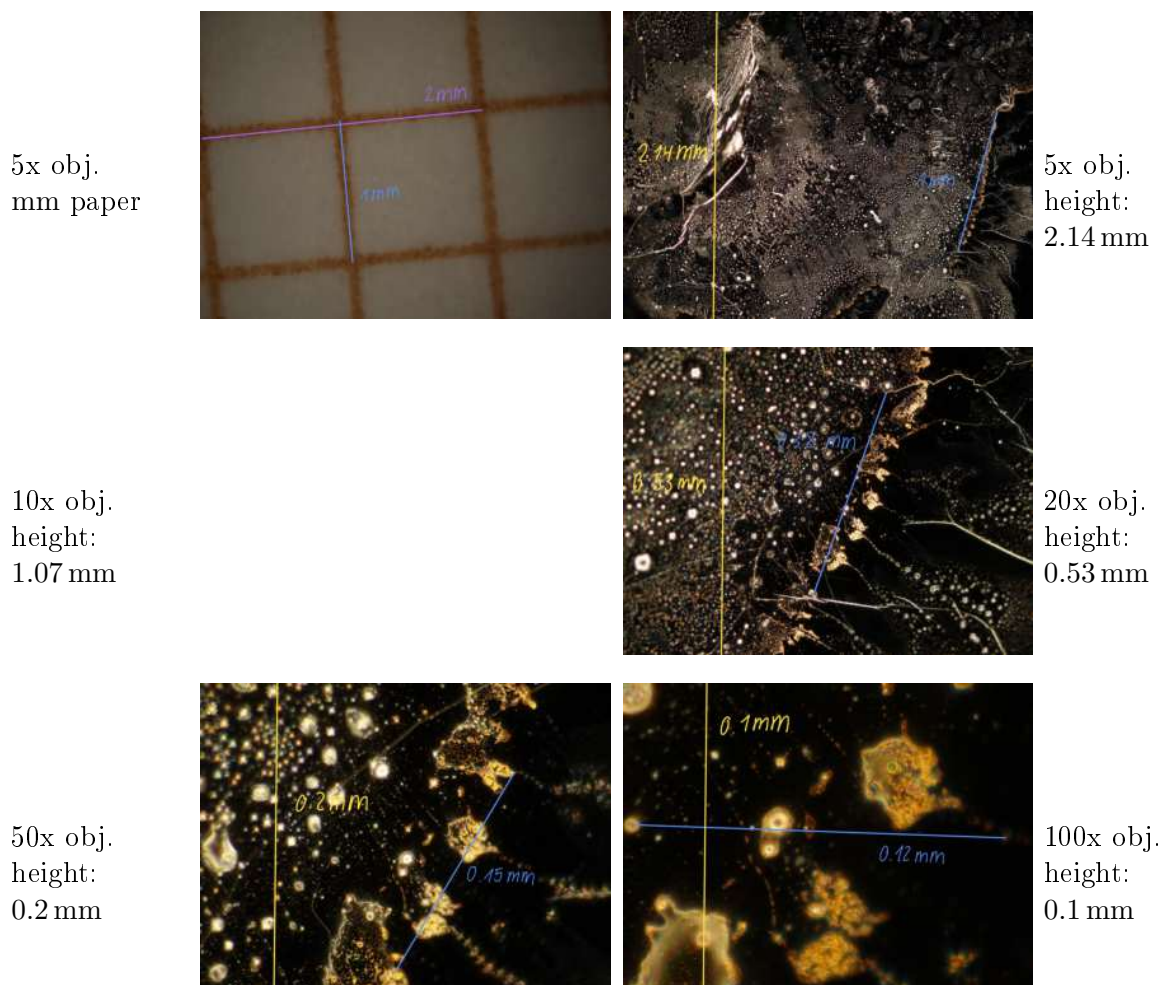
From the leveling Option 2 we have a stepfall of  $4.316 \text{ nm} - 4.908 \text{ nm} = 592 \text{ pm}$  for the distance of 24 nm (see Figure 85).

The separation between two graphene sheets in graphite is  $3.35 \text{ \AA} = 335 \text{ pm}$ , as shown in Figure 58. If we take the average of the two leveling methods we get 557 pm as a step height. The from measured to "real" value is  $\frac{557 \text{ pm}}{335 \text{ pm}} = 1.66$ . This scaling factor needs to be applied to all topographic data to scale it to the proper height information.

### B.8 Scaling of the BX41M light microscope

In Figure 86 we have a picture of a mm paper on the top left taken with the 5x objective. In the manual of the microscope we learned that the 10x has the double magnification of the 5x and so on. We verify this in Figure 86 and find a the corresponding height of the fotos.

**Figure 86:** Verification of the size of the pictures taken with the light microscope Olympus BX41M and the corresponding objectives (obj.).



## Appendix C Results

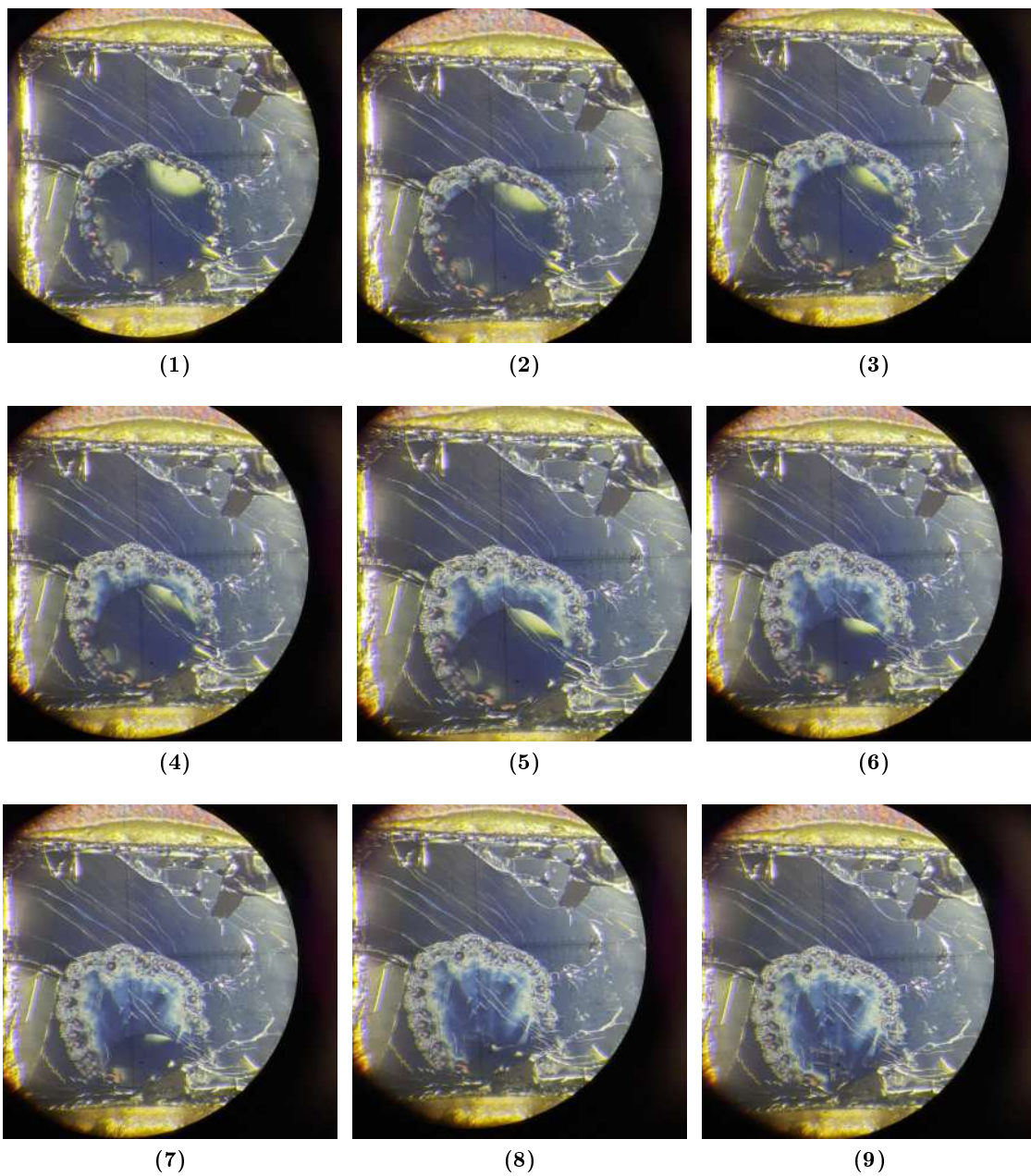
### C.1 Dropcast method

To perform STM luminescence measurements we need a plasmonic tip as well as an optical setup to detect photons. To functionalize the tip we will pick up gold nanoparticles (AuNPs) from HOPG. We planned to deposit AuNPs to HOPG using two methods: dropcasting and with an electro spray. For the dropcast experiments, after applying the first drops of AuNPs onto HOPG and observing their circular staining patterns as they dried, we inserted the samples into the AFM for further investigations.

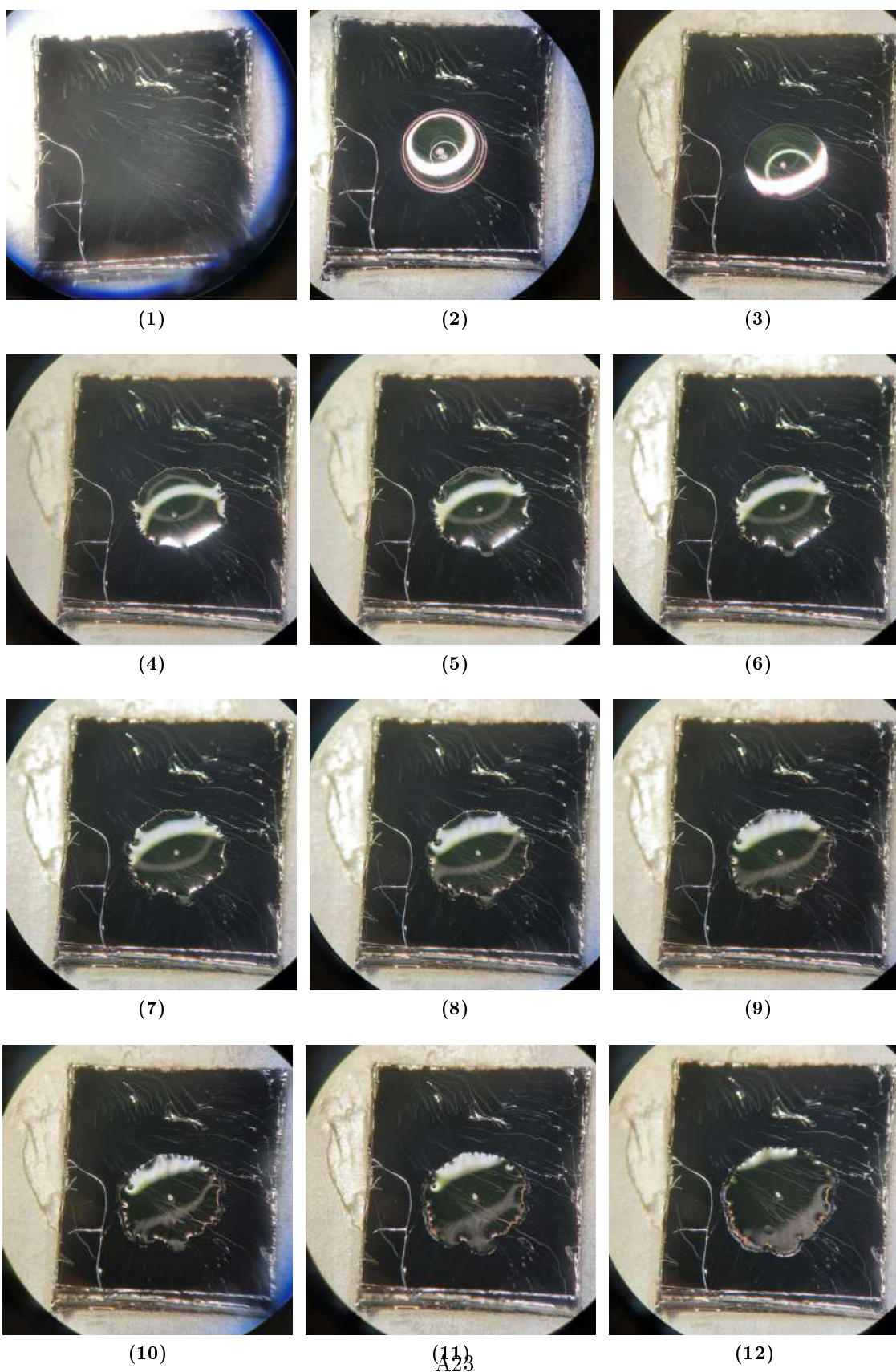


### C.1.1 Drying drops

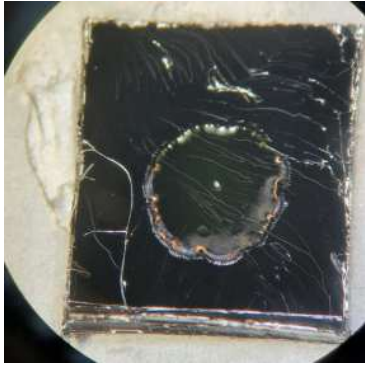
*Figure 87: Time lapse of the drying process (air, room temperature) from the dropcasted 1  $\mu\text{L}$  gold nanoparticle solution (OD1) onto HOPG. The HOPG crystal is  $\approx 4\text{mm}$  and the circular area of the dried drop has a diameter of  $\approx 2\text{mm}$ .*



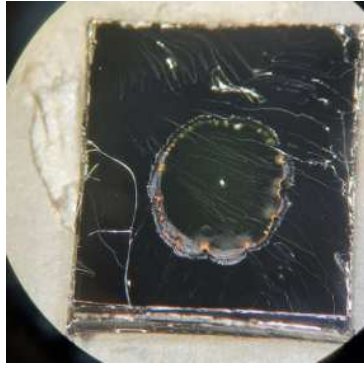
**Figure 88:** Time lapse of the drying process (air, room temperature) from the 1  $\mu$ L dropcasted gold nanoparticle solution (OD1) onto HOPG. The HOPG crystal is  $\approx$  4 mm and the circular are of the dried drop has a diameter of  $\approx$  1.5 mm.



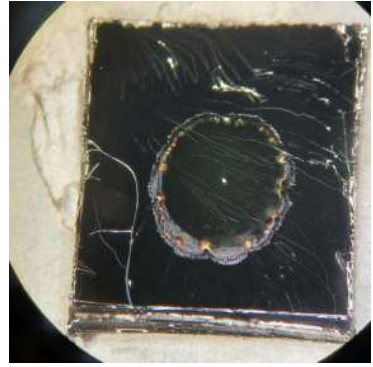




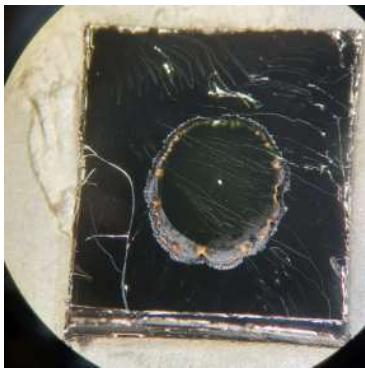
(13)



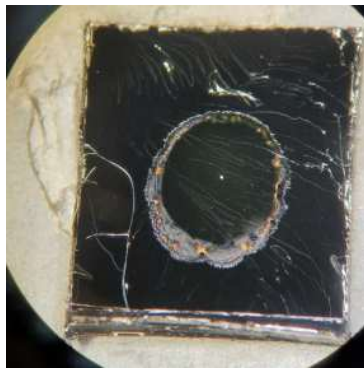
(14)



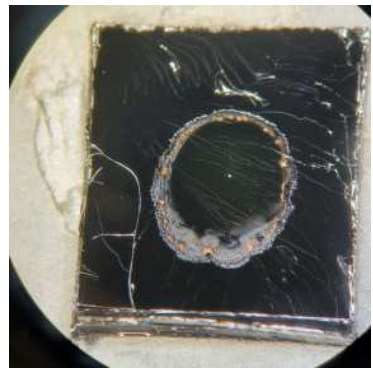
(15)



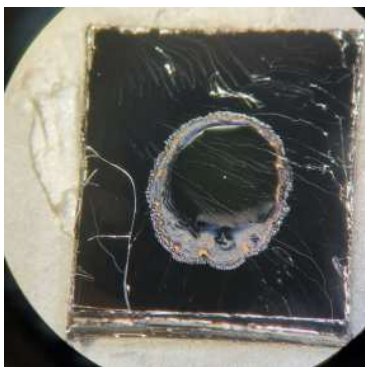
(16)



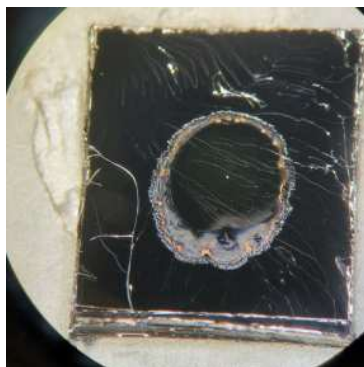
(17)



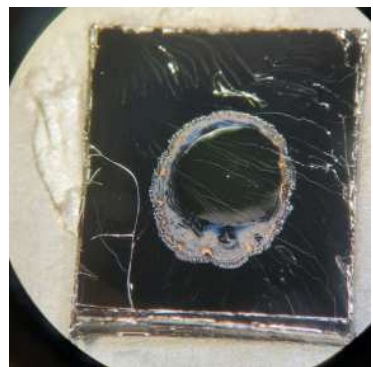
(18)



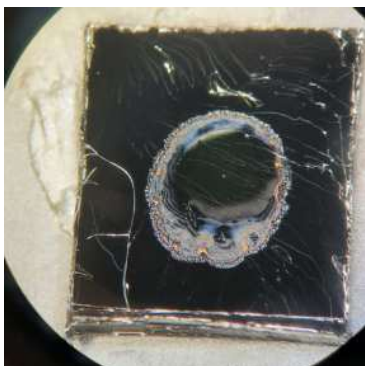
(19)



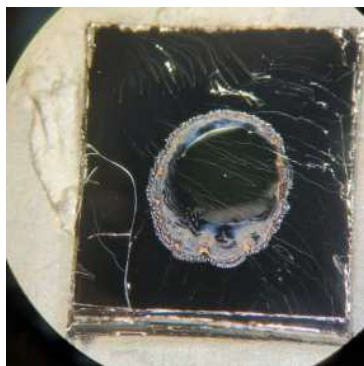
(20)



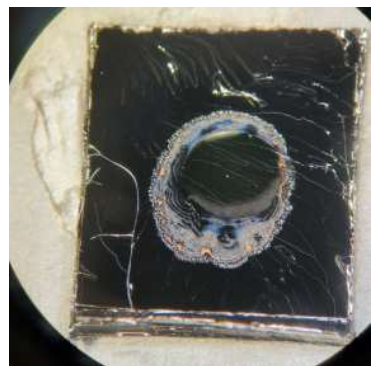
(21)



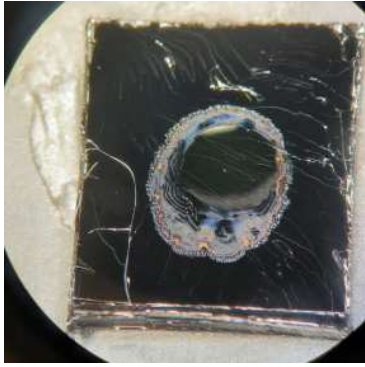
(22)



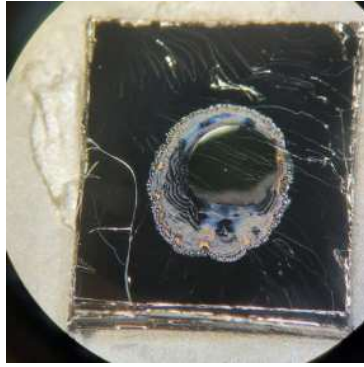
(23)



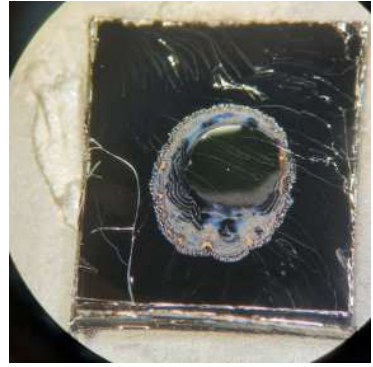
(24)



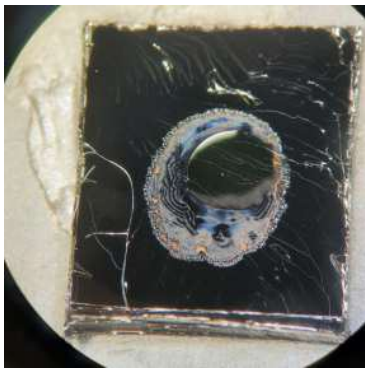
(25)



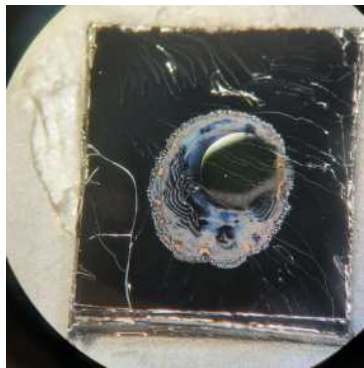
(26)



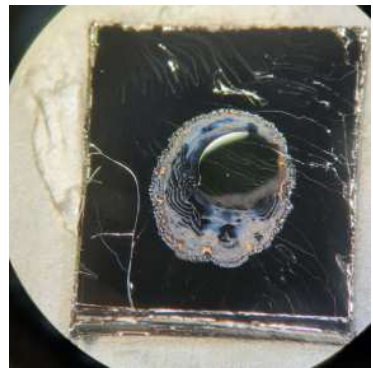
(27)



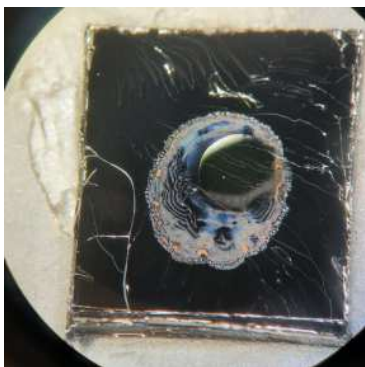
(28)



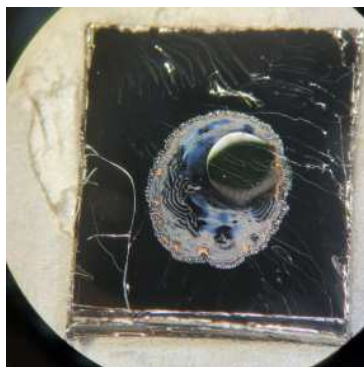
(29)



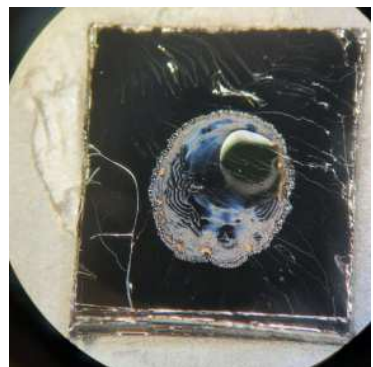
(30)



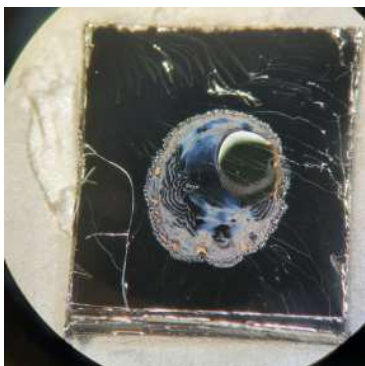
(31)



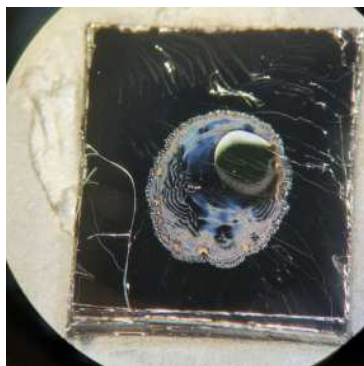
(32)



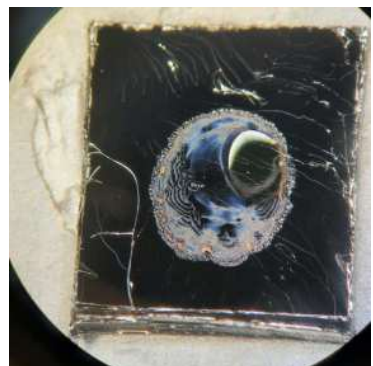
(33)



(34)

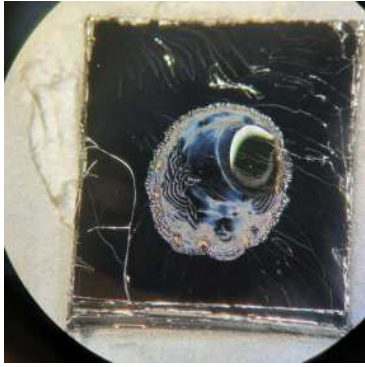


(35)

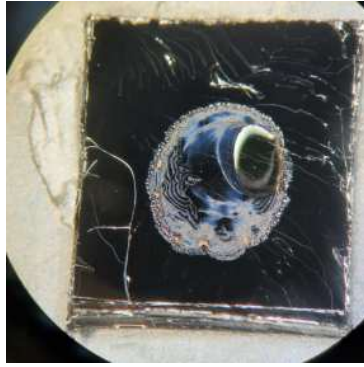


(36)

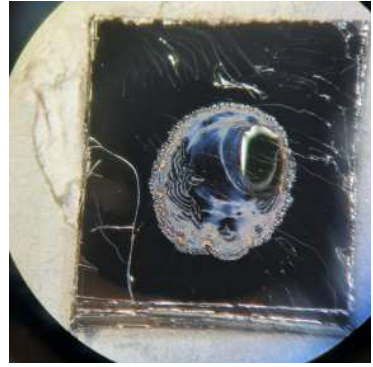




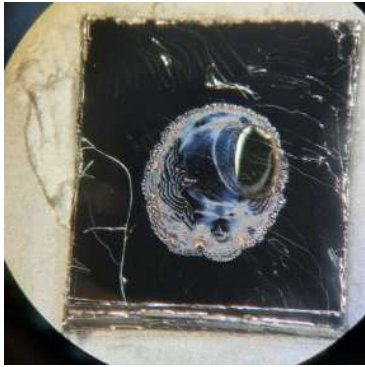
(37)



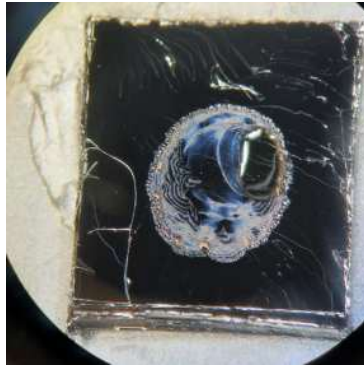
(38)



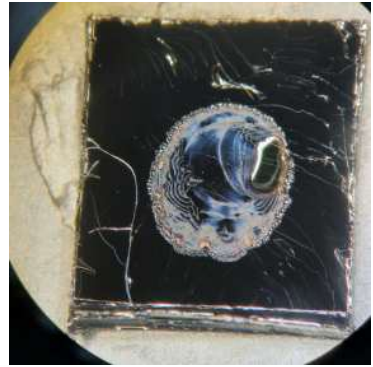
(39)



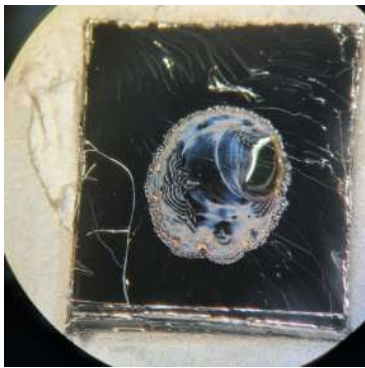
(40)



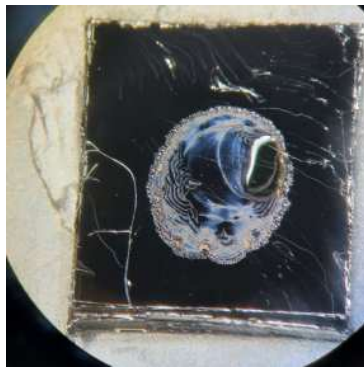
(41)



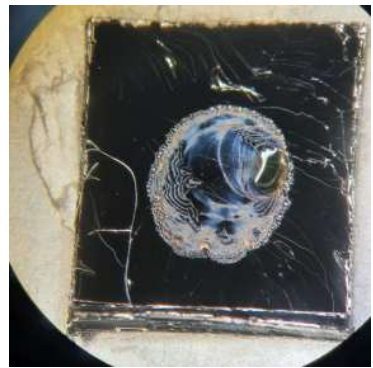
(42)



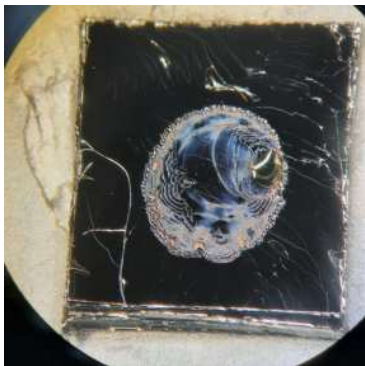
(43)



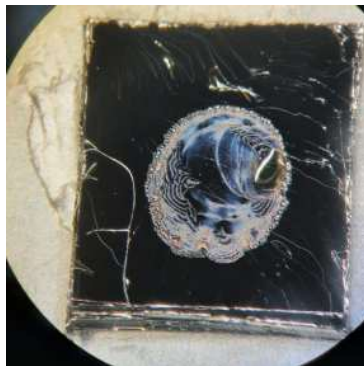
(44)



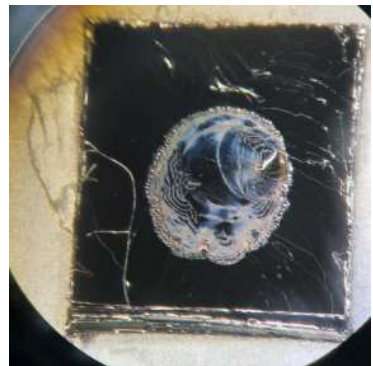
(45)



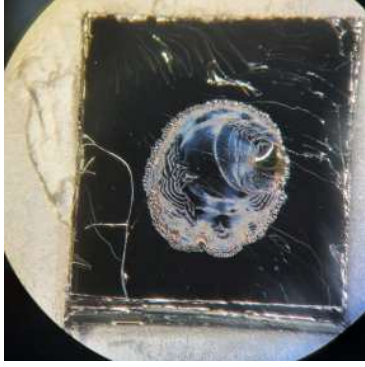
(46)



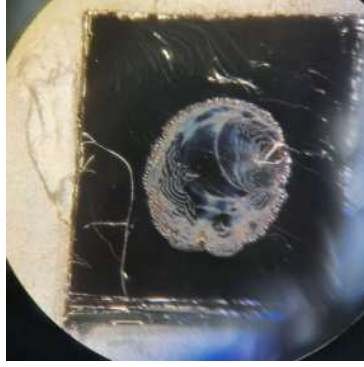
(47)



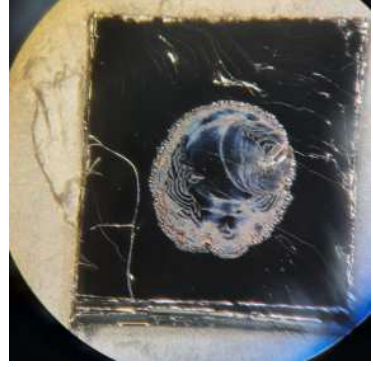
(48)



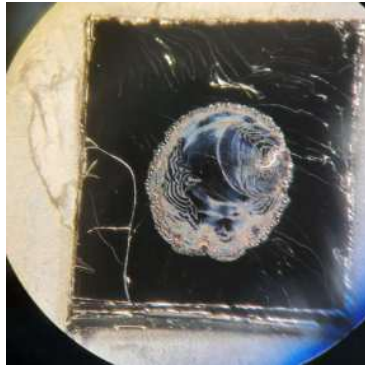
(49)



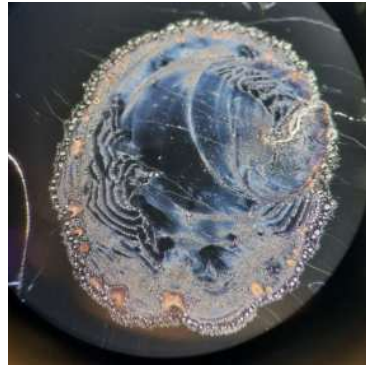
(50)



(51)



(52)



(53)

**Figure 85:** Dropcasted gold nanoparticle solution (OD1, air, room temperature) onto HOPG taken with the light microscope BX41M. On the left we listed the used objective with their corresponding magnification. In the 100x magnitude we see that liquid is surrounding the particle clusters.

DF mode  
Objective 5x  
height:  
2.4 mm



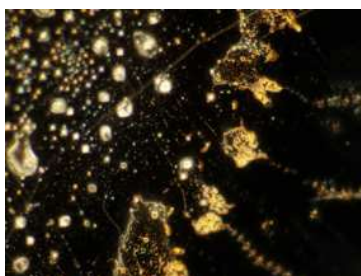
(1)

DF mode  
Objective 20x  
height:  
0.53 mm



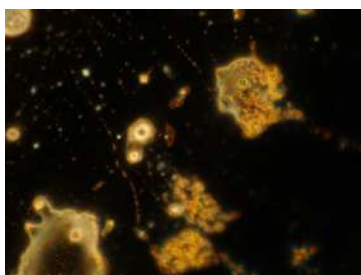
(2)

DF mode  
Objective 50x  
height:  
0.2 mm



(3)

DF mode  
Objective 100x  
height:  
0.1 mm



(4)

0.90 BF mode  
Objective 100x  
height:  
0.1 mm



A28

(5)




### C.1.2 Increase AuNP density

From our AFM measurements we concluded that we do not have enough particle density to perform STM measurements. The scan range of our STM is with  $1 \times 1 \mu\text{m}^2$  smaller than the scan range in the AFM ( $10 \times 10 \mu\text{m}^2$ ). To successfully detect particles, the scan range of the STM should have at least 10 to 100 particles.

#### C.1.2.1 Heating

**C.1.2.1.1 Increase optical density of the AuNP solution.** To increase the density of the particles we tried to evaporate the buffer solution.

*Table 8: We used the drying oven to get rid of the water in my buffer solution.*

Time [min]	What happend	Photo
00.00	Ofen reached 100°	
01.40	Ofen reached 110°	
13.42	We saw bubbles in the liquid but it was never visibly boiling.	
60.00		
89.25	We took it out	

We pipetted twice  $2 \mu\text{L}$  on two separate HOPG but the Liquid seemed dirty. There were black particles in it.



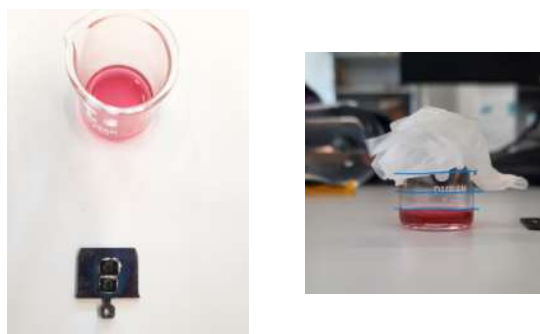


*Figure 86: We see that we lost approximately two thirds of the liquid.*

**C.1.2.1.2 Make smaller drops** During the drying processes we observed that the drop-casted solution spread from  $\approx 1$  mm to  $\approx 2$  mm. Probably dropcasting on heated HOPG will produce smaller dried drops leading to higher density.

**Figure 87:** We compare heated (120° for 20 min) and not heated samples. Right column: dropcast OD1 AuNP solution on room temperature HOPG, left column: dropcast OD1 AuNP solution on heated HOPG.

DF mode  
Objective 5x  
height:  
2.4 mm



(1)

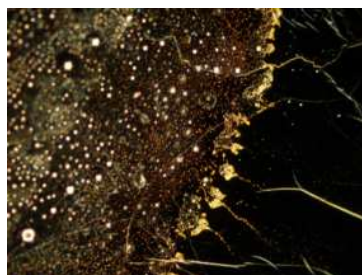


(2)

DF mode  
Objective 20x  
height:  
0.53 mm



(3)

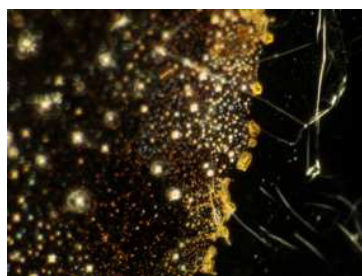


(4)

DF mode  
Objective 50x  
height:  
0.2 mm



(5)

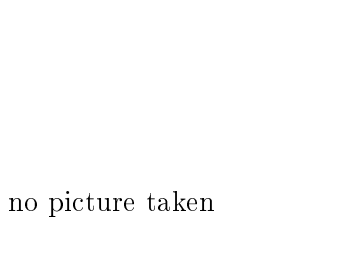


(6)

DF mode  
Objective 100x  
height:  
0.1 mm



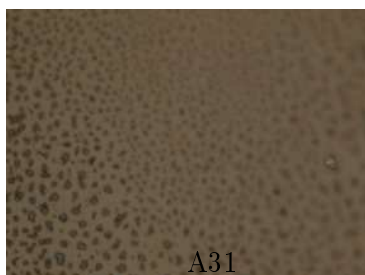
(7)



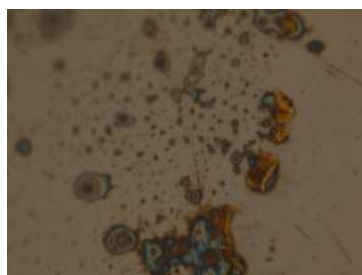
no picture taken

(8)

0.90 BF mode  
Objective 100x  
height:  
0.1 mm



(9)



(10)

A31

**Figure 88:** We compare heated ( $150^{\circ}$  for 15 min) and not heated samples. Right column: dropcast OD1 AuNP solution on room temperature HOPG, left column: dropcast OD1 AuNP solution on heated HOPG. The scaling of the photos are the same as in Figure 87. We saw that the drop dried faster but there was still a lot of water left around the particles. We zoomed in some interesting structures and realized, that the cluster distribution could be connected with waterdroplets (bottom right).

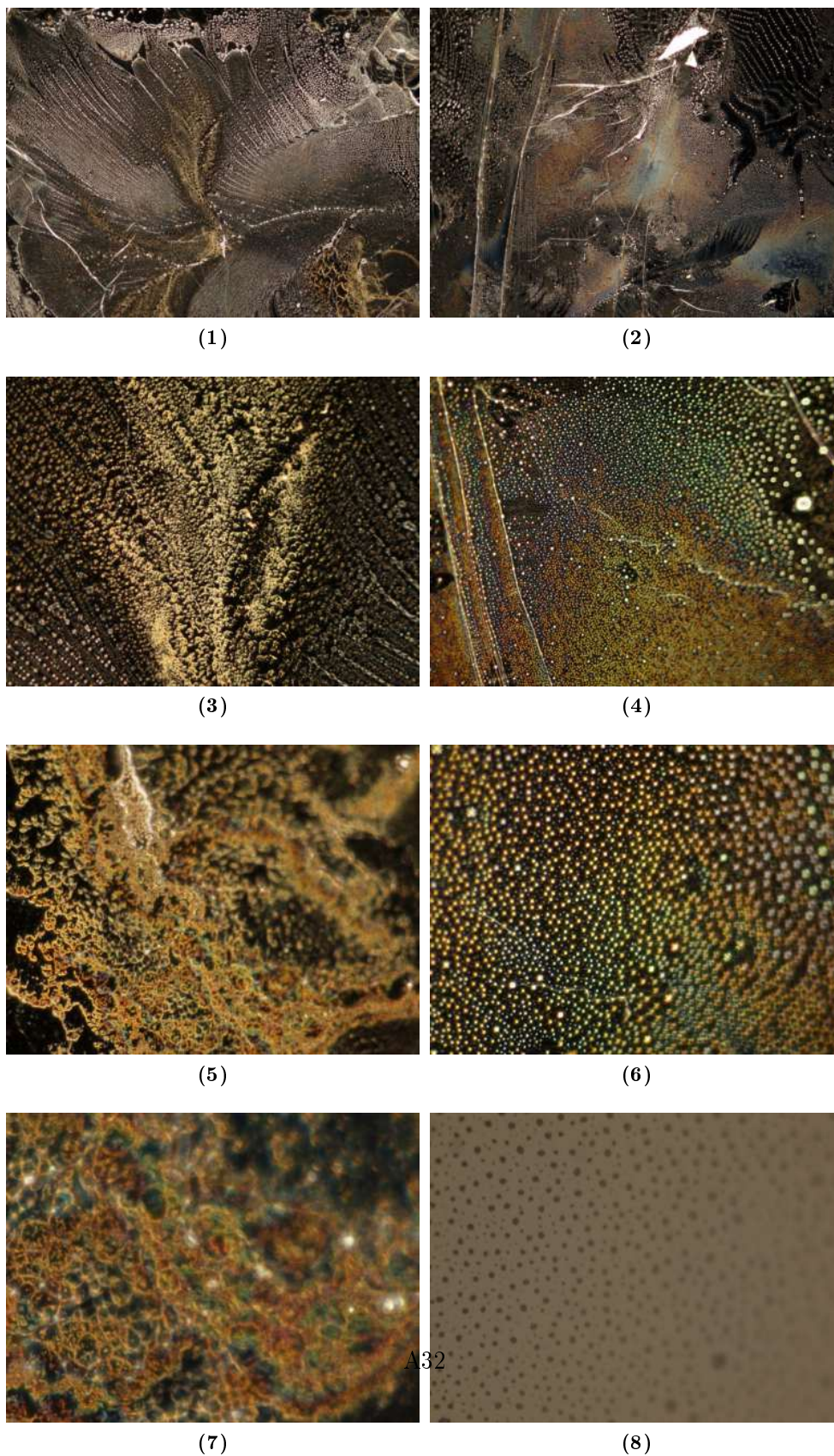
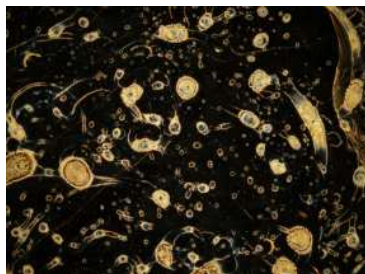




**Figure 89:** We compare heated (200° for 20 min) and not heated samples. Right column: dropcast OD1 AuNP solution on room temperature HOPG, left column: dropcast OD1 AuNP solution on heated HOPG. The solution splashed around when we dropcasted it. This process is too random to make use of it.

DF mode  
Objective 5x  
height:  
2.4 mm

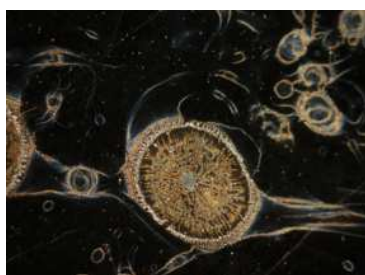


(1)



(2)

DF mode  
Objective 20x  
height:  
0.53 mm

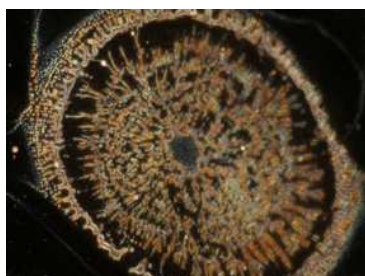


(3)

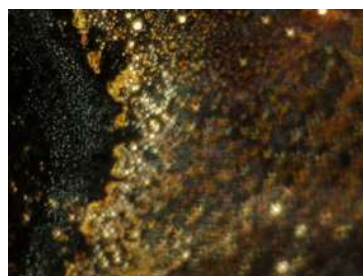


(4)

DF mode  
Objective 50x  
height:  
0.2 mm

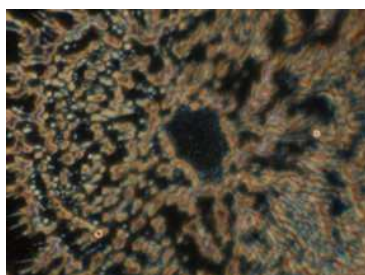


(5)

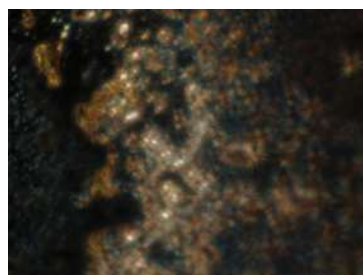


(6)

DF mode  
Objective 100x  
height:  
0.1 mm



(7)



(8)

0.90 BF mode  
Objective 100x  
height:  
0.1 mm



(9)

no picture taken

(10)

**Figure 90:** We compare heated (300° for 20 min) and not heated samples. Right column: dropcast OD1 AuNP solution on room temperature HOPG, left column: dropcast OD1 AuNP solution on heated HOPG. We see in the left column that the usual color of the golden shimmer went darker. We guess that we changed something in the structure of the AuNPs.

DF mode  
Objective 5x  
height:  
2.4 mm



(1)

(2)

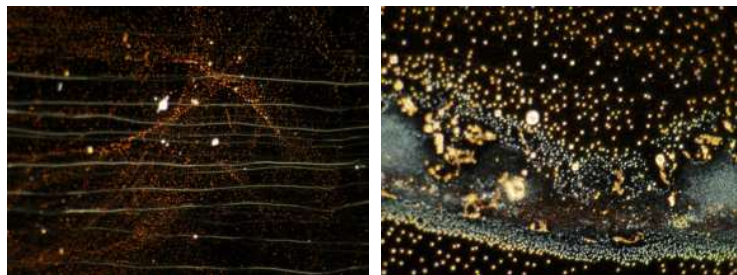
DF mode  
Objective 20x  
height:  
0.53 mm



(3)

(4)

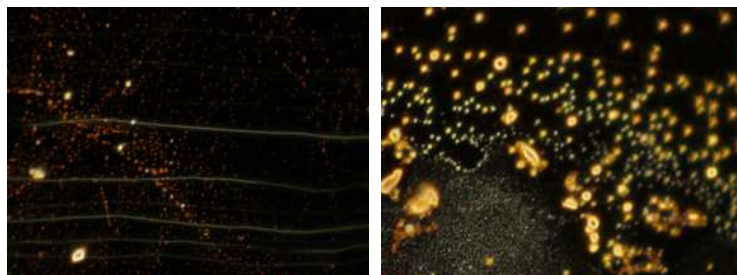
DF mode  
Objective 50x  
height:  
0.2 mm



(5)

(6)

DF mode  
Objective 100x  
height:  
0.1 mm



(7)

(8)

0.90 BF mode  
Objective 100x  
height:  
0.1 mm



(9)

(10)

**Figure 91:** With silver glue we made small circles on HOPG and performed dropcast of 1  $\mu$ L in each circle.

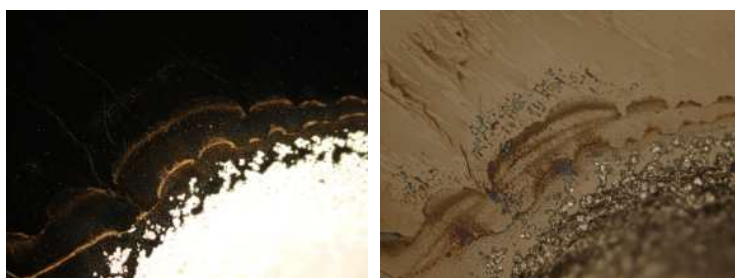
Objective 5x  
 left: DF mode  
 right: 0.15 BF mode  
 height:  
 2.4 mm



(1)

(2)

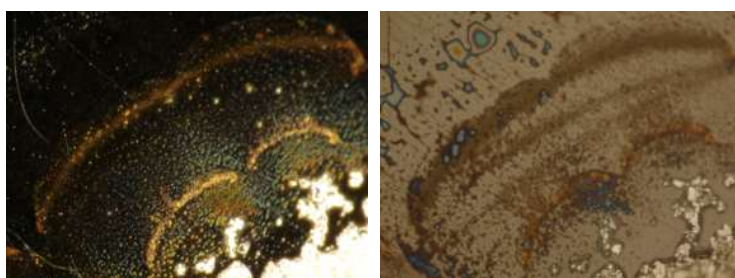
Objective 20x  
 left: DF mode  
 right: 0.46 BF mode  
 height:  
 0.53 mm



(3)

(4)

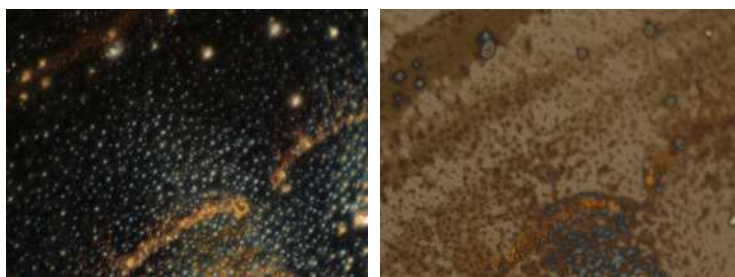
Objective 50x  
 left: DF mode  
 right: 0.80 BF mode  
 height:  
 0.2 mm



(5)

(6)

Objective 100x  
 left: DF mode  
 right: 0.90 BF mode  
 height:  
 0.1 mm



(7)

(8)



**Figure 92:** With silver glue we made small circles on HOPG and performed dropcast of 1  $\mu\text{L}$  in each circle. Additionally we heated the sample afterwards with 300° for 20 min.

DF mode  
Objective 5x  
height:  
2.4 mm



(1)



(2)

DF mode  
Objective 20x  
height:  
0.53 mm



(3)



(4)

DF mode  
Objective 50x  
height:  
0.2 mm



(5)

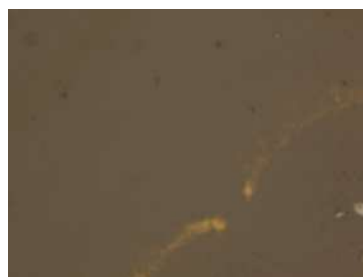


(6)

DF mode  
Objective 100x  
height:  
0.1 mm



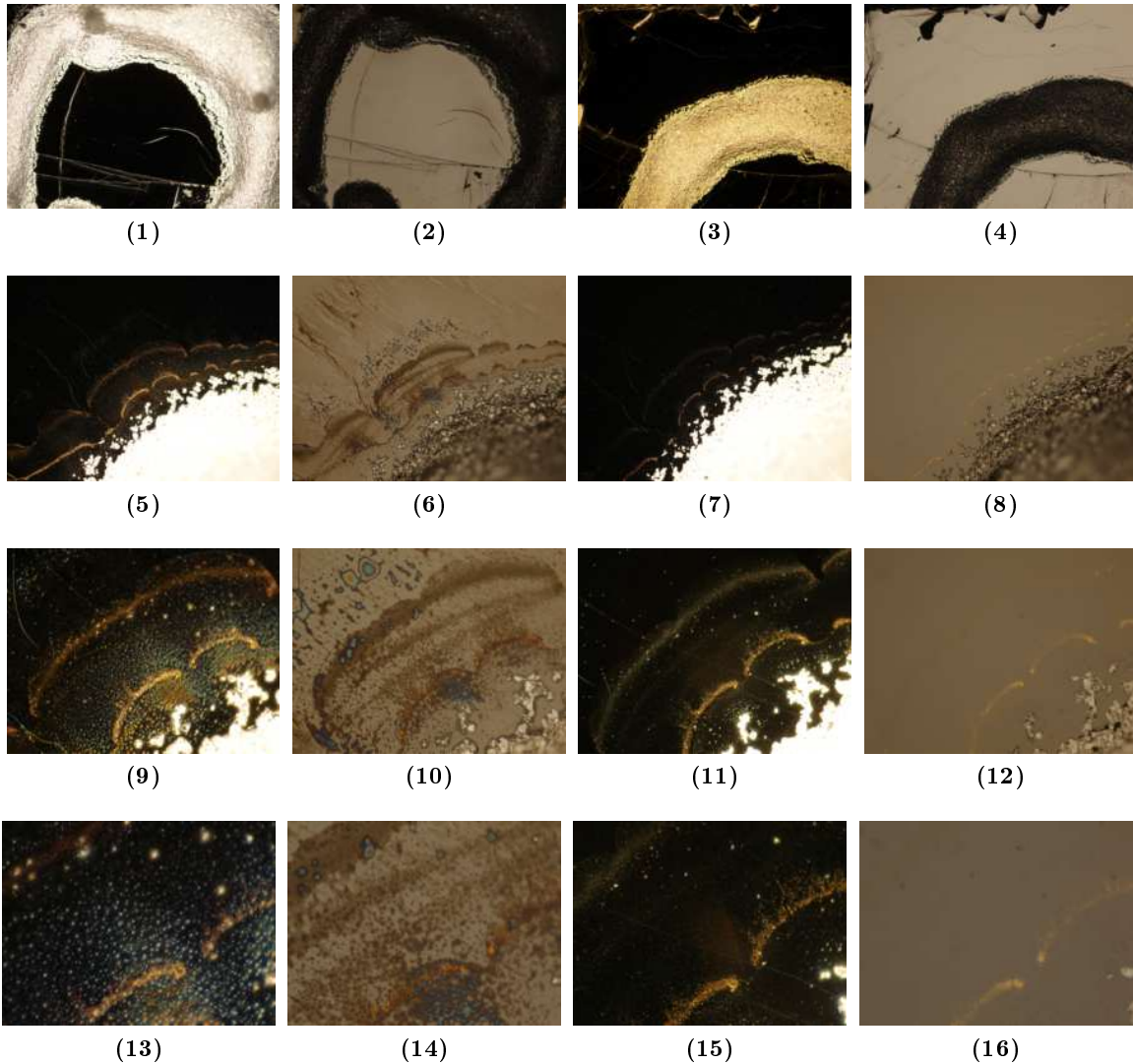
(7)



(8)

**Figure 93:** To see the effect of heating to 300° we compare Figure 91 and 92.

Not heated, DF      Not heated, BF      Heated 300° , DF      Heated 300° , BF



### C.1.2.2 Dropcast several drops in a area limited by silver glue

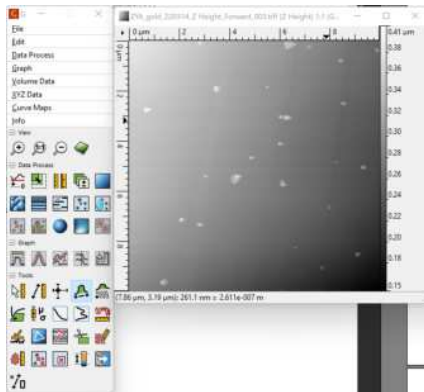
## C.2 AFM measurements

### C.2.1 Gwyddion 2.6

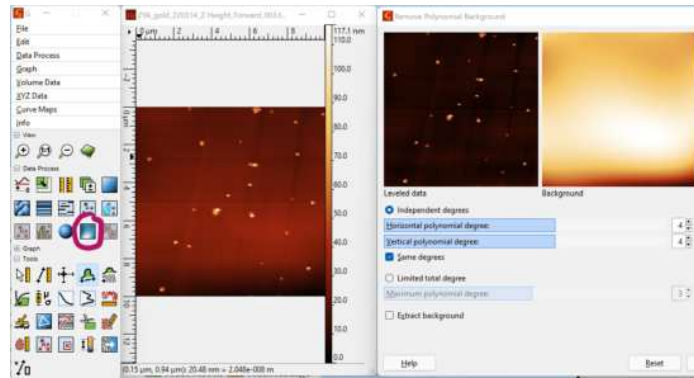
We documented the steps we performed to modify the raw data from the scanning probe micrographs in Figure 94. In Figure 94.(1) We imported the data. In Figure 94.(2) We changed to the color palette Caribbean. Afterwards we pressed "Level data by mean plane subtraction" and the gradient also visible in Figure 103 flattened out (see Figure94.(3)). With "shift minimum data value to zero" we got the result visible in Figure94.(3). As a next step we pressed "remove polynomial background" (see Figure94.(4)) and afterwards the dots were better visible. In the end (see Figure94.(5),(6) and (7)) we pressed the button "stretch color range to part of data". In (6) we see better the structure of the Graphite sample. But since we are not interested in the background we chose (7) to have a better visualisation of the clusters.



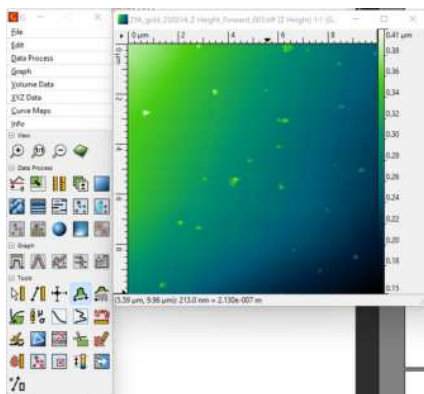
**Figure 94:** Documentation of image processing steps for the AFM scans of AuNP on HOPG. Description of the steps in is the text above.



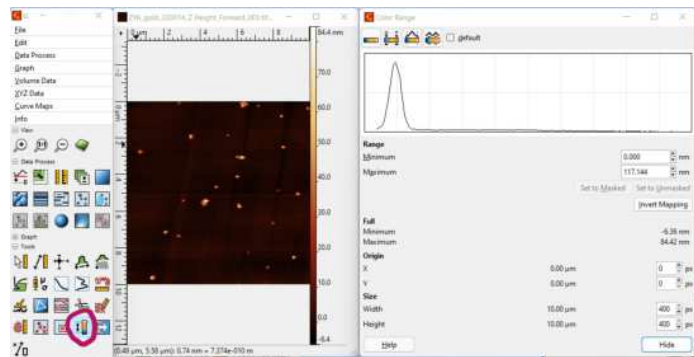
(1)



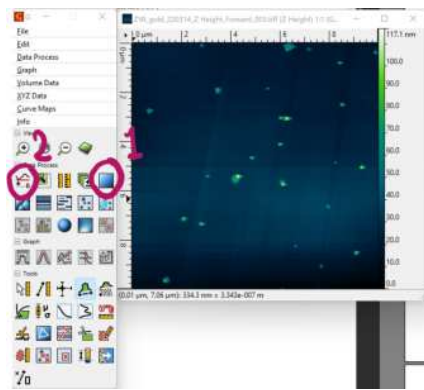
(4)



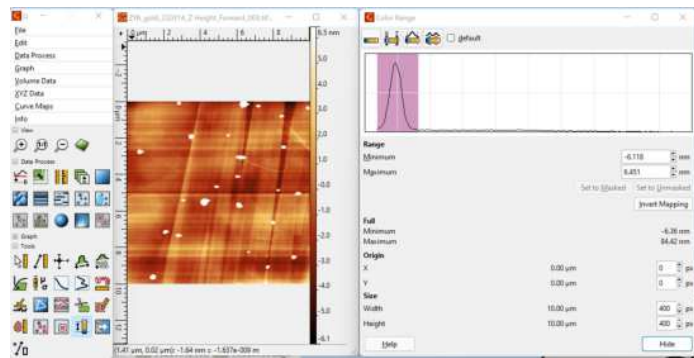
(2)



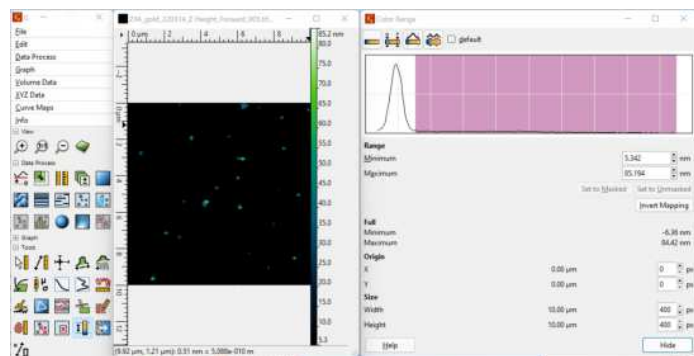
(5)



(3)



(6)



(7)

### C.2.2 ZYA

In Figure 96 we see some pictures taken with the built in camera of the AFM. We can already macroscopically see that the gold particles build clusters such that we can see them with a camera.

In Figure 95 we see a photo taken through the ocular from a light microscope. We see that we applied two drops and that I marked the orientation of the sampleholder with a drawing of the neck. With silver glue we marked some interesting parts to have a better orientation in the AFM. We marked the approximate measurement positions with red numbers.

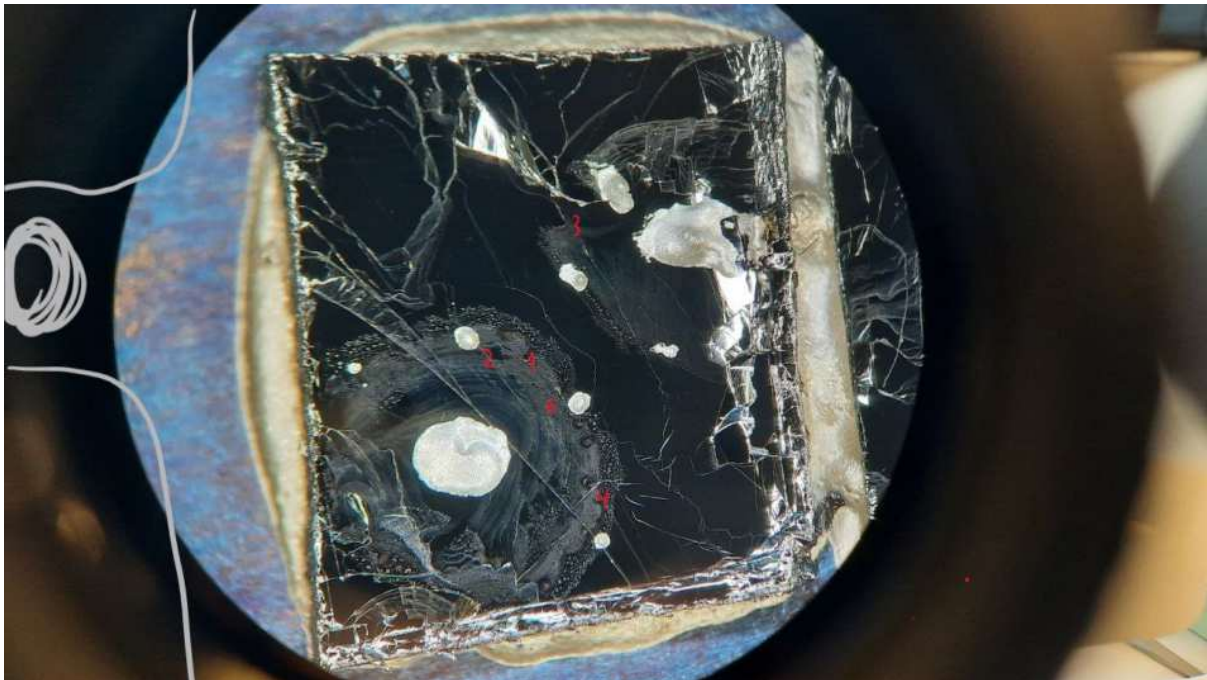


**Figure 95:** Photo of HOPG ZYA with two drops of AuNP solution OD1. The numbers mark the positions of the measurements in Figures 98, 99, 100,101 and 102.

(1) Was just a first random first approach. We saw a golden shimmer in the AFM camera and started to approaching. (2) Was interesting to check how the particles arranged in a crack of the HOPG. (3) Here we saw an interesting s shaped structure. There were several golden clusters of different sizes we wanted to approach. (see middle of Figure 96). (4) Here we saw a darker structure we were interessted in (see Figure 97 on the left). (5) We forgot where this position was. The AFM measurements of those positions are visible in Figures 98 to 102 (6) At this position we saw an interesting black structure we wanted to look at.

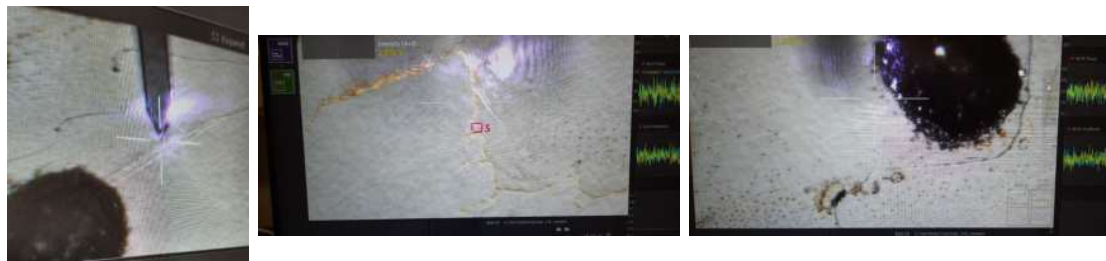


**Figure 96:** Photos of the AFM camera view.

In Figure 96 we see that we can recognize macroscopically golden looking structures. On the left and middle picture we see that the gold particles rolled in a crack of the HOPG structure coming from cleaving. The big black dots are silver glue which allowed me to verify the orientation on the sample. In the right picture we see smaller darker dots.

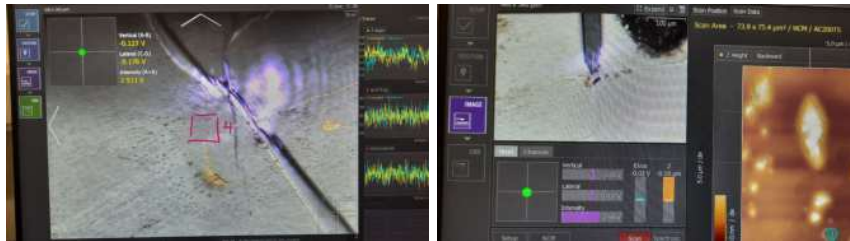


**Figure 97:** Marked positions of the measurement (4) on the left and the tip position for measurement (6) on the right.

With the AFM we were able to look at a field of view of the size 10  $\mu\text{m}$ . To analyze the AFM data we documented the steps I performed in Gwyddion 2.6 in Figure 94.

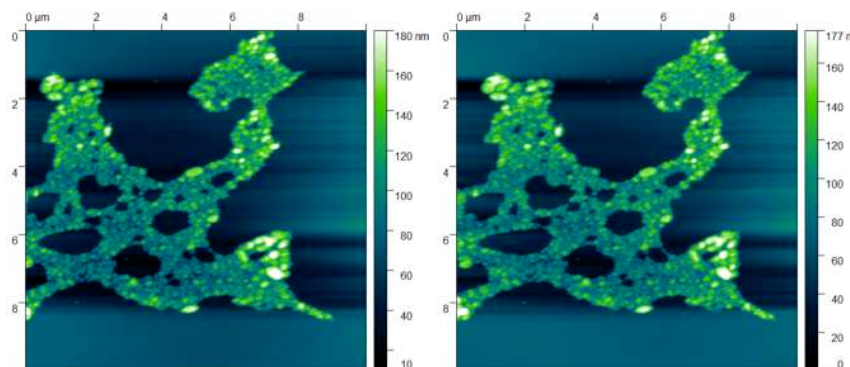


**Figure 98:** AFM pictures of measurement position 1 annotated in Figure 95. Height Backward (left) and Height Forward (right), size: 10  $\mu\text{m}$  to 10  $\mu\text{m}$

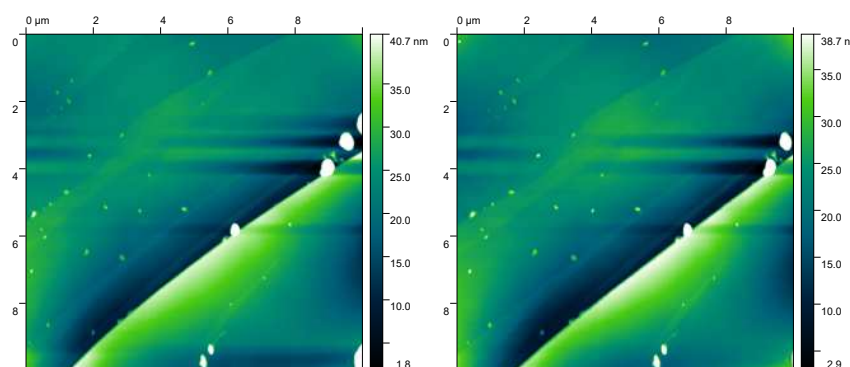


**Figure 99:** AFM pictures of measurement position 2 annotated in Figure 95. Height Backward (left) and Height Forward (right), size: 10  $\mu\text{m}$  to 10  $\mu\text{m}$

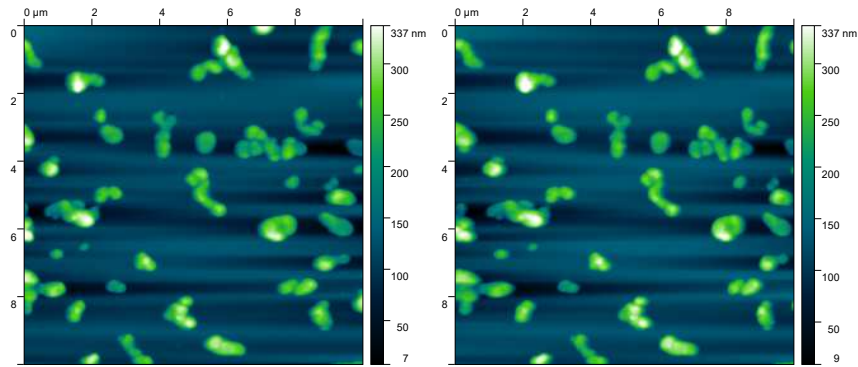


**Figure 100:** AFM pictures of measurement position 3 annotated in Figure 95. Height Backward (left) and Height Forward (right), size: 10  $\mu\text{m}$  to 10  $\mu\text{m}$

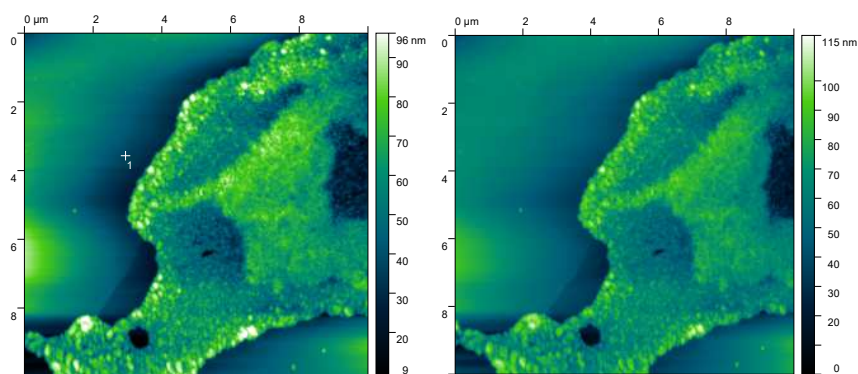


**Figure 101:** AFM pictures of measurement position 4 annotated in Figure 95. Height Backward (left) and Height Forward (right), size: 10  $\mu\text{m}$  to 10  $\mu\text{m}$

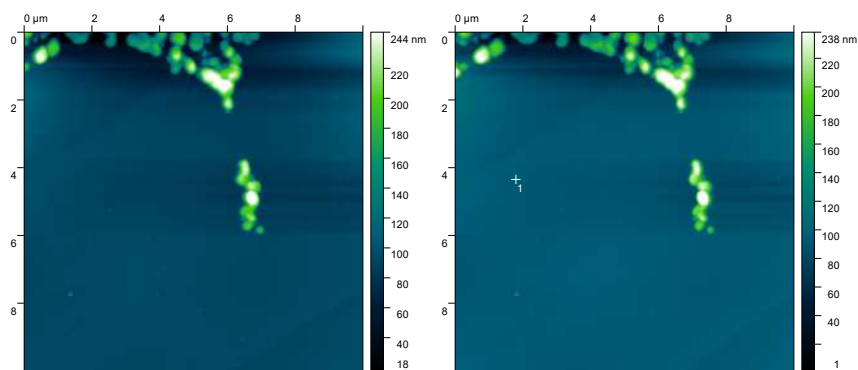


**Figure 102:** AFM pictures of measurement position 5 annotated in Figure 95. Height Backward (left) and Height Forward (right), size: 10  $\mu\text{m}$  to 10  $\mu\text{m}$

On another sample we went at the edge of a drop. We assumed that there should be a high particle density and shifted a little bit towards the center. In Figure 103 we see the HOPG surface with the steps and a gradient represented in profiles one and two. In Figure 104 we levelled the gradient as described in Figure 94. In the profiles one to four we assume that two AuNP stacked on top of each other since we see that the dots have some maximal peaks of 80 nm high and some second peaks at 40 nm. Profile one has a width of approximately 400 nm. Since our AuNPs have a diameter of 50 nm we can think of a cluster of 8 to 10 particles.



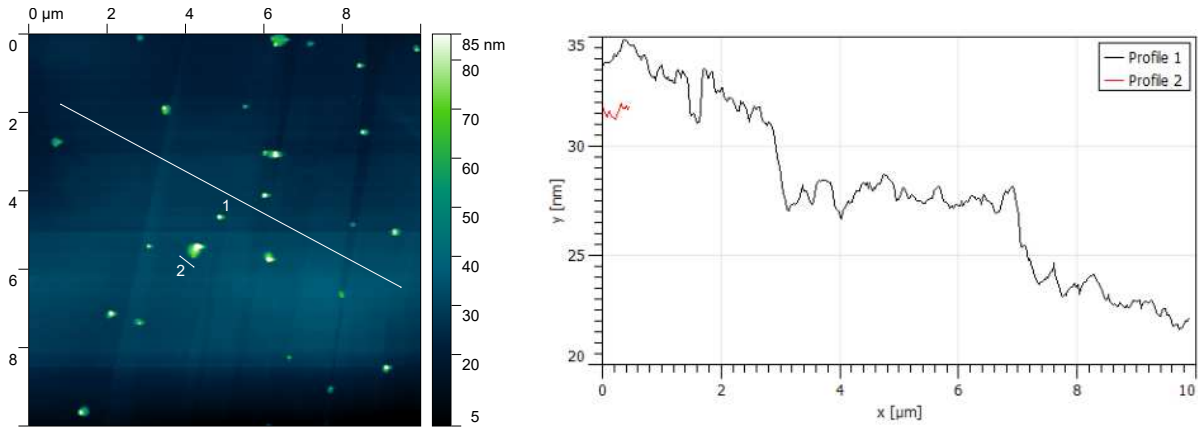


*Figure 103: In this plot we see the gradient and the steps of the HOPG ZYA sample.*

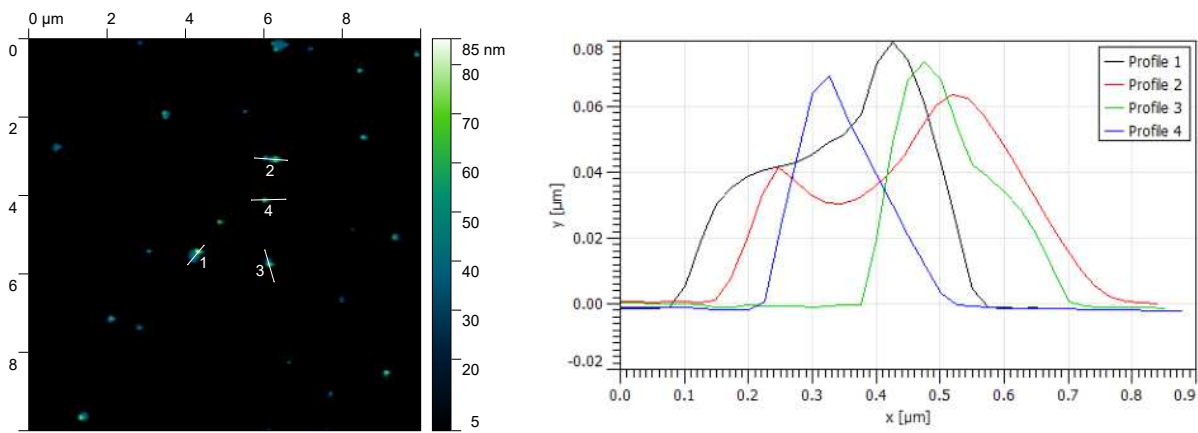


*Figure 104: In this plot we see the profile of some dots of the in the HOPG ZYA.*

We zoomed from 10  $\mu\text{m}$  to 2.5  $\mu\text{m}$  to make further interpretations. In Figure 105 we see the background with a more sensitive scale on the left and the dots on the right.

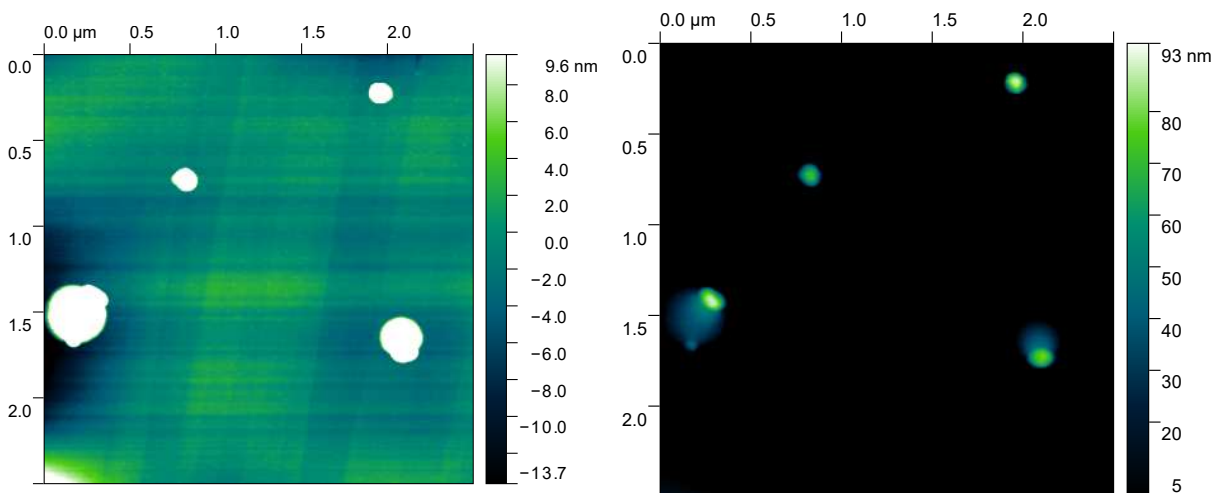


*Figure 105: Here we scaled the background and the dots differently to have a finer scale.*

In the plots of Figure 106 we analyse the width and the height of the dots. We see that the dots

have a maximum of 80 nm.

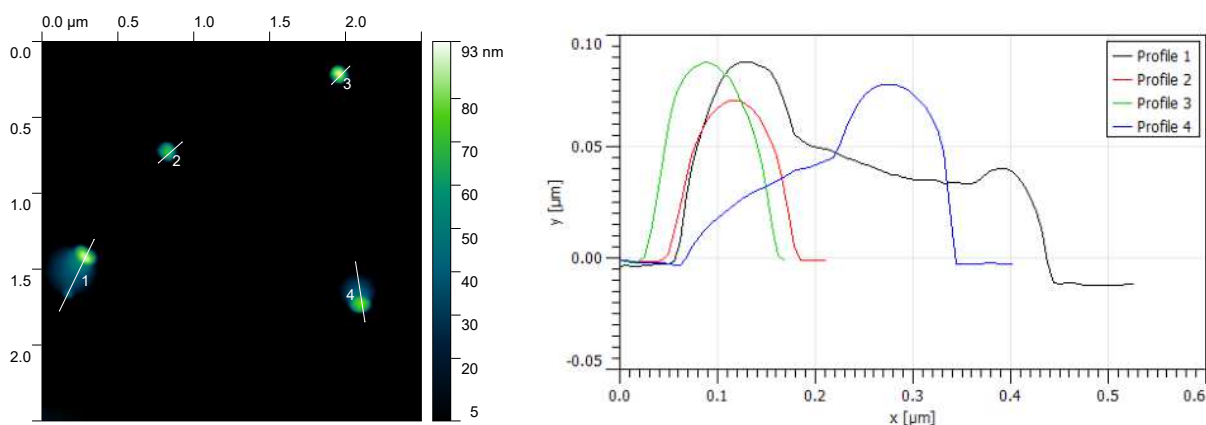


*Figure 106: In this plot we see the profile of some dots.*

### C.2.3 ZYH

We performed the same AFM measurements on a ZYA sample. The sample was not heated. In Figure 107 we focussed on the background. On the left we see that the HOPG surface is not flat as in the measurements before on the ZYA sample. There were pieces missing visible as dark marks. We see in the line profiles that we have dark parts with a height of 4 nm. In the profile two is a peak of  $\approx 1.7$  nm in the dark parts of the background. We attribute those patches to an adsorbate layer.

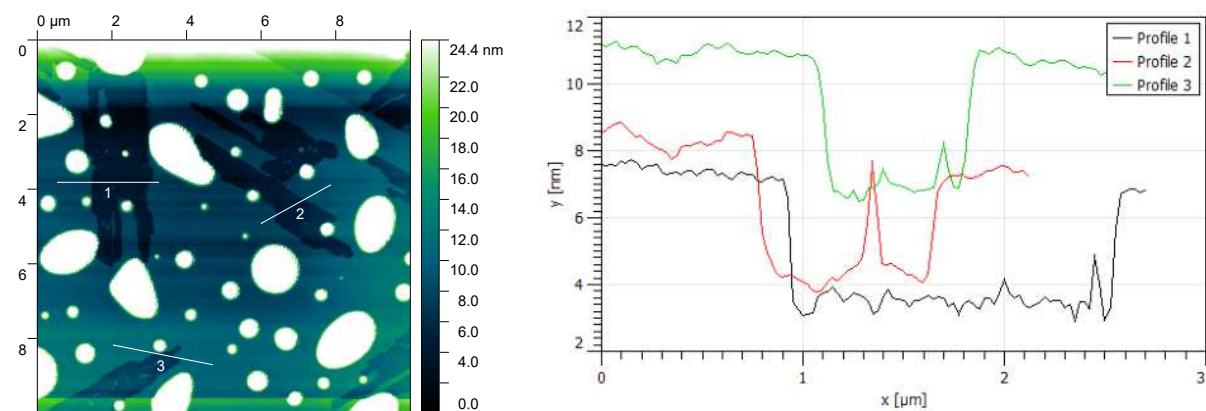


*Figure 107: Background of the measurements. We see the dark marks on the left and some lineprofiles on the right.*

We estimate the size of citrate with the table in Figure 108 on the left. For the citric acid molecule on the right we get  $(2 \cdot 1.43 + 4 \cdot 1.54) \text{ \AA} - 9 \text{ \AA} \approx 1 \text{ nm}$  which is too small for the scales we have. The chloroform in the buffer is even smaller. The apparent height of 4 nm suggests that this must be a multilayer of either the citrate or the chloroform from the buffer solution.

TABLE 8.4 Average Bond Lengths for Some Single, Double, and Triple Bonds

Bond	Bond Length (Å)	Bond	Bond Length (Å)
C—C	1.54	N—N	1.47
C=C	1.34	N=N	1.24
C≡C	1.20	N≡N	1.10
C—N	1.43	N—O	1.36
C=N	1.38	N=O	1.22
C≡N	1.16		
C—O	1.43	O—O	1.48
		O=O	1.21

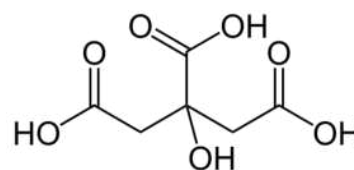


Figure 108: Data (left) and the structural formula (right) of citric acid to estimate its size.

In the picture on the left of Figure 109 we see wavy lines pointing to an instable AFM junction. This is because we had some struggles changing the measurement conditions for the AFM. They make the interpretation of the measurement more difficult but in the line profiles we can see a plateau around 50 nm.

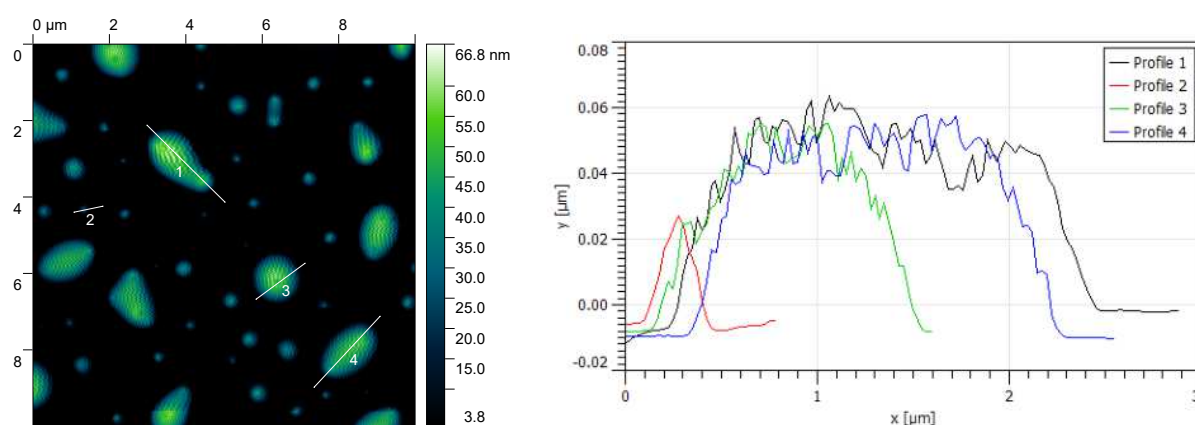
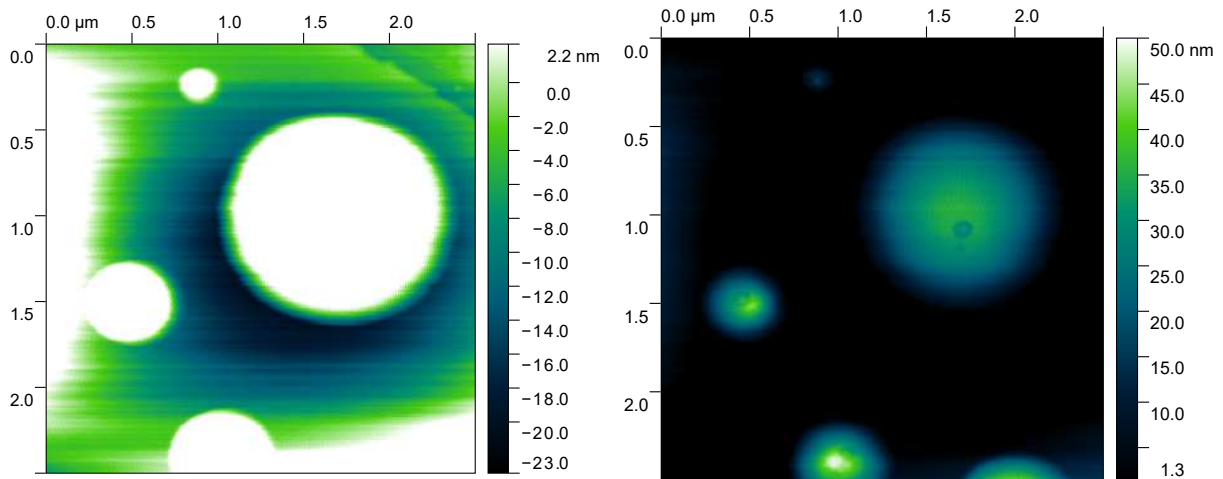
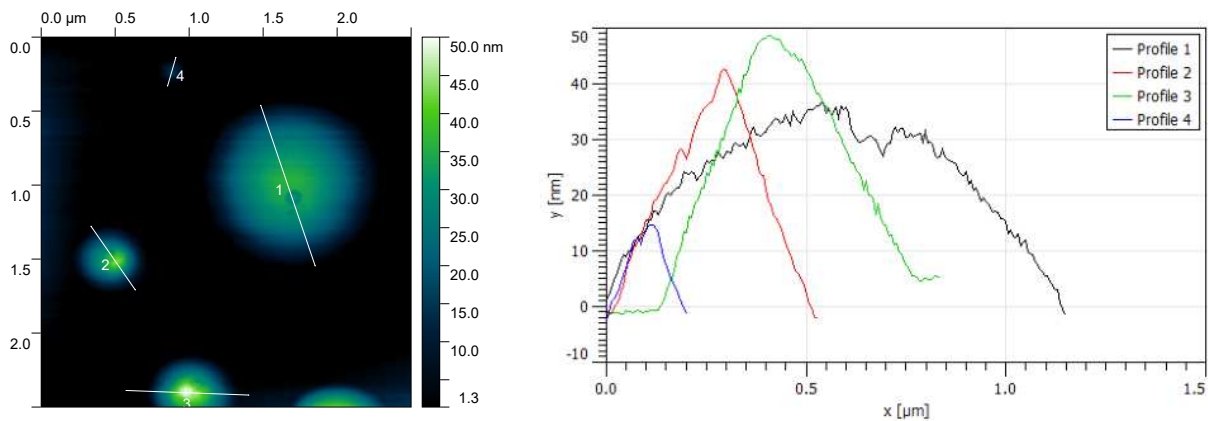


Figure 109: Measurement and line profile of dots on the ZYH sample.

We made a second scan in a smaller scan frame of 2.5 μm and took another measurement to make further interpretations. In Figure 110 we see the background with a more sensitive scale and the dots on the right. In the plots below we analyse the width and the height of the dots.



**Figure 110:** Here we scaled the background and the dots differently to have a finer scale. We see that the big dot sits in a indentation. Therefore I conclude, that the height of this dot will be below 50 nm



**Figure 111:** As expected is the height of the Dot profile 1 too low. But in general there is a lot of unexpected stuff happening on the unheated sample.

### C.3 Light sensitive camera stingray F-145

#### C.3.1 ImageJ analysis

To look at the measurements from the stingray F-145 camera we performed the following image processing steps in ImageJ.

1. Load all pictures in ImageJ
2. Press Image → Stacks → Images to Stack
3. Then Image → Stacks → Z Project and choose Average Intensity. With Ctr, Shift and C we see the contrast settings. The changes made in the contrast are noted next to the pictures with Min and Max.
4. Then take the position and with the star tool mark the tip (see Figure 112)



5. Go back to the stacked picture and press Ctr, Shift and E to mark the position, the tip was marked on the position picture.

The yellow dots in Figure 112 on the left corresponds to the tip position on the left.

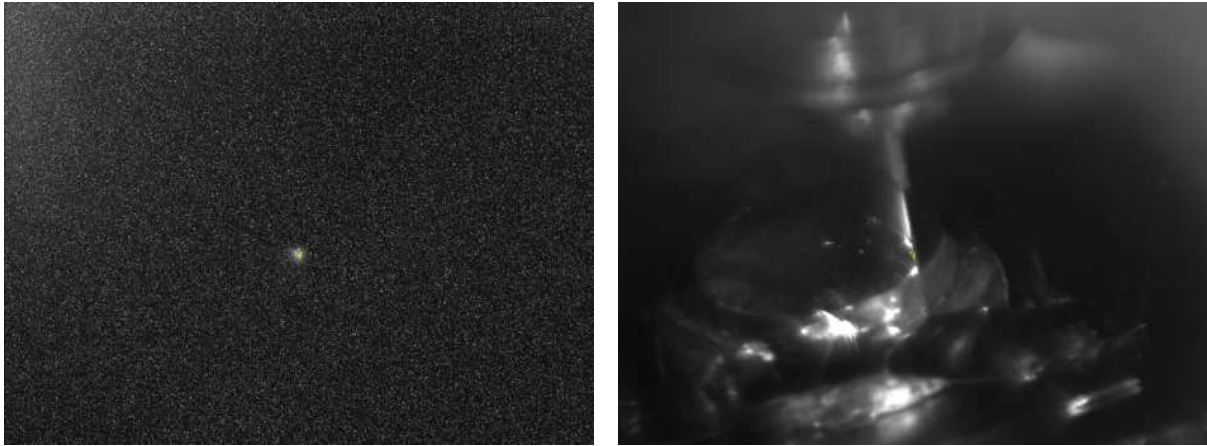


*Figure 112: Stacked measurements (left) with a marked yellow spot to show that the bright spot corresponds to the tip location (right).*



### C.3.2 Collecting the light coming from the STM junction with the Stingray camera.

*Figure 113: Series of luminescence experiments for different current and bias conditions for an functionalized tip (indentation in an Au(111) crystal) on Au(111) crystal. We were using the Stingray camera and stacked the pictures as described before. The settings are next to the pictures.*

**Settings**

-3.5 V, 50 nA

Exposure: 67 s

Gain: 5 db, ATI: 50

Min: 0, Max: 20



(1)

**Settings**

-3.5 V, 40 nA

Exposure: 67 s

Gain: 5 db, ATI: 50

Min: 0, Max: 20



(2)

**Settings**

-3.5 V, 30 nA

Exposure: 67 s

Gain: 5 db, ATI: 50

Min: 0, Max: 20



(3)

*Figure 114: Table of different setting and measurement results.*

**Settings**

+3.5 V, 40 nA

Exposure: 67 s

Gain: 5 db, ATI: 50

Min: 0, Max: 20



(1)

**Settings**

-3.5 V, 50 nA

Exposure: 67 s

Gain: 5 db, ATI: 50

Min: 0, Max: 20



(2)

*Figure 115: Table of different setting and measurement results.*

**Settings**

-0.5 V, 50 nA

Exposure: 60 s

Gain: 5 db, ATI: 50

Min: 0, Max: 20



(1)

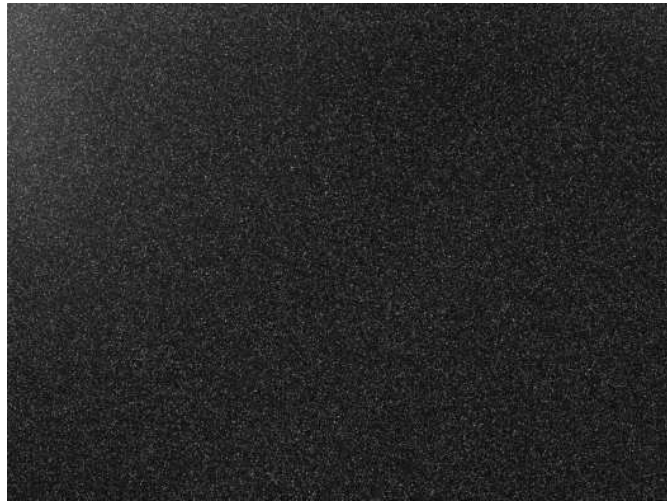
**Settings**

-1.0 V, 50 nA

Exposure: 60 s

Gain: 5 db, ATI: 50

Min: 0, Max: 20



(2)

**Settings**

-1.5 V, 50 nA

Exposure: 60 s

Gain: 5 db, ATI: 50

Min: 0, Max: 20



(3)

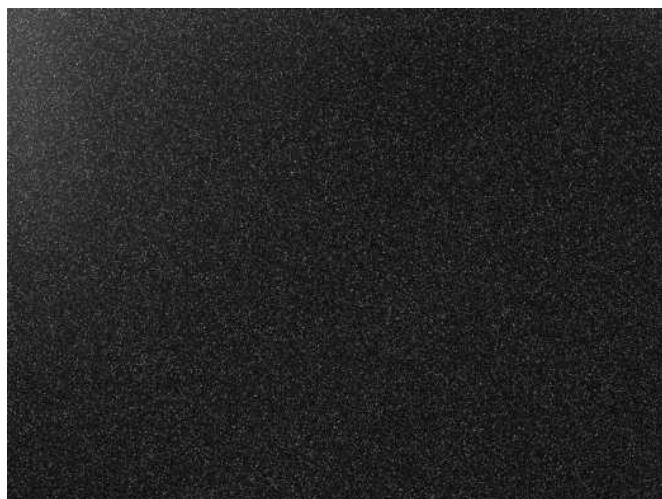
**Settings**

-2.0 V, 50 nA

Exposure: 60 s

Gain: 5 db, ATI: 50

Min: 0, Max: 20



(4)

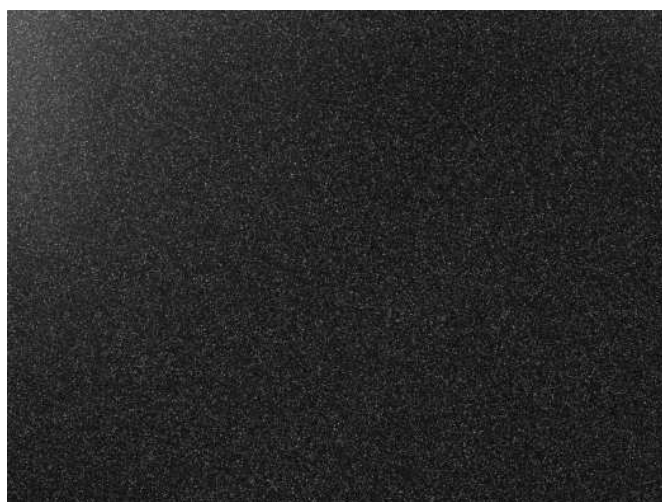
**Settings**

-2.5 V, 50 nA

Exposure: 67 s

Gain: 5 db, ATI: 50

Min: 0, Max: 20



(5)

**Settings**

-3.5 V, 50 nA

Exposure: 67 s

Gain: 5 db, ATI: 50

Min: 0, Max: 20



(6)

**Settings**

-4.0 V, 50 nA

Exposure: 67 s

Gain: 5 db, ATI: 50

Min: 0, Max: 20



(7)

**Settings**

-4.5 V, 50 nA

Exposure: 67 s

Gain: 5 db, ATI: 50

Min: 0, Max: 20



(8)

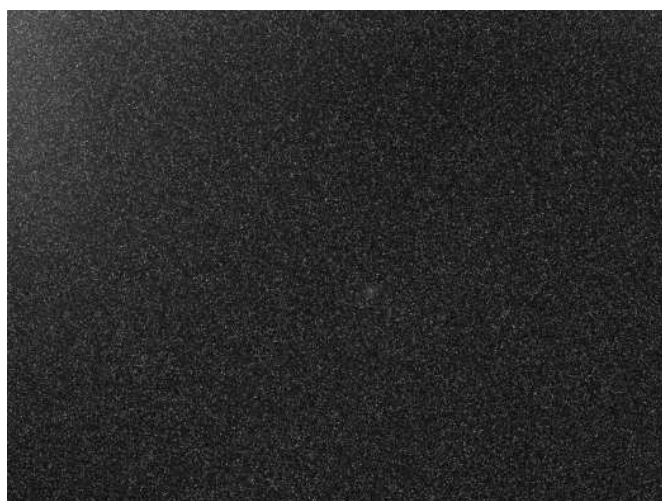
**Settings**

-5.0 V, 50 nA

Exposure: 60 s

Gain: 5 db, ATI: 50

Min: 0, Max: 20



(9)



**Settings**

-5.5 V, 50 nA

Exposure: 60 s

Gain: 5 db, ATI: 50

Min: 0, Max: 20



(10)

**Settings**

-6.0 V, 50 nA

Exposure: 60 s

Gain: 5 db, ATI: 50

Min: 0, Max: 20



(11)

**Settings**

-6.5 V, 50 nA

Exposure: 60 s

Gain: 5 db, ATI: 50

Min: 0, Max: 20



(12)

## C.4 Single Photon detector

### C.4.1 Measurements with LFM1F-1 fibre pointing directly in the junction

With the setup where the fibre was pointing directly at the junction we were not able to detect more photons than the darkcount. We averaged over the countrates taken over 5 minutes in step of 10s and compared it as countrates per second for 1 nA and 50 nA in the following Figure 113.

*Figure 113: Comparison for the countrates detected for 1 nA and 50 nA.*

